

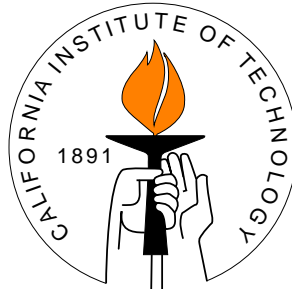


**Search for  
Heavy Neutral Resonances  
in the Dielectron Channel  
with the CMS Detector  
at the LHC**

THESIS BY

VLADLEN TIMCIUC

IN PARTIAL FULFILLMENT OF THE REQUIREMENTS  
FOR THE DEGREE OF  
DOCTOR OF PHILOSOPHY



CALIFORNIA INSTITUTE OF TECHNOLOGY  
PASADENA, CALIFORNIA

2013

(DEFENDED MAY 10, 2013)

© 2013

VLADLEN TIMCIUC

ALL RIGHTS RESERVED

# Acknowledgments

I would like to thank Professor Harvey Newman, my research adviser, for guidance and support throughout my years as a graduate student at Caltech, and for being an inspiring example of the achievements one can reach through hard and persistent work.

Thank you to Adolf Bornheim, Vladimir Litvin, Patrick Jarry, and Francesca Cavallari for helping me to get started with research at CERN, first during test beams and later with the Laser Monitoring System.

I would also like to thank Lubomir Djambazov, Werner Lustermann, Bozhidar Panev, Bojan Loncar, and the entire ECAL supermodule assembly team for enabling my contribution to the construction of CMS ECAL supermodules and helping me during my first days at CERN.

I would like to thank Roberta Arcidiacono, Christopher Palmer, and Jeremy Werner for our work together in hunting for the first signs of  $J/\psi$  and  $\Upsilon$  resonances at CMS.

I would like to thank the entire  $Z'$  analysis team (HEEP), and in particular Barbara Clerbaux, Claire Shephard-Themistocleous, Sam Harper, and Laurent Thomas for our productive work on the  $Z'$  analysis, both at CERN and in Brussels. It was a great experience working with all of you.

I would like to thank all my colleagues at Caltech CMS group for our work together, in particular: Jan Veverka, Yousi Ma, Yong Yang, Christopher Rogan, and Marat Gataullin.

A special “thank you” to Bertrand Echenard for going through my thesis drafts and providing tremendous support and advice throughout this process.

Finally and most importantly I would like to say “thank you” to my parents Alla and Iacov Timeciuc, for the help, support, and inspiration they provided me

throughout this time.

---

# Abstract

A search for dielectron decays of heavy neutral resonances has been performed using proton-proton collision data collected at  $\sqrt{s} = 7$  TeV by the Compact Muon Solenoid (CMS) experiment at the Large Hadron Collider (LHC) in 2011. The data sample corresponds to an integrated luminosity of  $5 \text{ fb}^{-1}$ . The dielectron mass distribution is consistent with Standard Model (SM) predictions. An upper limit on the ratio of the cross section times branching fraction of new bosons, normalized to the cross section times branching fraction of the Z boson, is set at the 95 % confidence level. This result is translated into limits on the mass of new neutral particles at the level of 2120 GeV for the  $Z'$  in the Sequential Standard Model, 1810 GeV for the superstring-inspired  $Z'_{\psi}$  resonance, and 1940 (1640) GeV for Kaluza-Klein gravitons with the coupling parameter  $k/M_{Pl}$  of 0.10 (0.05).



# Contents

<b>Acknowledgments</b>	<b>iii</b>
<b>Abstract</b>	<b>v</b>
<b>List of Tables</b>	<b>xii</b>
<b>List of Figures</b>	<b>xiii</b>
<b>1 Introduction</b>	<b>1</b>
<b>2 Theory overview</b>	<b>3</b>
2.1 The Standard Model . . . . .	3
2.2 Open questions and beyond the Standard Model . . . . .	6
2.3 Extensions to the Standard Model and Heavy Neutral Resonances . . . . .	7
2.4 Production at the LHC and previous searches . . . . .	10
<b>3 Experimental Apparatus</b>	<b>13</b>
3.1 The Large Hadron Collider . . . . .	13
3.2 CMS . . . . .	19
3.2.1 Introduction . . . . .	19
3.2.2 Tracker . . . . .	21
3.2.3 Electromagnetic calorimeter . . . . .	23
3.2.4 Hadron calorimeter . . . . .	28
3.2.5 The muon system . . . . .	32
<b>4 ECAL Laser Monitoring System</b>	<b>39</b>
4.1 ECAL crystal transparency change . . . . .	40

4.2	ECAL Laser Monitoring System . . . . .	41
4.3	Laser Monitoring System data-flow . . . . .	44
4.3.1	General data-flow strategy . . . . .	45
4.3.2	Online database . . . . .	46
4.3.3	Offline database . . . . .	47
4.4	Data flow specifications and optimization . . . . .	49
4.5	Summary . . . . .	50
<b>5</b>	<b>Electron Reconstruction</b>	<b>53</b>
5.1	Electron reconstruction overview . . . . .	53
5.2	ECAL clustering . . . . .	54
5.2.1	Clustering in the barrel region . . . . .	55
5.2.2	Clustering in the endcap . . . . .	56
5.2.3	Recovery of energy deposited in preshower . . . . .	58
5.2.4	Energy reconstruction . . . . .	58
5.3	Track reconstruction . . . . .	60
5.4	Preselection and energy determination . . . . .	62
5.4.1	Preselection . . . . .	62
5.4.2	Momentum determination . . . . .	63
<b>6</b>	<b>Electron Identification</b>	<b>67</b>
6.1	Selection variables . . . . .	68
6.1.1	Isolation variables . . . . .	69
6.1.2	Identification variables . . . . .	72
6.1.3	Photon conversion rejection . . . . .	75
6.2	Electron selection at intermediate energies . . . . .	77
6.3	Electron selection at high energies . . . . .	77
<b>7</b>	<b>ECAL Energy Scale and Dielectron Mass Resolution</b>	<b>81</b>
7.1	ECAL energy scale . . . . .	81
7.2	Energy scale and dielectron mass resolution with $Z \rightarrow e^+e^-$ . . . . .	85

7.2.1	Energy scale and dielectron mass resolution estimation method	86
7.2.2	Method performance in data . . . . .	87
7.2.3	Fixed Crystal Ball cut off parameter consideration . . . . .	94
7.3	Summary . . . . .	95
<b>8</b>	<b>Search for Heavy Neutral Resonances</b>	<b>97</b>
8.1	Event selection . . . . .	98
8.1.1	Data sets and trigger . . . . .	99
8.2	Validation of the Monte Carlo simulation with the data . . . . .	103
8.3	Selection efficiency . . . . .	107
8.3.1	Trigger efficiency . . . . .	107
8.3.2	Electron identification efficiency scale factors . . . . .	108
8.3.3	Total reconstruction and identification efficiency . . . . .	108
8.4	Dielectron mass resolution and electron energy scale . . . . .	110
8.4.1	Energy scale validation . . . . .	110
8.4.2	Resolution parametrization . . . . .	113
8.4.3	Energy scale evolution . . . . .	114
8.5	Background estimation . . . . .	117
8.5.1	Standard Model Drell-Yan . . . . .	117
8.5.2	Other prompt electrons . . . . .	120
8.5.3	Jets and misidentified electrons . . . . .	122
8.6	Results . . . . .	127
8.6.1	Dielectron mass spectrum . . . . .	127
8.6.2	Signal and background parametrization . . . . .	131
8.6.3	Statistical interpretation . . . . .	135
8.6.4	Combination with the dimuon channel . . . . .	138
<b>9</b>	<b>Conclusion</b>	<b>141</b>
9.1	Summary . . . . .	141
9.2	Current status and outlook . . . . .	141

**Bibliography****145**

---

# List of Tables

2.1	Properties of Quarks and Leptons . . . . .	4
2.2	Fundamental forces and associated gauge bosons with their properties	5
2.3	Lower mass limits for various $Z'$ models, from the LEP experiments .	11
2.4	Lower mass limits for various $Z'$ models, obtained by the D0 experiment	11
2.5	Lower mass limits for various $Z'$ models, obtained by the CDF experiment	11
3.1	Design ECAL energy resolution parameters. . . . .	29
4.1	Online database access optimization results. . . . .	50
5.1	Hybrid clustering algorithm parameters. . . . .	56
5.2	Multi $5 \times 5$ clustering algorithm parameters. . . . .	58
5.3	Definition of the seed matching windows. . . . .	61
6.1	Electron identification criteria for intermediate energy electrons at 95 % efficiency. . . . .	78
6.2	Electron identification criteria for intermediate energy electrons at 80 % efficiency. . . . .	79
6.3	Electron identification criteria at high energies. . . . .	79
7.1	Datasets used for the study of the ECAL energy scale validation method.	88
8.1	A summary of the data sets used in the analysis . . . . .	100
8.2	The triggers used in the analysis, together with their run ranges . . .	101
8.3	The electron energy scale summary for the different ECAL regions as measured at the $Z$ peak. Comparison between the data and MC. . . . .	110
8.4	The dielectron mass resolution for different ECAL regions, as measured at the $Z$ peak for the data and the MC . . . . .	113
8.5	Energy scale for the different run periods and electron topologies . . .	115
8.6	The electron preselection requirements for the “fake rate” calculation.	124

8.7	The functional form of the “fake rate” for the three pseudo-rapidity regions. . . . .	124
8.8	The number of dilepton events with an invariant mass in the control region $120 < m_{ee} < 200$ GeV and in the search region $m_{ee} > 200$ GeV	130

# List of Figures

3.1	A schematic diagram of the LHC accelerator complex . . . . .	14
3.2	LHC dipole magnet. . . . .	15
3.3	A schematic layout of LHC interaction points. . . . .	16
3.4	LHC peak luminosity 2011. . . . .	17
3.5	LHC delivered luminosity 2011. . . . .	18
3.6	The Compact Muon Solenoid detector . . . . .	19
3.7	A slice of the CMS detector . . . . .	20
3.8	The CMS tracker system . . . . .	21
3.9	The CMS tracker material budget units of radiation length as a function of the pseudorapidity $\eta$ . . . . .	22
3.10	The CMS tracker transverse momentum resolution. . . . .	23
3.11	The CMS Electromagnetic calorimeter. . . . .	24
3.12	The CMS Electromagnetic calorimeter, barrel region. . . . .	25
3.13	The ECAL $PbW_04$ crystals with photodetectors attached. . . . .	26
3.14	The CMS Electromagnetic calorimeter, endcap Dee . . . . .	27
3.15	CMS ECAL energy resolution as a function of energy. . . . .	30
3.16	The CMS Hadronic calorimeter layout. . . . .	31
3.17	A schematic view of the HCAL tower mapping in the $r - z$ plane for the barrel and endcap regions. . . . .	32
3.18	A schematic layout of the CMS Muon system. . . . .	33
3.19	A schematic layout of the CMS Muon DT system. . . . .	34
3.20	The layout of a DT chamber inside a muon barrel station. . . . .	35
3.21	The layout of a CSC chamber. . . . .	36
3.22	The muon momentum resolution as a function of momentum for different $\eta$ regions. . . . .	37

4.1	Results from the test-beam irradiation studies. . . . .	41
4.2	Laser monitoring light source, Nd:YLF pump laser and a tunable Ti:Sapphire laser by Quantronix. . . . .	42
4.3	Laser monitoring light source, diode pumped YVO <sub>4</sub> laser by Photonics.	43
4.4	Laser Monitoring system schematics. . . . .	44
4.5	Laser Monitoring System Data-flow. . . . .	45
4.6	OMDS Laser Monitoring System database schematic representation. .	47
4.7	ORCON/ORCOFF Laser Monitoring System objects representation.	49
4.8	Reconstructed $\pi^0$ mass peak position with and without transparency corrections applied as a function of time . . . . .	51
4.9	$E/p$ ratio for electrons from $W \rightarrow e\nu$ decays with and without transparency corrections applied as a function of time . . . . .	51
4.10	Di-electron invariant mass distribution for the $Z \rightarrow ee$ candidate events with and without ECAL inter-calibration applied, and with and without ECAL crystal transparency corrections applied . . . . .	52
5.1	An illustration of the Hybrid clustering algorithm . . . . .	56
5.2	An illustration of the Multi5×5 clustering algorithm . . . . .	58
5.3	Electron energy resolution . . . . .	65
6.1	Electron isolation variables in the barrel region . . . . .	69
6.2	Electron isolation variables in the endcap region . . . . .	71
6.3	Electron identification variables in the barrel region . . . . .	73
6.4	Electron identification variables in the endcap region . . . . .	74
6.5	Photon conversion pattern in the inner tracker layers . . . . .	76
7.1	Energy scale reference region definition . . . . .	83
7.2	CB⊗BW fit for the data and the MC for all categories and for both non-showering electrons, 2010 data set . . . . .	90
7.3	CB⊗BW fit for the data and the MC for both showering electrons and for both non-showering electrons, in the ECAL barrel region . . . . .	91
7.4	CB⊗BW fit for the data and the MC for both showering electrons and for both non-showering electrons, in the ECAL endcap region . . . . .	92

7.5	CB $\otimes$ BW fit for the data and the MC for both Low r9 and for both High r9 electrons, in the ECAL barrel region . . . . .	92
7.6	CB $\otimes$ BW fit for the data and the MC for both Low r9 and for both High r9 electrons, in the ECAL endcap region . . . . .	93
7.7	Crystal Ball cut off systematics in the barrel region . . . . .	94
7.8	Crystal Ball cut off systematics in the endcap region . . . . .	95
8.1	Feynman diagram for the Drell–Yan process . . . . .	98
8.2	CMS event display for a $Z'_{SSM}$ candidate in simulation . . . . .	99
8.3	Electron isolation variables in barrel region data vs. simulation validation. . . . .	103
8.4	Electron isolation variables in endcap region data vs. simulation validation. . . . .	104
8.5	Electron identification variables in barrel region data vs. simulation validation. . . . .	105
8.6	Electron identification variables in endcap region data vs. simulation validation. . . . .	106
8.7	The MC estimated total reconstruction and selection efficiency vs $E_T^{truth}$ . . . . .	109
8.8	The invariant mass spectrum of the data and MC overlaid with the CB $\otimes$ BW fit results, for EB-EB and EE-EE categories . . . . .	111
8.9	The invariant mass spectrum of the data and MC overlaid with the CB $\otimes$ BW fit results, for EB-EE and EB-EB & EB-EE categories . . . . .	112
8.10	The dielectron mass resolution as a function of the mass, derived from the DY MC and corrected by the $\sigma_{CB}(extra)$ measured at the Z peak, for the EB-EB and EB-EE categories . . . . .	114
8.11	The dielectron mass resolution as a function of the mass, derived from the DY MC and corrected by the $\sigma_{CB}(extra)$ measured at the Z peak, for the EB-EB & EB-EE category . . . . .	115
8.12	The invariant mass spectrum of the data and MC overlaid with the CB $\otimes$ BW fit results for EB-EB & EB-EE category. Run2011A and Run2011B separately . . . . .	116

8.13 Comparison between PYTHIA and POWHEG for the Drell-Yan process.	119
8.14 The observed opposite-sign $e^\pm\mu^\mp$ dilepton invariant mass spectrum .	121
8.15 The “fake rate” probability for a jet to be identified as an electron. .	123
8.16 Comparison of the two jet background estimation methods. . . . .	126
8.17 The invariant mass spectrum of $ee$ events . . . . .	128
8.18 The cumulative distribution of the dielectron invariant mass spectrum	129
8.19 Results of Breit-Wigner function fit to the true MC invariant mass distribution for several mass points for the $Z'_{SSM}$ and $Z'_\Psi$ models . . .	132
8.20 The background parametrization . . . . .	133
8.21 The relative difference between the data and the fitted parametrization of the simulated background . . . . .	133
8.22 Kinematic acceptance times electron reconstruction and identification efficiency parametrization for the signal. . . . .	134
8.23 Upper limits as a function of the resonance mass $M$ on the production ratio $R_\sigma$ of cross section times branching fraction into electron pairs for $Z'_{SSM}$ , $Z'_\Psi$ , and $G_{KK}$ production to the same quantity for Z bosons	137
8.24 Upper limits as a function of the resonance mass $M$ on the production ratio $R_\sigma$ of cross section times branching fraction into lepton pairs for $Z'_{SSM}$ , $Z'_\Psi$ , $Z'_{St}$ , and $G_{KK}$ production to the same quantity for Z bosons. The combination of the electron and muon channel results .	139
9.1 The invariant mass spectra of $ee$ and $\mu^+\mu^-$ events, for 2012 data set .	143
9.2 Upper limits as a function of resonance mass on the production ratio $R_\sigma$ of cross section times branching fraction into lepton pairs for $Z'_{SSM}$ and $Z'_\psi$ boson production to the same quantity for Z bosons. The combination of the electron and muon channel results for 2012 data set	144

# Chapter 1

## Introduction

*“Eigentlich weiß man nur, wenn man wenig weiß;  
mit dem Wissen wächst der Zweifel.”*

Maximen und Reflexionen,  
Johann Wolfgang von Goethe

*“We know accurately only when we know little;  
with knowledge doubt increases.”*

Maxims and Reflections,  
Johann Wolfgang von Goethe

The Standard Model (SM) is one of the most successful theories in modern physics. It describes a wide spectrum of phenomena, and has been validated experimentally to a high level of precision. Despite its success many fundamental questions remain unanswered. To address these questions, certain extensions of the SM propose the existence of a new heavy neutral boson, generically referred to as  $Z'$ .

We search for  $Z'$  at the Large Hadron Collider (LHC), where heavy neutral resonances can be identified through their dileptonic decays. In this thesis I present a search for a heavy neutral resonance in the dielectron ( $e^+e^-$ ) final state.

This analysis is based on the data set collected by the Compact Muon Solenoid (CMS) detector during the 2011 proton-proton data-taking period, corresponding to an integrated luminosity of  $5.0 \text{ fb}^{-1}$ .

This thesis is structured as follows. The theoretical framework is presented in Chapter 2, followed by description of the LHC and CMS in Chapter 3. The CMS Laser Monitoring System is described in more detail in Chapter 4. The details of

electron reconstruction and identification are presented in Chapters 5 and 6. The method for validation of the electron energy scale and the estimation of the dielectron mass resolution is introduced in Chapter 7. The search for new heavy resonances is detailed in Chapter 8. The results are summarized in Chapter 9, together with a brief overview of the current results.

# Chapter 2

## Theory overview

### 2.1 The Standard Model

The Standard Model (SM) of particle physics [1, 2, 3, 4, 5, 6, 7] is a highly successful theory that describes the fundamental interactions between elementary particles. It has been validated by many experiments to a high degree of precision [8, 9].

The Standard Model successfully describes three of the four fundamental forces: the electromagnetic, the weak, and the strong force. The gravitational force is not part of the SM, and is described by the General Theory of Relativity (no theory of Quantum Gravity exists to this date).

The fundamental particles of the Standard Model are the quarks, leptons, and the force-carrying particles - gauge bosons. The quarks and leptons represent building blocks of matter, which interact via the exchange of gauge bosons to form protons, neutrons and atoms. Both the leptons and quarks are spin 1/2 fermions, while gauge bosons have spin 1. Each particle is accompanied by an anti-particle with the same mass and spin, but opposite internal quantum numbers.

The leptons are the electron  $e$ , muon  $\mu$ , tau  $\tau$ , and their corresponding neutrinos  $\nu_e$ ,  $\nu_\mu$  and  $\nu_\tau$ , and are grouped into three generations  $(e, \nu_e)$ ,  $(\mu, \nu_\mu)$  and  $(\tau, \nu_\tau)$ . Electrons, muons, and taus are charged and interact via the electromagnetic and weak forces, while the neutrinos interact only via the weak force. Although the SM assumes that neutrinos are massless, the observation of neutrino oscillation shows that they are massive, however the mass values are experimentally constrained to be very small [8]. The properties of the leptons are summarized in Table 2.1 [8].

Generation	Leptons			Quarks		
	Flavors	Charge (e)	Mass (MeV)	Flavors	Charge (e)	Mass (MeV)
1	$e$	-1	0.511	$u$	+2/3	1 - 4
	$\nu_e$	0	$< 2 \times 10^{-6}$	$d$	-1/3	3 - 7
2	$\mu$	-1	105.6	$c$	+2/3	$1.15 - 1.35 \times 10^3$
	$\nu_\mu$	0	$< 0.19$	$s$	-1/3	70 - 130
3	$\tau$	-1	1777	$t$	+2/3	$\sim 173 \times 10^3$
	$\nu_\tau$	0	$< 18.2$	$b$	-1/3	$4.1 - 4.4 \times 10^3$

Table 2.1: Properties of Quarks and Leptons [8].

The quarks are represented by up ( $u$ ), down ( $d$ ), charm ( $c$ ), strange ( $s$ ), top ( $t$ ) and bottom ( $b$ ) quarks. In addition to the electric charge, quarks possess an internal degree of freedom called color, which can be red, blue and green. The quarks are also grouped into three generations ( $u, d$ ), ( $c, s$ ), and ( $t, b$ ). The quarks interact via the strong, electromagnetic, and weak forces. The properties of the quarks are summarized in Table 2.1 [8].

In the Standard Model the gauge bosons are the mediators of the forces between particles. Charged particles interact via the electromagnetic force mediated by the photon ( $\gamma$ ), these interactions are described by Quantum Electrodynamics (QED) [3]. The weak force is mediated by the  $W^\pm$  and  $Z$  bosons and can act on all leptons and quarks. In the Standard Model, the electromagnetic and weak interactions are unified in the Electroweak Theory, first introduced by Glashow, Weinberg and Salam [1]. The strong force that enables interaction of colored particles is mediated by gluons ( $g$ ) and is described by Quantum Chromodynamics (QCD) [2]. The properties of the gauge bosons are summarized in Table 2.2 [8].

More specifically, the Standard Model is a locally gauge invariant quantum field theory. The gauge symmetry group of the Standard Model is:

$$SU(3)_C \times SU(2)_L \times U(1)_Y, \quad (2.1)$$

where  $SU(3)_C$  is the symmetry group of the strong interactions, “C” - stands for color, and  $SU(2)_L \times U(1)_Y$  is the symmetry group of the unified electromagnetic and

Force	Gauge boson	Charge	Spin	Mass (GeV)	Range
Electromagnetic	Photon ( $\gamma$ )	0	1	0	$\infty$
Weak	$W^\pm$	$\pm 1$	1	80.4	$10^{-18} \text{ m}$
	Z	0	1	91.2	
Strong	Gluon ( $g$ )	0	1	0	$10^{-15} \text{ m}$
Gravity	Graviton ( $G$ )	0	2	0	$\infty$

Table 2.2: Fundamental forces and associated gauge bosons with their properties [8].

weak interactions, “L” indicates that  $SU(2)$  acts only on the left-handed part of the spinors, and “Y” is the weak hypercharge.

Quantum Chromodynamics (QCD) is based on the  $SU(3)_C$  symmetry group corresponding to colors that quarks possess. The requirement of local gauge invariance under this symmetry requires the existence of 8 massless gauge bosons, the gluons. Gluons also have color, thus gluons can also interact with themselves. Gluon-gluon interactions contribute to two phenomenologically important properties of the strong force. The first is *asymptotic freedom* - as the energy scale of the interaction increases the coupling constant becomes small. This property allows for perturbative calculation to be made for strong interactions at high energies [6]. The second is quark *confinement* - the force between quarks increases with distance, leaving quarks either bound together, or through quark-antiquark pair creation resulting in two separate hadrons [31]. That explains the absence of free quarks and the formation of mesons and hadrons which are color-neutral combinations of quarks.

The unified theory of the electromagnetic and weak interactions is based on the gauge group  $SU(2)_L \times U(1)_Y$  and is described by the Glashow-Salam-Weinberg (GSW) theory [1]. The gauge fields associated to this group are 3 gauge bosons  $W_\mu^i$  ( $i=1,2,3$ ) for  $SU(2)_L$  group and a  $B_\mu$  for the  $U(1)_Y$  group, all of which are massless.

The Higgs mechanism [7] (spontaneous symmetry breaking) is used to break the symmetry of the  $SU(2)_L \times U(1)_Y$  group at low energies and to give mass to the vector bosons. Spontaneous symmetry breaking [7] breaks some of the components of the

symmetry, and leaves the  $U(1)_{em}$  symmetry group unbroken, which corresponds to electromagnetic interactions and is described by Quantum Electrodynamics (QED). The  $U(1)_{em}$  symmetry group requires the existence of a massless gauge boson, the photon ( $\gamma$ ), as the carrier of electromagnetic force. After symmetry breaking the gauge bosons mix to form the weak and electromagnetic fields as follows:

$$W_\mu^\pm = \frac{1}{\sqrt{2}}(W_\mu^1 \mp W_\mu^2), \quad (2.2)$$

$$Z_\mu = \cos \theta_W W_\mu^3 - \sin \theta_W B_\mu, \quad (2.3)$$

$$A_\mu = \sin \theta_W W_\mu^3 + \cos \theta_W B_\mu, \quad (2.4)$$

where  $\theta_W$  is the weak mixing angle defined as  $\theta_W = \tan^{-1} g'/g$ , where  $g$  and  $g'$  are the coupling constants of  $SU(2)_L$  and  $U(1)_Y$ , respectively;  $A_\mu$  is the electromagnetic photon field ( $\gamma$ );  $W_\mu^\pm$  and  $Z_\mu$  are the charged and neutral weak fields, correspondingly. This mechanism requires the introduction of a complex scalar Higgs doublet. The potential introduced by this field breaks part of the EW gauge symmetry, after which only one neutral Higgs scalar  $H$  remains. As a result, the  $W^\pm$  and  $Z$  acquire masses and the photon remains massless.

In 2012, a Higgs-like particle has been observed independently by both the CMS and ATLAS collaborations at LHC, CERN [10, 11]. It still remains to be seen if this particle is exactly the one described by the Standard Model, but if it is indeed the SM Higgs boson, then this discovery would complete the Standard Model.

## 2.2 Open questions and beyond the Standard Model

The Standard Model is a highly successful quantum field theory. It has been confirmed to a high precision [9, 8] (with a few 2 - 3 sigma deviations) by the experimental measurements. However it still doesn't answer some fundamental questions and has a few considerations that don't come very naturally. I list a few of them below:

- The Standard Model doesn't include gravity

- The Hierarchy problem and fine-tuning
- The number of fermion generations is arbitrary
- There are no candidates for dark matter
- There is a lack of explanation for dark energy

To overcome some of these difficulties many theories beyond the Standard Model have been proposed, such as Grand Unified Theories (GUTs), Supersymmetric Theories (SUSY), String Theory, Left-Right symmetric models, etc. In some of these theories, the existence of one or more extra neutral gauge bosons is predicted. We will briefly review some of them in the next section.

## 2.3 Extensions to the Standard Model and Heavy Neutral Resonances

The electric and magnetic forces, that at first appeared as independent phenomena, are parts of a unified electromagnetic force. At low energies, the electromagnetic and weak interactions appear as unrelated phenomena, but above the electroweak scale the two forces are unified to form the electroweak interaction. It is natural to assume that at some energy scale the Electroweak Theory is unified with the theory of strong interactions, Quantum Chromodynamics (QCD), to form the Grand Unified Theory (GUT), that would describe all three forces within a corresponding  $G_{GUT}$  group. At the electroweak scale such a GUT theory is then reduced to a low-energy effective theory described by the Standard Model, and  $G_{GUT}$  is decomposed to the Standard Model gauge group (Eq. 2.1).

The simplest extension that includes the SM gauge group is  $SU(5)$ , however it was shown to be inconsistent with the proton lifetime and the electroweak mixing angle measurements [12]. The next simplest GUT groups are  $SO(10)$  and  $E_6$ .  $E_6$  group can arise as an effective GUT group in superstrings theories [13]. The  $E_6$  can be decomposed as follows:  $E_6 \rightarrow SO(10) \times U(1)_\psi$  and  $SO(10) \rightarrow SU(5) \times U(1)_\chi$ .

Each of the extra  $U(1)$  groups would have a neutral gauge boson associated to it, analogous to the SM  $Z$ . In the case described above, it would lead to the so-called  $Z_\psi$  and  $Z_\chi$  neutral gauge bosons [14]. As an additional simplification, an effective model can be considered were the two  $U(1)$  symmetries are further broken down as  $U(1)_\psi \times U(1)_\chi \rightarrow U(1)_\theta$  where corresponding  $Z_\theta$  is a linear combination of  $Z_\psi$  and  $Z_\chi$ . For such an effective model, the corresponding mass eigenstate is given by

$$Z'(\theta) = Z_\psi \cos \theta - Z_\chi \sin \theta \quad (2.5)$$

where the parameter  $\theta$  is a priori unknown [16, 15]. As  $\theta$  is varied, several  $Z'$  models result. The value  $\theta = 0$  corresponds to  $Z' = Z_\psi$ , while  $\theta = -90^\circ$  corresponds to  $Z' = Z_\chi$ . Other  $Z'$  models are sometimes considered, such as  $Z' = Z_\eta$  and  $Z' = Z_I$  which correspond to  $\sin \theta = \sqrt{3/8}$  and  $\sin \theta = \sqrt{5/8}$ , respectively, where  $Z_\eta$  corresponds to the case when  $E_6$  is decomposed directly to  $SU(3)_C \times SU(2)_L \times U(1)_Y \times U(1)_\eta$ , and  $Z_I$  arises in the  $SU(6) \times SU(2)_I$  decomposition of  $E_6$  [15].

Depending on the GUT group and its decomposition, one or more extra  $U(1)$  groups with the associated neutral gauge bosons are introduced. The bosons are generally referred to as  $Z'$ 's. The discovery of such a particle could point to the possibility of grand unification.

A neutral gauge boson  $Z'$  can also be produced in the so-called Stueckelberg Extension [19, 20] of the Standard Model, that extends the gauge symmetry of the SM with an additional  $U(1)_X$  gauge symmetry. The extension is based on the Stueckelberg mechanism [21, 22], in which abelian vector bosons can acquire mass without breaking the gauge invariance of the Lagrangian. In this extension, there is a non-trivial mixing of the  $U(1)_Y$  hypercharge gauge field  $B_\mu$  with the  $U(1)_X$  Stueckelberg gauge field  $C_\mu$  and an axionic scalar  $\sigma$ . Assuming that scalar field  $\sigma$  couples only to the abelian gauge bosons  $B_\mu$  and  $C_\mu$ , this theory contains a massless photon, massive  $Z$  and one extra massive gauge boson  $Z'$  (denoted as  $Z'_{StSM}$ ) after the standard spontaneous electron-weak symmetry breaking. The strength of the coupling to the SM is governed by the dimensionless parameter  $\epsilon$ . When  $\epsilon \rightarrow 0$ , the Stueckelberg sector

decouples from the Standard Model. An upper bound of 0.061 on  $\epsilon$  has been derived from the correction to the  $Z$  mass [23].

From an experimental point of view, it is not essential which model is chosen as the  $Z'$  candidate, they all lead to the same analysis structure. In particular it is common practice to use the Sequential Standard Model ( $Z'_{SSM}$ ) as a benchmark model among many experiments. In this model  $Z'$  has the same couplings to quarks and leptons as the SM  $Z$ , but an arbitrarily high mass [17, 18].

In addition to  $Z'$  models, heavy neutral resonances can be produced in the context of the Randall-Sundrum theory of extra dimensions [24]. In this theory the existence of one additional extra-dimension is proposed, which generates the hierarchy between the Planck and electroweak scales. The Standard Model is confined to a 4-dimensional subspace (or “brane”) of the 5-dimensional space. The extra-dimension is parametrized by the angular coordinate  $\phi$  ( $0 \leq |\phi| \leq \pi$ ), the compactification radius  $r_c$ , and the curvature of the extra dimension  $k$ . The Planck brane is located at  $\phi = 0$ , while SM is located at  $\phi = \pi$ . TeV scales are generated from fundamental scales of order  $M_{Pl}$  via a geometrical exponential warp factor:  $\Lambda_\pi = \bar{M}_{Pl} e^{-kr_c\pi}$ , where  $\Lambda_\pi \sim \text{TeV}$ ,  $\bar{M}_{Pl} = M_{Pl}/\sqrt{8\pi}$  is the reduced Planck scale. The hierarchy is reproduced if  $kr_c \simeq 12$  and no additional hierarchies are generated.

The compactification of the extra dimension gives rise to a Kaluza-Klein (KK) tower of graviton states. The masses of the KK graviton states are given by  $m_n = kx_n e^{-kr_c\pi}$ , where  $x_n$  is the  $n^{th}$  root of the first-order Bessel function. The decay width and coupling to SM particles depend on the mass of the first KK graviton excitation  $m_G = m_1$  and the constant  $k/\bar{M}_{Pl}$ . The value of  $k$  is expected to be such that  $0.01 \leq k/\bar{M}_{Pl} \leq 0.1$  [25]. These excitations would result in spin-2 resonances which can be produced at the TeV scale, and identified through their dilepton decay mode, among other decay modes. We will consider two benchmark values  $k/\bar{M}_{Pl} = 0.1$  and  $k/\bar{M}_{Pl} = 0.05$ .

## 2.4 Production at the LHC and previous searches

At the LHC  $Z'$  resonances can be produced at tree level in quark-antiquark annihilation, and decay to a pair of fermions or W bosons. The cross section, as well as the decay branching fractions, depends on the particular model and the mass of the  $Z'$ . Among the decay channels, the dilepton final state provides a clean signature with a relatively low background contribution. In this thesis I consider only the dielectron final state.

The main background to the dielectron final state comes from the Drell-Yan process, forming an “irreducible” background to the search for  $Z'$ . This background is described by an exponentially falling distribution in the invariant mass spectrum, and a  $Z'$  signal can be easily identified as a peak on the smooth background distribution. Other sources of background include  $t\bar{t}$ ,  $tW$  and  $WW$  production, where dielectron final states can be produced in semileptonic decays of the W bosons, and QCD multijet and W + Jets production, where a jet can be misidentified as an electron. Relative contributions of these backgrounds after the analysis selection is applied, and methods of determining these background contributions, are discussed in more detail in Chapter 8.

Previous searches for  $Z'$ s have been performed both directly by the Tevatron experiments [26], and indirectly by the LEP experiments [33, 27]. The LEP collaborations have set mass limits on a set of  $Z'$  models, which are summarized in Table 2.3 [28]. At the Tevatron the direct searches for  $Z'$ s in the dielectron channel have set mass limits on some of the benchmark models, as summarized in Tables 2.4, 2.5 [30, 29]. In addition RS gravitons with masses below 848 GeV are excluded at 95 % C.L. for  $k/\bar{M}_{Pl} = 0.1$ , in the dielectron final state by the CDF experiment, based on  $2.5 \text{ fb}^{-1}$  of  $p\bar{p}$  data at  $\sqrt{s} = 1.96 \text{ TeV}$  [30].

Z' model	$Z'_\chi$	$Z'_\psi$	$Z'_\eta$	$Z'_{SSM}$
Mass (GeV)	673	481	434	1787

Table 2.3: The 95% confidence level lower limits on the  $Z'$  mass for various  $Z'$  models, from the LEP experiments [28].

Z' model	$Z'_{StSM}(\epsilon = 0.04)$	$Z'_{StSM}(\epsilon = 0.04)$	$Z'_\psi$	$Z'_\chi$	$Z'_\eta$	$Z'_{SSM}$
Mass (GeV)	417	443	891	903	923	1023

Table 2.4: Observed 95% confidence level lower limits on the  $Z'$  mass for various  $Z'$  models, in the dielectron final state, obtained by the D0 experiment based on  $5.4 \text{ fb}^{-1}$  of  $p\bar{p}$  data at  $\sqrt{s} = 1.96 \text{ TeV}$  [29].

Z' model	$Z'_\psi$	$Z'_\chi$	$Z'_\eta$	$Z'_{SSM}$
Mass (GeV)	851	862	877	963

Table 2.5: Observed 95% confidence level lower limits on the  $Z'$  mass for various  $Z'$  models, in the dielectron final state, obtained by the CDF experiment based on  $2.5 \text{ fb}^{-1}$  of  $p\bar{p}$  data at  $\sqrt{s} = 1.96 \text{ TeV}$  [30].



# Chapter 3

## Experimental Apparatus

### 3.1 The Large Hadron Collider

The Large Hadron Collider (LHC) [32] is the highest energy superconducting hadron accelerator and collider, located in the 26.7 km ring tunnel 45 m to 170 m below the ground, on the border of France and Switzerland, near Geneva. This tunnel was previously used by the LEP [33] collider and was adopted to host LHC with minor modifications. The internal diameter of the tunnel is 3.7 m, which made it extremely difficult to install two completely separate proton rings. This limitation led to the adoption of a two-bore magnet design, a so called “two-in-one” superconducting magnet design [34].

To achieve the design energy of 7 TeV per proton beam, the proton bunches undergo a series of acceleration steps before being injected into the main LHC ring, as illustrated in Figure 3.1 [35, 36]. First protons are accelerated in the linear accelerator (LINAC) and injected into the Booster where they can reach a kinetic energy of 1.4 GeV. Then the protons are injected in the Proton Synchrotron (PS) where the beams are arranged into bunches with 25 ns or 50 ns spacing, and accelerated to 25 GeV. After that proton bunches are injected into Super Proton Syncrotron (SPS) where they achieve energies of 450 GeV. And finally the proton bunches are injected into the LHC where both orbits are fed from the SPS. First the desired number of bunches per orbit is injected in the LHC ring, then through a series of accelerating RF cavities the beams are brought to desired operating energies.

The design field of the superconducting dipole magnets is 8.33 T, corresponding

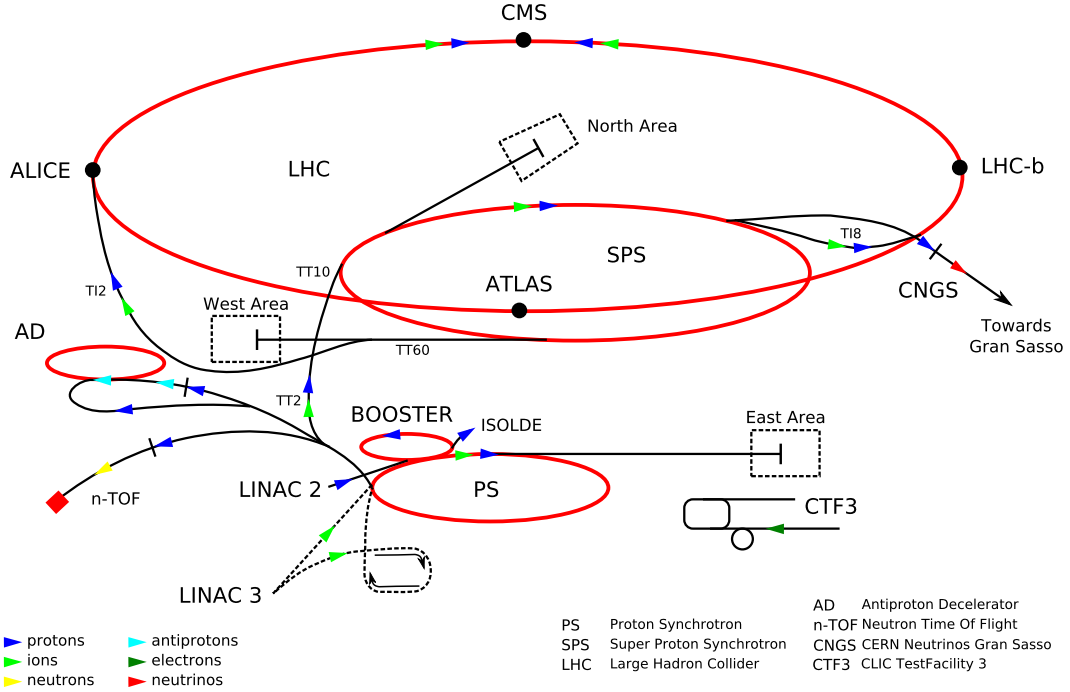


Figure 3.1: A schematic diagram of the LHC accelerator complex. Protons are first accelerated in the linear accelerator (LINAC), and transferred to the Booster where they are accelerated to a kinetic energy of 1.4 GeV. Then, they are injected into the Proton Synchrotron (PS), arranged into bunches, and are accelerated to 25 GeV. Protons then are transferred to the Super Proton Synchrotron (SPS), where they are accelerated to 450 GeV. Finally they are injected into the LHC, where they are accelerated to the operating energy [35, 36].

to a stored proton beam energy of 7 TeV. This energy level will eventually be reached once sufficient experience with LHC operation at intermediate energies is attained, in particular when the quench protection system can guarantee safe operation at these energies. The LHC suffered a major accident in September 2008, following the start up of its operation [37]. Several magnets were destroyed after a sequence of magnets quenched. The damage caused by the accident has been successfully repaired, and updated quench protection and temperature stability systems have been introduced.

To establish safe LHC operations it was initially operated at the injection energy in the center of mass of 900 GeV, and then energy was subsequently raised to 2.4 TeV

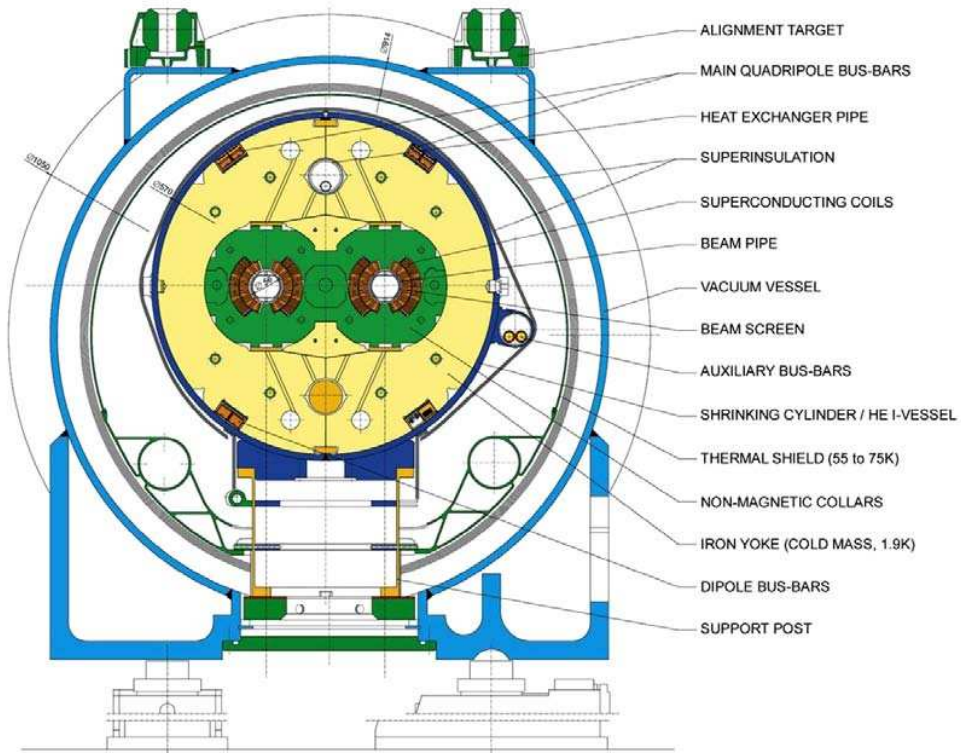


Figure 3.2: A schematic diagram of the LHC dipole magnet and cryostat structure.

by the end of 2009. After the initial commissioning the following year, the LHC has operated at 7 TeV in 2010 and 2011. In 2012 LHC was operated at 8 TeV, which was agreed upon after additional quench protection system improvements.

The LHC is composed of 1232 main dipole magnets, which are complemented with roughly 7000 other magnets dedicated to beam focusing and trajectory correction. One of the main features of the LHC is the two-bore “two-in-one” design of the superconducting dipole magnets, as shown in Figure 3.2. Both beam pipes are enclosed in a common cryogenic system and enclosed in the same mechanical structure. The magnetic field produced by the superconducting coils is in opposite directions in the two beam pipes, as needed for transporting protons in opposite directions. The magnets use NbTi superconductors operated at 1.9 K. The 1.9 K operating temperature is provided by the use of super-fluid helium. Temperature stability is crucial for safe LHC operation and is closely monitored.

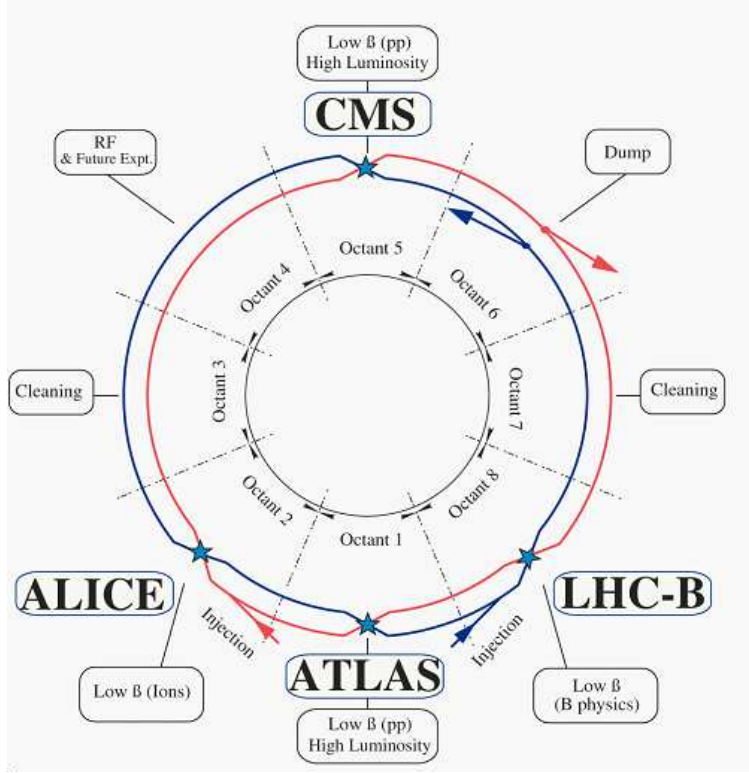


Figure 3.3: A schematic layout of LHC interaction points.

The LHC hosts four major experiments, two general purpose ones ATLAS [38] and CMS [39], and two specialized experiments ALICE [40] and LHCb [41]. The ALICE and LHCb experiments took advantage of already available caverns from the LEP experiments, while ATLAS and CMS, located at opposite sides of the LHC ring as illustrated in the Figure 3.3, are located in caverns built specifically for them.

The LHC luminosity can be expressed in terms of the beam parameters as follows [32]:

$$L = \frac{N_b^2 n_b f_{rev} \gamma_r}{4\pi \epsilon_n \beta^*} F \quad (3.1)$$

where  $N_b$  is the number of particles per bunch,  $n_b$  the number of bunches per beam,  $f_{rev}$  the revolution frequency,  $\gamma_r$  the relativistic gamma factor,  $\epsilon_n$  the normalized transverse beam emittance,  $\beta^*$  the beta function at the collision point, and  $F$  the geometric luminosity reduction fraction due to the crossing angle at the interaction point (IP).

The nominal luminosity of the LHC machine is  $10^{34} \text{ cm}^{-2}\text{s}^{-1}$ , foreseen to be reached with 2808 bunches per proton beam and  $10^{11}$  protons per bunch. During the 2010 and 2011 running periods, when the LHC was operated at 7 TeV center of mass energy, the highest instantaneous luminosity was at about  $3.5 \times 10^{33} \text{ cm}^{-2}\text{s}^{-1}$ . It was achieved with 1380 bunches per beam at 50 ns spacing, with  $1.4 \times 10^{11}$  protons per bunch.

High proton bunch density and strong focusing at the interaction points leads to production of multiple interactions per bunch crossing. This effect is referred to as “pile-up.” During the 2011 running period an average pile-up of 9 interactions per crossing was observed [103].

The evolution of the luminosity delivered to the CMS during 2011 data-taking period is presented in Figure 3.4. The corresponding integrated luminosity is shown in Figure 3.5. A total of  $6.1 \text{ fb}^{-1}$  was delivered to CMS and  $5.6 \text{ fb}^{-1}$  was recorded.

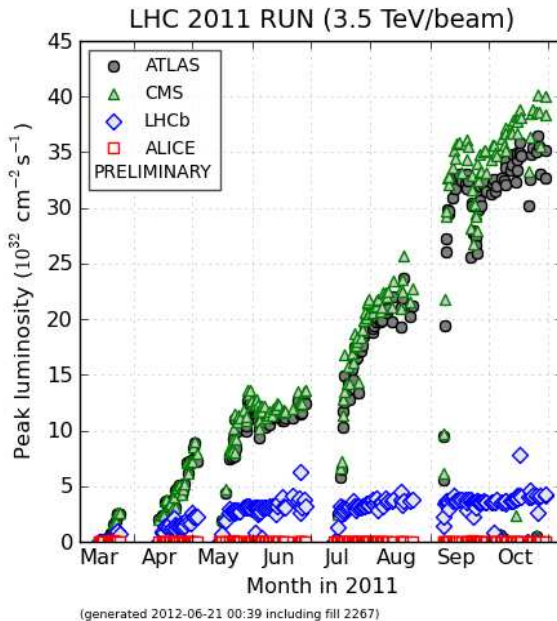


Figure 3.4: Peak luminosity delivered by the LHC machine to the LHC experiment during the 2011 run [42].

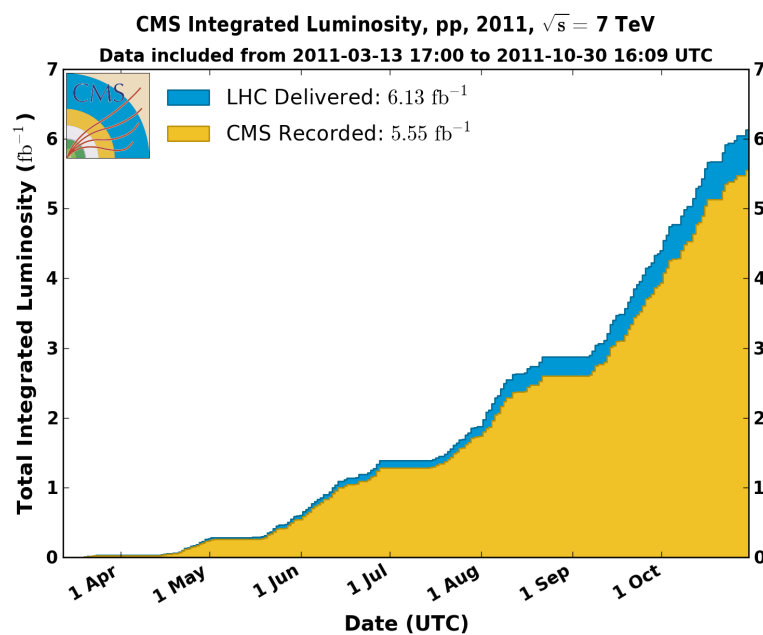


Figure 3.5: Integrated luminosity delivered by the LHC machine and recorded by the CMS experiment [43].

## 3.2 CMS

### 3.2.1 Introduction

The Compact Muon Solenoid (CMS) [39] is a general purpose experiment, designed to perform searches for physics beyond the Standard Model as well as the precise measurement of Standard Model processes. In particular the design was optimized to discover the Higgs Boson, the missing element in the Standard Model (SM). The first observation of a Higgs-like particle was established in Summer 2012 [11].

The central feature of the CMS apparatus is the 3.8 Tesla superconducting solenoidal magnet, as can be see in the Figure 3.6. Inside the magnet, tracking and calorimetry systems are located, and on the outside a set of muon detectors are present. The iron yokes surrounding the solenoid in layers provide the magnetic flux return. A muon will therefore follow an “S” shaped trajectory when traveling through the CMS detector, as illustrated in Figure 3.7.

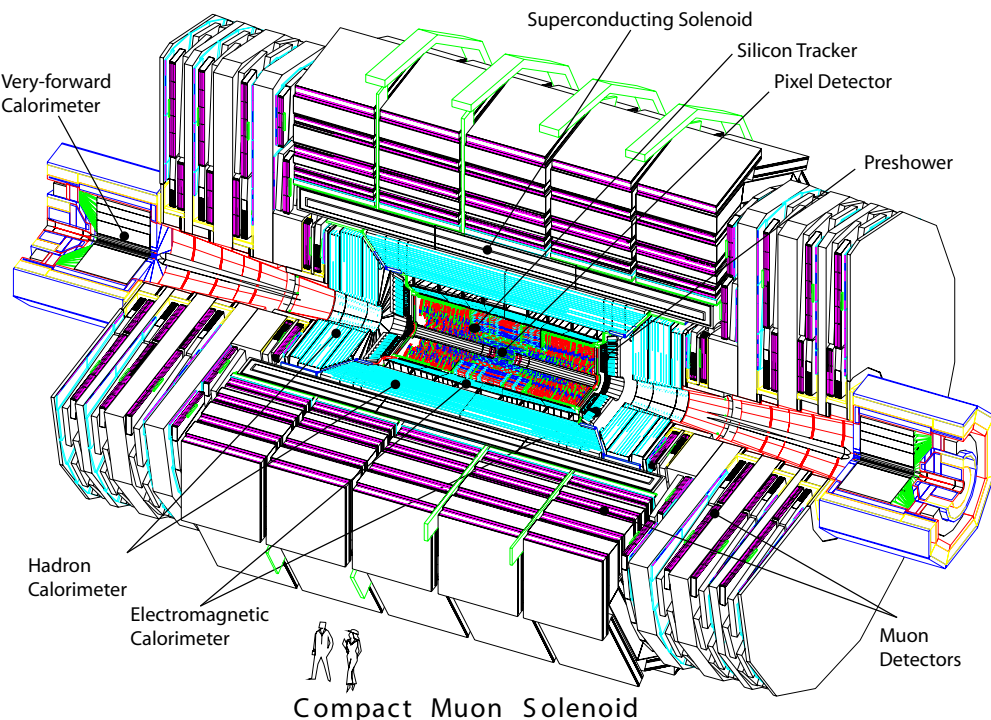


Figure 3.6: The Compact Muon Solenoid detector [44].

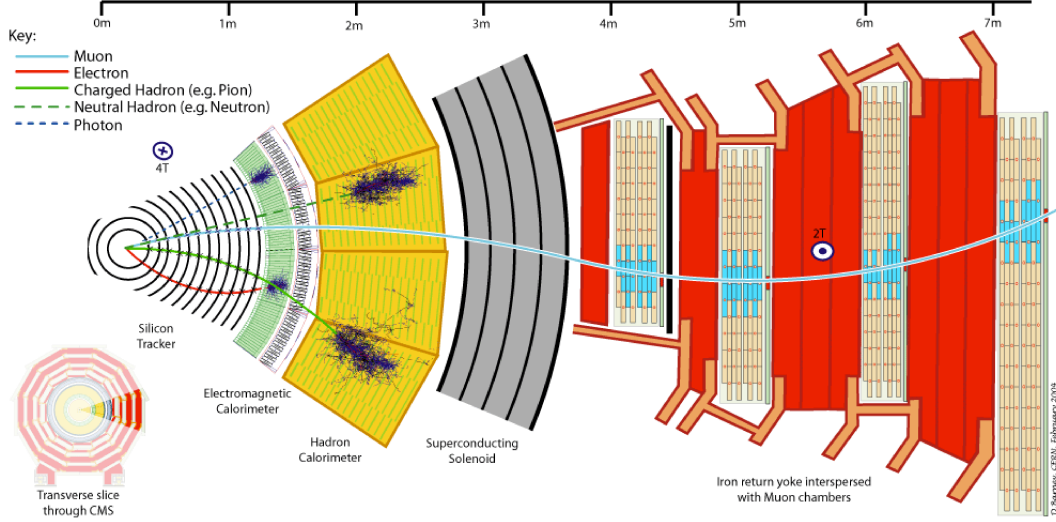


Figure 3.7: A slice of the CMS detector [45].

CMS has adopted a right handed coordinate system, with the  $x$ -axis pointing to the center of the LHC ring, the  $y$ -axis pointing upwards and the  $z$ -axis along the direction of the beam in the anticlockwise direction. The polar angle  $\phi$  is measured from the  $x$ -axis in the  $x - y$ . The polar angle  $\theta$  is measured from the  $z$ -axis. Pseudorapidity<sup>1</sup> is defined as:

$$\eta = -\ln(\tan \frac{\theta}{2}). \quad (3.2)$$

The momentum and energy measured transverse to the beam direction are denoted  $p_T$  and  $E_T$ , respectively. The imbalance of energy measured in the transverse plane is denoted by  $E_T^{miss}$ .

The CMS experiment is located at one of the interaction points (IP 5) of the LHC accelerator (Figure 3.3) in a specially built cavern which hosts the experiment itself as well as the service facilities. The overall dimensions of the CMS detector are a length of 21.6 m, a diameter of 14.6 m and a total weight of 12500 tons.

In the following sections I discuss each of the sub-detector systems in more detail.

---

<sup>1</sup>Pseudorapidity can also be written as  $\eta = -\ln(\frac{|p|+p_z}{|p|-p_z})$ , which corresponds to the rapidity, defined as  $y = -\ln(\frac{E+p_z}{E-p_z})$ , in the limit of high energies, where the masses of the particles can be neglected.

### 3.2.2 Tracker

The innermost detector of the CMS is the tracker system [46, 47]. The tracker system consists of a pixel detector, located in the direct vicinity of the interaction point, and a strip tracker detector, which surrounds the pixel detector, as illustrated in Figure 3.8. The tracker system is used to measure the momentum of the outgoing charged particles, and to identify the position of the vertex where the interaction took place. The pixel detector together with the strip tracker provides coverage up to  $|\eta| < 2.5$ .

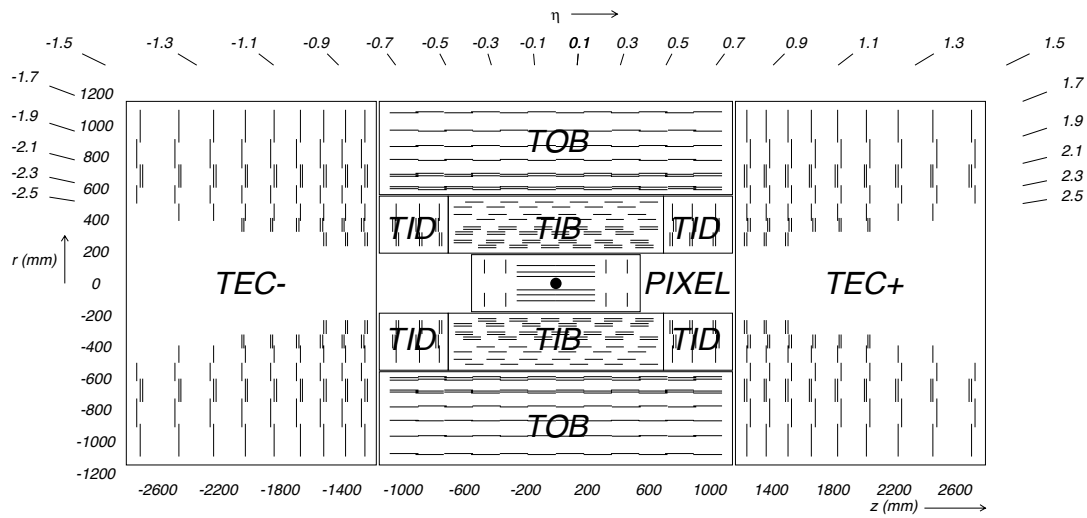


Figure 3.8: The CMS tracker system [44].

The pixel detector consists of 3 barrel layers parallel to the beam direction located between the mean radii of 4.4 cm and 10.2 cm. The barrel pixel layers are complemented by two endcap disks on each side at  $|z| = 34.5$  cm and 46.5 cm. The individual silicon pixel size is  $100 \times 150 \mu\text{m}^2$  in  $r\phi \times z$  coordinates. The pixel detector comprises 66 million pixels and has the total area of  $\sim 1 \text{ m}^2$ . The pixel detector provides high precision of interaction vertex position determination ( $\sim 10 \mu\text{m}$  in all three dimensions). Such high precision allows for an effective implementation of b jet identification (b-tagging), with high efficiency and relatively low fake rates.

The strip tracker covers the region between 20 to 110 cm in  $r$  and extends up

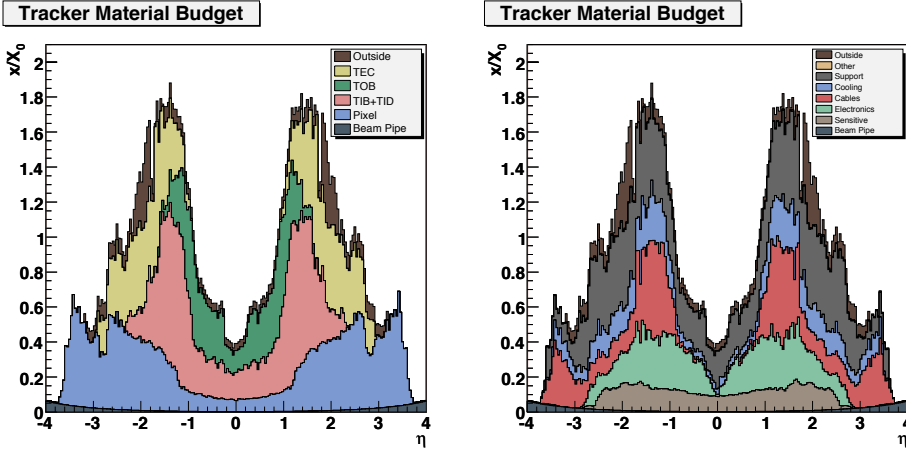


Figure 3.9: The CMS tracker material budget in units of radiation length as a function of the pseudorapidity  $\eta$  for different sub-detectors (left) and broken down into functional contributions (right) [44].

to 280 cm in the  $z$  direction. It consists of the silicon microstrip detectors arranged in several layers. The Tracker Inner Barrel (TIB) is made up of 4 layers and the Tracker Outer Barrel (TOB) comprises 6 layers (Figure 3.8). The endcaps are divided into the Tracker End Cap (TEC) comprising 9 disks that extend in the the region  $124 \text{ cm} < |z| < 282 \text{ cm}$ , and the Tracker Inner Disks consisting of two sets of 3 discs that fill the gap between TIB and TEC. The silicon sensors' thickness varies in the range of 320 to 500  $\mu\text{m}$  and the strip pitch varies from 80  $\mu\text{m}$  in the TIB to 180  $\mu\text{m}$  in TEC and TOB. Overall the strip tracker comprises 9.3 million silicon strips covering a total area of 200  $\text{m}^2$ .

The tracker silicon detectors together with the readout electronics and support structure presents a considerable amount of material to particles traveling from the interaction point. Figure 3.9 [44] shows the material budget of the CMS tracker in units of the radiation lengths ( $X_0$ ). It increases from 0.4  $X_0$  at  $\eta = 0$  to about 1.8  $X_0$  at  $\eta = 1.4$ , and decreases to about 1  $X_0$  at  $\eta = 2.5$ . This leads to a high conversion probability for photons in the tracker material.

Figure 3.10 shows the tracker transverse momentum resolution for single muons

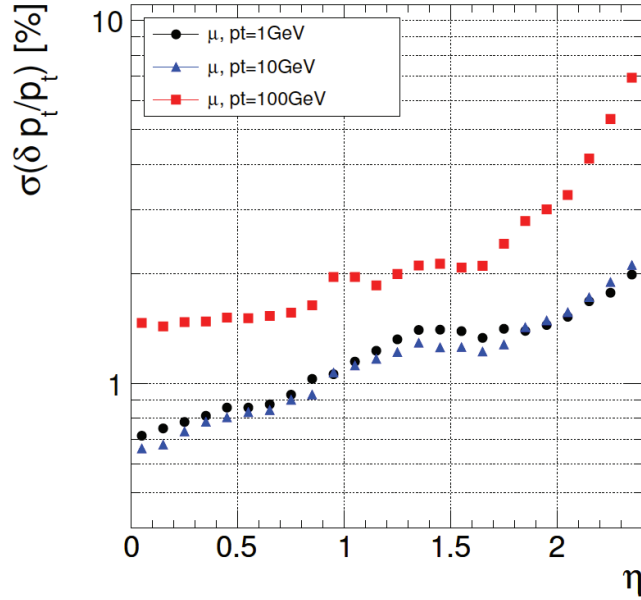


Figure 3.10: The CMS tracker transverse momentum resolution for single muons with transverse momenta 1, 10 and 100 GeV, as a function of  $\eta$  [44].

at different values of  $p_T$ , as a function of pseudorapidity. For high  $p_T$  tracks, the resolution ranges from 1.5 % at  $\eta = 0$  to 7 % at  $\eta = 2.5$ .

### 3.2.3 Electromagnetic calorimeter

The electromagnetic calorimeter of CMS (ECAL) [48] is a hermetic, high-resolution, high-granularity scintillating crystal calorimeter comprising 61200 lead tungstate ( $PbWO_4$ ) crystals mounted in the central barrel part ( $|\eta| < 1.48$ ), and 7324 crystals in each of the two endcaps ( $1.5 < |\eta| < 3.0$ ) (Figure 3.11). A preshower detector is placed in front of the endcap crystals in the region  $1.65 < |\eta| < 2.6$ . Avalanche photodiodes (APDs) are used as photo-detectors in the barrel and vacuum phototriodes (VPTs) in the endcaps.

The choice of lead tungstate ( $PbWO_4$ ) for the ECAL crystals is based on the characteristics of this material, which are suitable for the hadron collider environment, and for a total absorption ECAL that fits within the design dimensions of the CMS.

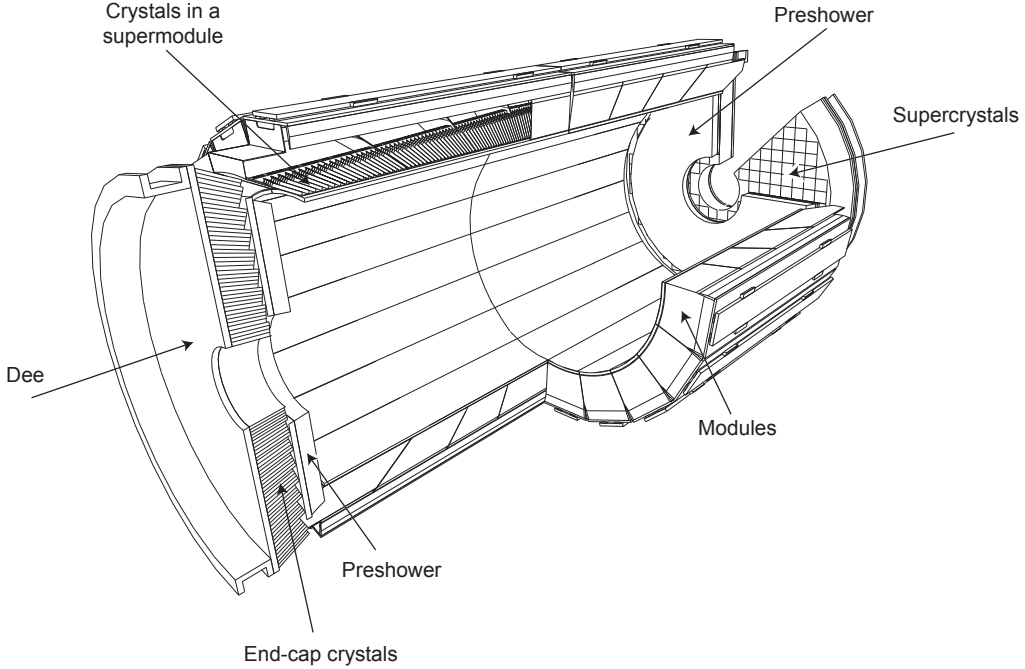


Figure 3.11: The CMS Electromagnetic calorimeter [48].

The high density ( $8.28 \text{ g/cm}^3$ ), short radiation length ( $X_0 = 0.89 \text{ cm}$ ) and small Moliere radius (2.2 cm) allow for a high granularity and a compact calorimeter design. The crystals are optically clear, fast and relatively radiation-hard [49, 50, 60]. About 80 % of light is emitted in 25 ns. The light output is relatively low: about 4.5 photo-electrons per MeV are collected in both APDs and VPTs. The crystals emit blue-green scintillation light with a broad maximum at 420-430 nm [50, 59].

The ECAL  $PbWO_4$  crystals are radiation resistant but experience dose rate dependent optical transparency loss due to the color center formation [59]. A dose rate dependent equilibrium is achieved between production of the color centers, and their thermal annealing [60]. Thus the effect is more pronounced for higher instantaneous luminosities and for the high pseudorapidity ECAL regions. In order to provide ECAL uniform response and stable energy measurement the transparency of each individual crystal in ECAL is monitored by the ECAL Laser Monitoring System [62] that was built, commissioned and installed, and is now operated by the Caltech group. The

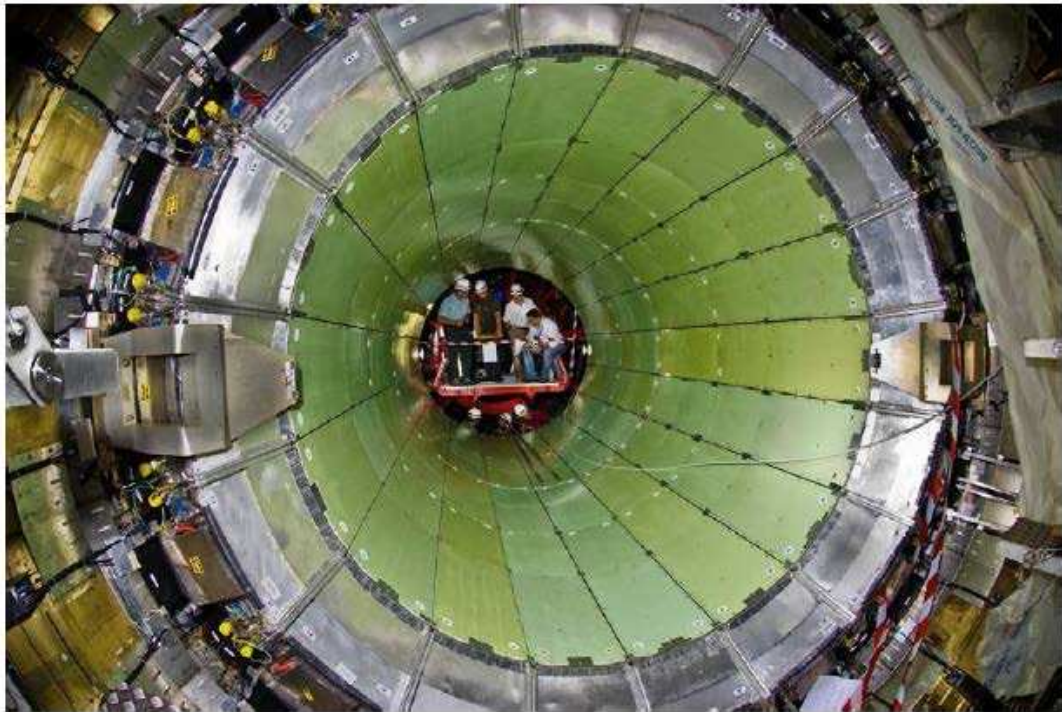


Figure 3.12: The CMS Electromagnetic calorimeter, barrel region.

change in response to laser light is translated to the change in crystal response to incident particles, and is corrected for at the event reconstruction step. The ECAL Laser Monitoring System and its performance are described in more detail in Chapter 4.

The barrel part of the ECAL (EB) has an inner radius of 129 cm and is composed of 36 identical “supermodules,” 18 in each half of the ECAL barrel as shown in Figures 3.11 and 3.12, covering the region  $|\eta| < 1.479$ . Each supermodule contains 1700 crystals arranged in quasi-projective geometry to avoid cracks aligned with particle trajectories originating at the interaction point. Crystal axes make an angle of  $3^\circ$  with respect to the direction to the nominal interaction vertex, in both the  $\phi$  and  $\eta$  directions. The crystals have a front face cross section of  $22 \times 22 \text{ mm}^2$  and  $26 \times 26 \text{ mm}^2$  at the rear face, corresponding to approximately  $0.0174 \times 0.0174$  in  $\eta - \phi$  (or  $1^\circ \times 1^\circ$ ). The length of the crystals in the barrel region is 230 mm, corresponding to  $25.8 X_0$ . Each crystal surface is initially polished to exploit total internal reflection

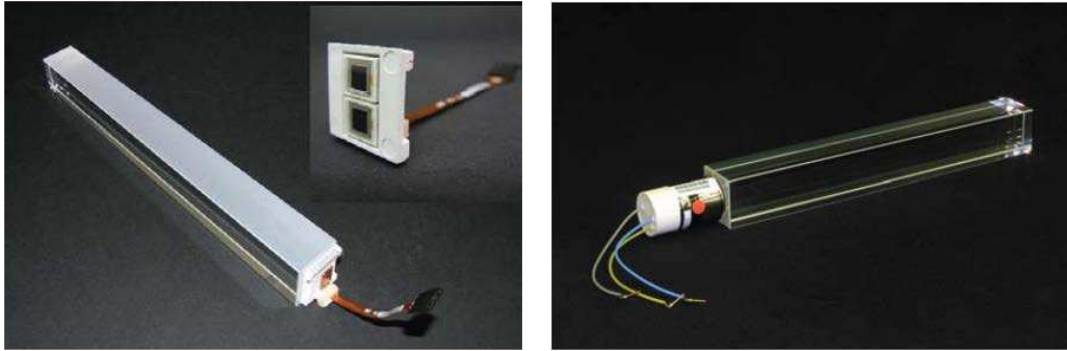


Figure 3.13: The ECAL  $PbW_04$  crystals with photodetectors attached. A barrel crystal with the upper face depolished and the APD capsule (left). An endcap crystal with VPT (right) [44].

for optimum light collection, however the truncated pyramidal shape makes light collection nonuniform along the length of the crystal. The needed uniformity is achieved by depolishing one of the crystal surfaces. Images of the barrel and endcap crystals with attached photodetectors are shown in Figure 3.13. The total crystal volume of the ECAL barrel is 8.14 m<sup>3</sup> and the weight is 67.4 t.

The ECAL endcaps (EE) cover the pseudorapidity range  $1.479 < |\eta| < 3.0$  and are at a distance of 315 cm from the interaction point. Each endcap is divided in two halves (Dees), with each Dee holding 3662 crystals grouped in  $5 \times 5$  super-crystals as illustrated in Figure 3.14. Crystals are arranged in a rectangular  $x - y$  grid, with the crystals pointing at a focus 1.3 m beyond the interaction point, giving off-pointing angles (with respect to the interaction vertex) ranging from 2° to 8°. The crystals in the endcaps have a front face cross section of  $28.6 \times 28.6$  mm<sup>2</sup> and  $30 \times 30$  mm<sup>2</sup> at the rear face. Each crystal is 220 mm in length, corresponding to a radiation length of  $24.7 X_0$ . The total endcaps crystal volume is 2.9 m<sup>3</sup> and the weight is 24 t.

The ECAL Preshower is a sampling calorimeter with two layers. Each layer consists of lead radiators that initiate electromagnetic showers from incoming electrons/photons, and silicon strip sensors, located after the radiator, that measure the



Figure 3.14: The CMS Electromagnetic calorimeter, endcap Dee.

deposited energy and transverse shower profile. The Preshower covers the fiducial region  $1.653 < |\eta| < 2.6$  and its total thickness is 20 cm. The material thickness of the first layer of preshower at  $\eta = 1.653$  is  $2 X_0$  and  $1X_0$  for the second layer. The energy measured by the Preshower is added to that measured by the crystal endcap to form the total electromagnetic energy deposited in the endcap by an incoming particle.

The ECAL energy resolution can be parameterized as a function of energy ( $E$ ) as follows [44]<sup>1</sup>:

$$\frac{\sigma(E)}{E} = \frac{S}{\sqrt{E}} \oplus \frac{N}{E} \oplus C, \quad (3.3)$$

where  $S$  is the stochastic term,  $N$  the noise term, and  $C$  the constant term. The

individual contributions are discussed below:

- **Stochastic term.** There are three main contributions. First, event-to-event fluctuations in the lateral shower containment, 1.5 %. Second, the photo-statistics results in a contribution of about 2.3 %. Last, fluctuations in the energy deposited in the preshower absorber with respect to the measurement in the preshower silicon detector result in a contribution of 5 %.
- **Noise term.** This contribution includes terms due to electronics noise, digitization noise, and pileup noise. Pileup noise occurs when additional particles, from multiple inelastic interactions, reach the calorimeter and their energy deposits overlap.
- **Constant term.** The most important contributions to the constant term are non-uniformity of the longitudinal light collection, crystal-to-crystal intercalibration errors, and leakage of energy from the back of the crystal.

The design ECAL energy resolution parameters are summarized in the Table 3.1 [48].

The ECAL energy resolution as a function of energy of the incident particle is illustrated in Figure 3.15 (right), as measured in electron beam tests [51]. Figure 3.15 (left) shows the contribution of the various terms to the total energy resolution as a function of energy [48].

### 3.2.4 Hadron calorimeter

The CMS hadron calorimeter (HCAL) [52] surrounds the ECAL system and is mostly located inside the CMS magnet coil, complemented by an additional layer just outside of the coil as illustrated in Figure 3.16. Limited by the available volume inside the magnet coil, the CMS HCAL is designed as a sampling calorimeter consisting of brass plates, serving as absorber, interleaved with plastic scintillator tiles, serving as the active medium. Brass has been chosen due to the fact that it has relatively short interaction length of  $\lambda_I = 16.42$  cm, it is relatively easy to manufacture, and it is a

---

<sup>1</sup>The symbol  $\oplus$  means sum in quadrature.

	Barrel ( $\eta = 0$ )	Endcaps ( $ \eta  = 2$ )
Contribution		
Electronics noise	0.15 GeV	0.75 GeV
Leakage current noise	0.03 GeV	–
Pileup noise	0.03 GeV	0.18 GeV
<b>Total Noise Term</b> (low luminosity)	<b>0.16</b> GeV	<b>0.77</b> GeV
Electronics noise	0.15 GeV	0.75 GeV
Leakage current noise	0.11 GeV	–
Pileup noise	0.10 GeV	0.53 GeV
<b>Total Noise Term</b> (high luminosity)	<b>0.21</b> GeV	<b>0.92</b> GeV
Containment	1.5 %	1.5 %
Photo-statistics	2.3 %	2.3 %
Preshower sampling	–	5.0 %
<b>Total Stochastic Term</b>	<b>2.7</b> %	<b>5.7</b> %
Inter-calibration	0.4 %	0.4 %
Longitudinal non-uniformity	0.3 %	0.3 %
Others	< 0.2 %	< 0.2 %
<b>Total Constant Term</b>	<b>0.55</b> %	<b>0.55</b> %

Table 3.1: Design ECAL energy resolution parameters [48] including different contributions to the terms in energy resolution parametrization (Eq. 3.3).

non-magnetic material. These properties make it an optimal absorber choice for the limited available volume and a strong magnetic field inside the CMS magnet. The active material consists of plastic scintillator tiles read out with embedded wavelength-shifting (WLS) fibers. The light from the WLS is delivered via a network of clear fibers, arranged in read-out towers, to hybrid photodiodes (HPD) [53].

The CMS HCAL consists of 4 subsystems, the hadron barrel calorimeter (HB), the hadron endcap calorimeter (HE), the hadron outer calorimeter (HO), and the hadron forward calorimeter (HF), as illustrated in Figure 3.16. Together with the ECAL they form the complete calorimeter system of the CMS.

The HB covers the central region within  $|\eta| < 1.4$  and consists of two halves each composed of 18 identical wedges covering  $20^\circ$  in  $\phi$ . The innermost and outermost absorber layer is made of stainless steel for structural strength. Each wedge consists of 17 active plastic scintillator tiles interleaved with 16 absorber plates. The individual scintillation tiles are machined to a size of  $\Delta\eta \times \Delta\phi = 0.087 \times 0.087$  (or  $5^\circ \times 5^\circ$ ) and

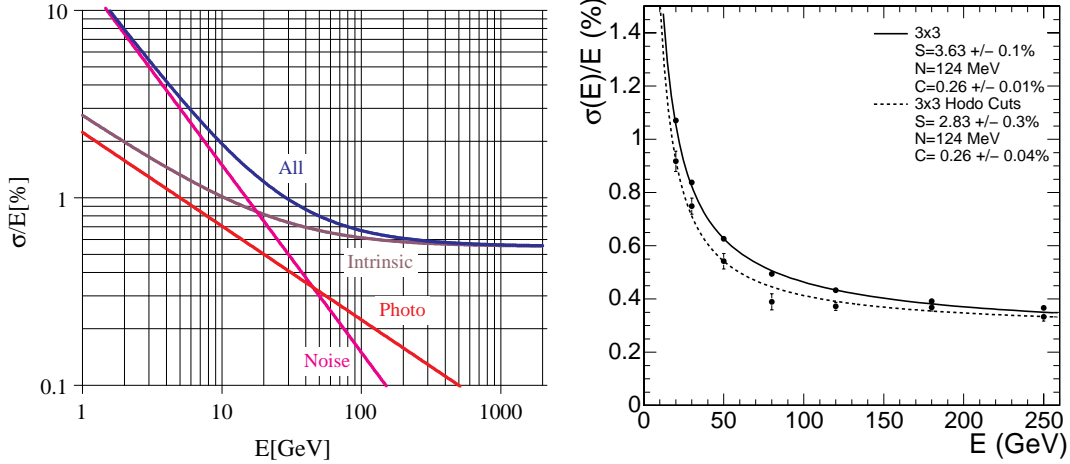


Figure 3.15: CMS ECAL energy resolution as a function of energy, as designed and as measured in test beams. Left, different contributions to the energy resolution [48]: the noise term (magenta, “Noise”), the stochastic term (red, “Photo”), the sum in quadrature of the stochastic and constant terms (brown, “Intrinsic”), and the total resolution (blue, “All”). Right, energy resolution measured in test beams as a function of energy. The resolution obtained with a  $3 \times 3$  array of crystals and an electron beam within  $20 \times 20 \text{ mm}^2$  around the center of the crystal (solid line), and within  $4 \times 4 \text{ mm}^2$  (dashed line) is shown [39].

form 2304 read-out towers. A schematic view of the tower mapping in the  $r - z$  plane is presented in Figure 3.17 [52]. The thickness of the brass plates is about 5 cm, while the scintillator plates are 3.7 mm thick, with exception of the innermost and outermost layer of scintillators which are 9 mm thick. The total absorber thickness is  $5.39 \lambda_I$  at  $\eta = 0$ , and is increasing to  $10.3 \lambda_I$  at  $|\eta| = 1.3$ .

The hadron outer calorimeter (HO) consists of scintillators with thickness of 10 mm, which are located just outside the magnet coil and cover the region  $|\eta| < 1.26$ . The first layer of magnetic field return yoke made of iron with a thickness of about 18 cm is used together with the HO scintillators as a tail-catcher for hadronic showers, with a geometry that follow the HCAL barrel tower geometry in  $\eta$  and  $\phi$ . The HO allows one to sample the energy from penetrating hadron showers leaking through the rear of the HB. This increases the effective thickness of the hadron calorimeter to

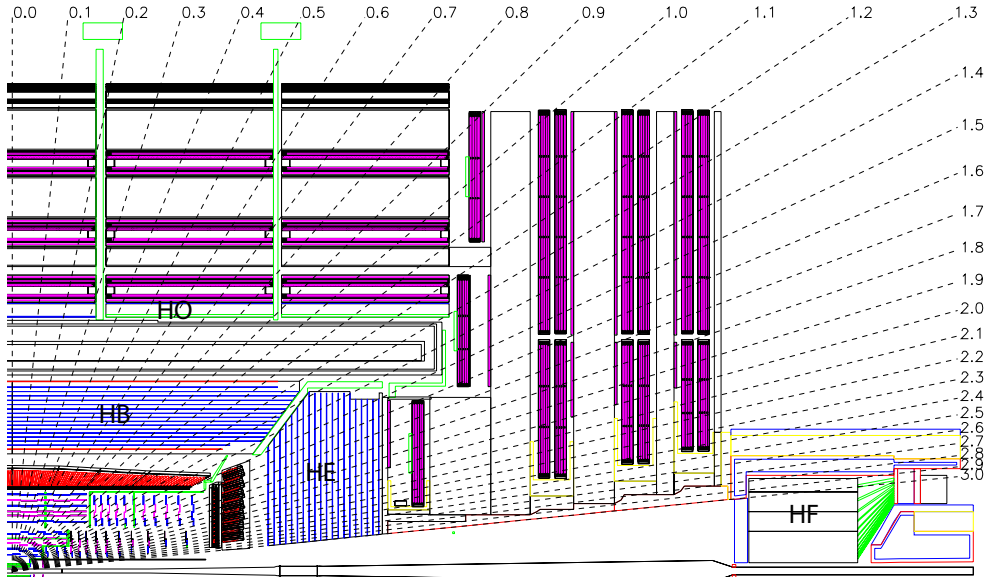


Figure 3.16: Longitudinal view of the CMS detector showing the locations of hadron barrel (HB), endcap (HE), outer (HO) and forward (HF) calorimeters.

over 10 interaction lengths.

The endcap hadron calorimeter (HE) covers the pseudorapidity region  $1.3 < |\eta| < 3.0$ , providing necessary overlap with the HB in the transition region between the barrel and endcap. There are 19 active plastic scintillator layers in the HE. Each scintillator layer is 3.7 mm thick and is interleaved with brass plates 78 mm thick. In the region  $1.3 < |\eta| < 1.73$  the tower size matches the one for the, namely  $\Delta\eta \times \Delta\phi = 0.087 \times 0.087$  (or  $5^\circ \times 5^\circ$ ). Beyond pseudorapidity of 1.74 the  $\phi$  size is 0.174 (or  $10^\circ$ ) and  $\eta$  size varies from 0.09 to 0.35. The read out in the HE allows for longitudinal segmentation, as illustrated in Figure 3.17 with differently colored regions [54].

The hadron forward calorimeters (HF), composed of steel and quartz fibers, are located 11.2 m from the interaction point and cover the pseudorapidity range  $3.0 < |\eta| < 5.0$ . The signal originates from the Cherenkov light [56] emitted in the quartz fibers, which is then channeled to the photomultipliers. The depth of the absorber is 1.65 m. The quartz fibers form a square grid with 5 mm spacing parallel to the beam line within the absorber material. The tower segmentation varies from

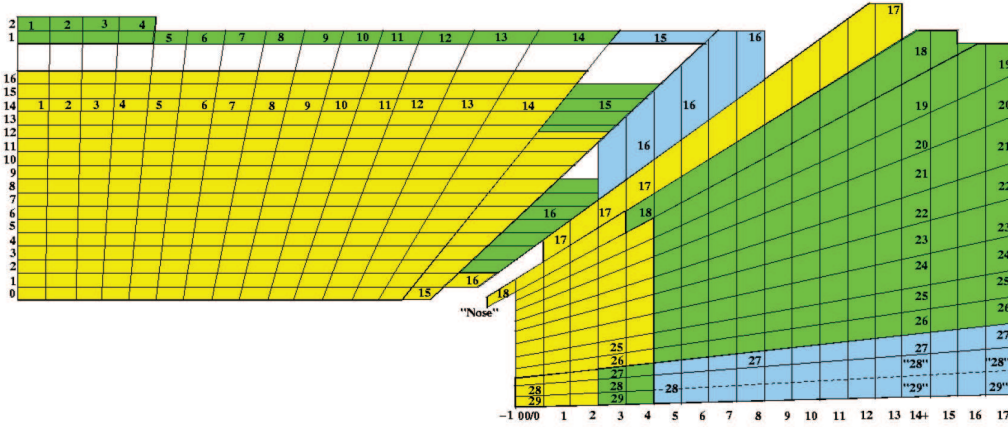


Figure 3.17: A schematic view of the HCAL tower mapping in the  $r - z$  plane for the barrel and endcap regions. Different colors correspond to different longitudinal read out segments.

$$\Delta\eta \times \Delta\phi = 0.175 \times 0.175 \text{ at } |\eta| = 3.0 \text{ to } \Delta\eta \times \Delta\phi = 0.3 \times 0.35 \text{ at } |\eta| = 5.0.$$

The energy resolution of the HCAL combined with the ECAL for hadronic jets can be parameterized as a function of the energy of the incident particle as follows:

$$\frac{\sigma(E)}{E} = \frac{S}{\sqrt{E}} \oplus C, \quad (3.4)$$

where  $S$  represents the stochastic term and  $C$  the constant term. Based on the beam test studies the values of the stochastic and constant terms for the HE and HB have been estimated to be  $S = 0.85 \text{ GeV}^{\frac{1}{2}}$  and  $C = 7.4\%$  [55]. The corresponding values for the HF are estimated to be  $S = 1.98 \text{ GeV}^{\frac{1}{2}}$  and  $C = 9\%$  [57].

### 3.2.5 The muon system

The CMS muon system [58] is designed to identify, measure momentum, and trigger on muons produced in CMS. Three types of gaseous detectors are used to detect muons: drift tubes (DT), cathode strip chambers (CSC), and resistive plate chambers (RPC). The entire muon system is located outside the magnet solenoid and covers a pseudorapidity region of  $|\eta| < 2.4$ . A general layout of the CMS muon system is

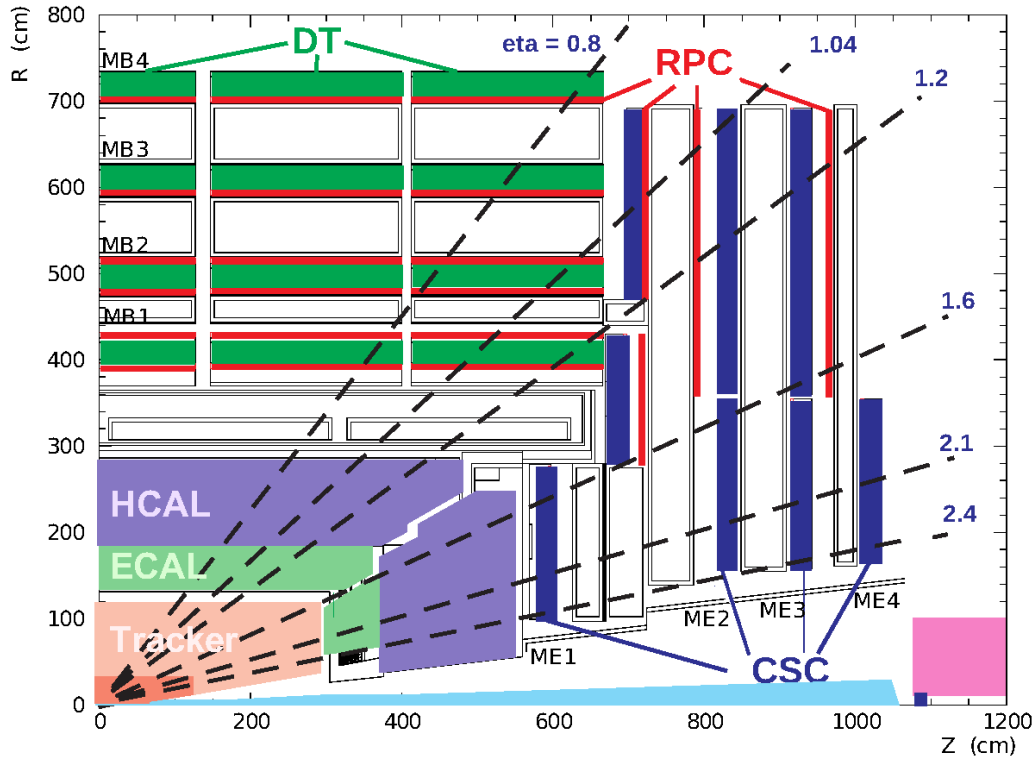


Figure 3.18: A schematic layout of the CMS Muon system, presenting the location of drift tubes (DT), cathode strip chambers (CSC) and resistive plate chambers (RPC) systems.

shown schematically in Figure 3.18.

The drift tube (DT) system consists of 250 chambers organized in 4 layers (stations) inside the magnetic return yoke, at radii of approximately 4.0, 4.9, 5.9 and 7.0 m from the beam axis (Figure 3.18). The DT system covers a pseudorapidity region of  $|\eta| < 1.2$ . Each of the 5 wheels of the Barrel Detector is divided into 12 sectors, with each sector covering  $\Delta\phi = 30^\circ$ , as can be seen in Figure 3.19. A drift-tube chamber is made of 3 (or 2) superlayers (SL), each made of 4 layers of rectangular drift cells staggered by half a cell (see Figure 3.20). Each station is designed to measure a muon's position with a precision of better than  $100 \mu\text{m}$  in  $\phi$  and a direction precision of about 1 mrad.

The cathode strip chambers system (CSC) covers the region  $0.9 < |\eta| < 2.4$  in

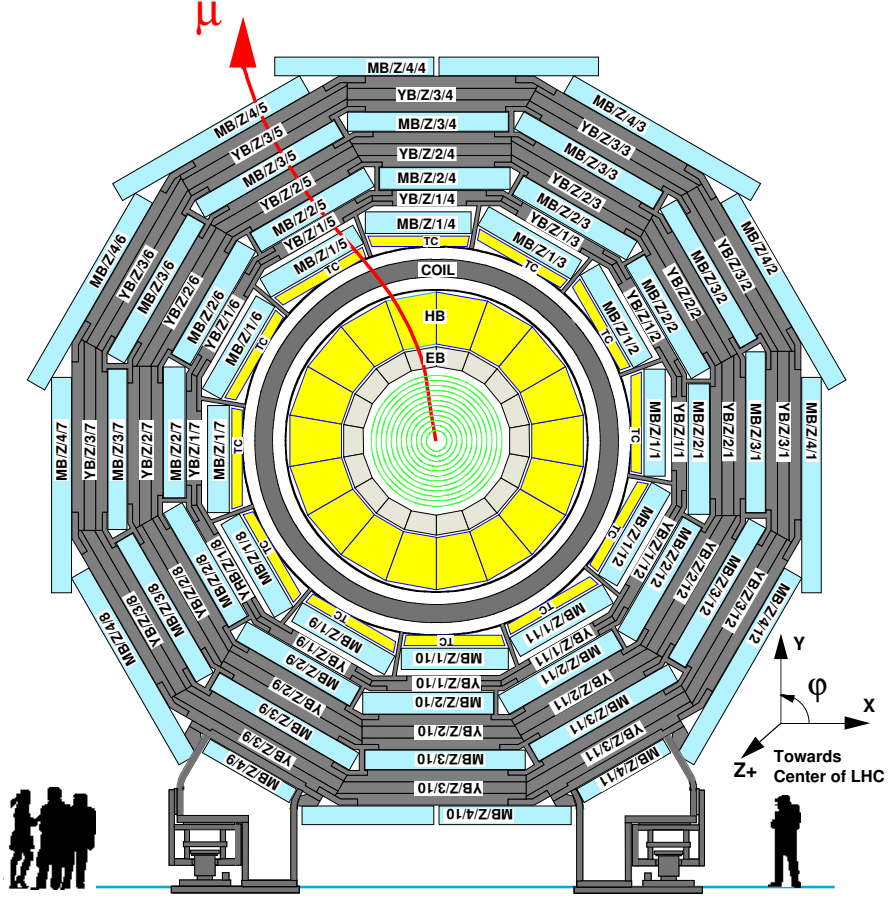


Figure 3.19: A schematic layout of the CMS Muon DT system.

pseudorapidity. The 468 CSC chambers are mounted on the CMS endcap discs. Each CSC is a multiwire proportional chamber composed of 6 anode wire planes interleaved with 7 cathode panels (Figure 3.21). Wires are oriented in the  $\phi$  direction and define a track's  $\eta$  coordinate, while strips on the cathode panels run radially at a constant  $\Delta\phi$  width. The muon  $\phi$  coordinate is obtained by interpolating among the positions of the strips where charge is induced, weighting each strip by the charge. A mixture of Ar, CO<sub>2</sub> and CF<sub>4</sub> is used as the gas in the chambers. In the region  $0.9 < |\eta| < 1.2$  the barrel drift tubes (DT) and CSC systems overlap, and muons are detected by both systems in this region.

The resistive plate chambers (RPC) system is complementary to the DT and

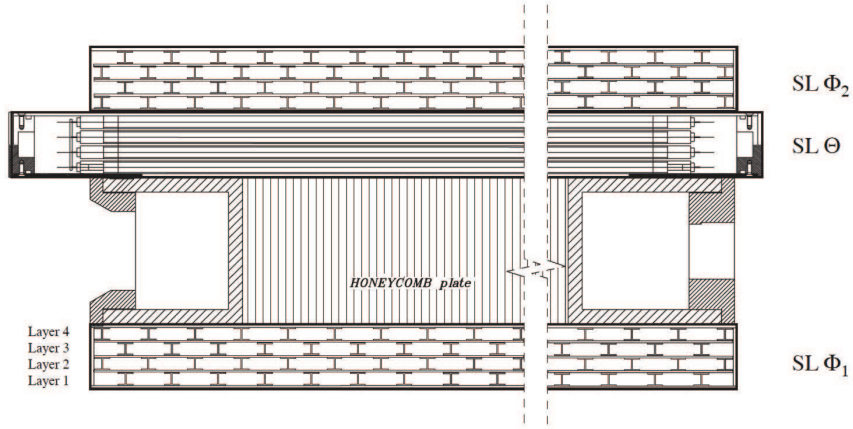


Figure 3.20: The layout of a DT chamber inside a muon barrel station.

CSC systems, in both barrel and endcap regions. Each RPC consists of a double-gap gaseous parallel-plate detector with common readout strips in the middle. The strips in the barrel run along the beam direction and radially in the endcap region. The combined system covers the region  $|\eta| < 1.6$ . The position of the RPC layers in the barrel and endcap regions can be seen in Figure 3.18, marked in red.

Muon momentum is measured by both the inner tracking system and the muon system. For transverse momenta below 200 GeV, the momentum measurements by the muon system are dominated by multiple scattering in the material in front of the first muon station, then the chamber spatial resolution starts to dominate at higher momenta. For low-momentum muons, the best momentum resolution is obtained in the silicon inner tracker system. Figure 3.22 illustrates the contribution to the momentum resolution as measured by the muon system only, by the tracker only, and the combined measurement, for two regions in pseudorapidity.

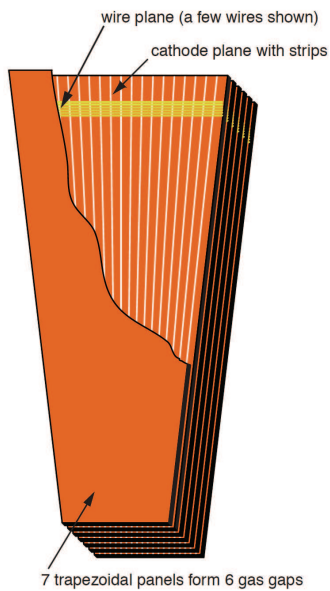


Figure 3.21: The layout of a CSC chamber made of 7 trapezoidal panels. The panels form 6 gas gaps with planes of sensitive anode wires. A few wires are shown to indicate the azimuthal direction. Strips of constant  $\Delta\phi$  run radially.

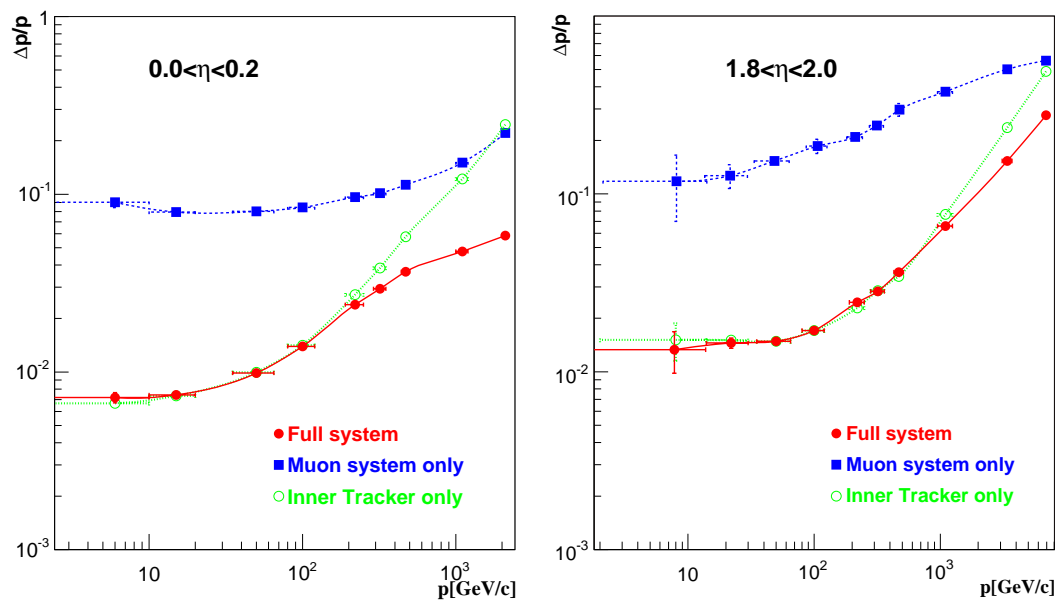


Figure 3.22: The muon momentum resolution as a function of momentum using the muon system only (blue), the inner tracker only (green), or both systems (red). Left, barrel  $|\eta| < 0.2$ . Right, endcap  $1.8 < |\eta| < 2.0$  [39].



## Chapter 4

# ECAL Laser Monitoring System

Irradiation of the ECAL crystals, mainly due to particles produced by proton-proton collisions at the LHC results in two distinct classes of radiation damage: electromagnetic damage due to high energy electrons and photons that recovers over time [60], and hadronic damage that is proportional to the number of nuclear interactions in the crystals and does not recover [61]. Electromagnetic damage leads to the formation of color centers that result in absorption bands that reduce the number of scintillation photons produced in the crystal that reach the photosensors. The color centers in  $PbWO_4$  are subject to thermal annealing at room temperature, so that there is a dynamic equilibrium between center creation and dissociation [60]. This results in a time-dependent, and dose rate dependent response. Due to the electromagnetic damage, response of each crystal generally decreases during LHC data taking in the first part of a fill, and recovers between fills as well as towards the end of the fill at lower luminosities under stable running conditions. Hadronic damage results from displacements in the crystal lattice caused by incident high energy charged hadrons, as well as neutrons.

During 2011 data taking period LHC operated at the luminosities  $\sim 10^{32} - 3.5 \times 10^{33} \text{ cm}^{-2}\text{s}^{-1}$ , equivalent to a dose-rate of  $\sim 0.01 \text{ Gy/h}$  for the ECAL barrel region and  $\sim 0.5 \text{ Gy/h}$  for the endcap region [48]. In such environment the effect of crystal transparency change becomes significant, on the order of a few %, and should be corrected for in order to maintain high precision of ECAL energy measurements.

The CMS ECAL utilizes a laser monitoring system [62] to monitor the transparency of the crystals, which affects the light seen by the crystal readout electronics. With this system, we can measure the change in transparency of each crystal contin-

uously during LHC running, with a very high precision. In this chapter the overview of the ECAL Laser Monitoring system and the data-flow strategy are presented. Special attention is paid to the data-flow structure and performance optimization, as also reported here [63].

## 4.1 ECAL crystal transparency change

The choice of lead tungstate crystals for the precision electromagnetic calorimeter was motivated by the fast decay time, light yield uniformity and radiation hardness, combined with sufficient light yield for a high resolution measurement of high energy electrons and photons. ECAL crystals are radiation hard against high integrated dose, but suffer from dose-rate dependent radiation damage which affects the transparency of the crystals by means of formation of color centers that absorb and scatter light, reducing the transparency of the crystals [59, 48].

The relation between the crystal response to an electromagnetic shower and to the injected laser light can be parametrized by the power law, for small changes in transparency [64]:

$$\frac{S}{S_0} = \left( \frac{R}{R_0} \right)^\alpha \quad (4.1)$$

where  $S/S_0$  is the normalized crystal response to electrons and  $R/R_0$  normalized response to the laser light as observed by the readout photosensors, and  $\alpha$  is the power law parameter. The initial values  $S_0$  and  $R_0$  correspond to measurements taken prior to the irradiation. This dependence was demonstrated in a series of test-beam studies as shown in Figure 4.1. The value of the power law parameter  $\alpha$  differs slightly from one crystal to another, and is affected by the crystal lattice impurities.

There are two major groups of crystals for which  $\alpha$  values differ significantly. This division is dictated by difference in the crystal growth techniques used at different manufacturing sites where crystals were produced. The majority of the crystals was produced at Bogoroditsk Techno-Chemical Plant in Tula, Russia, where the Czochralski method of crystal growing was used. The rest of the crystals were supplied by the

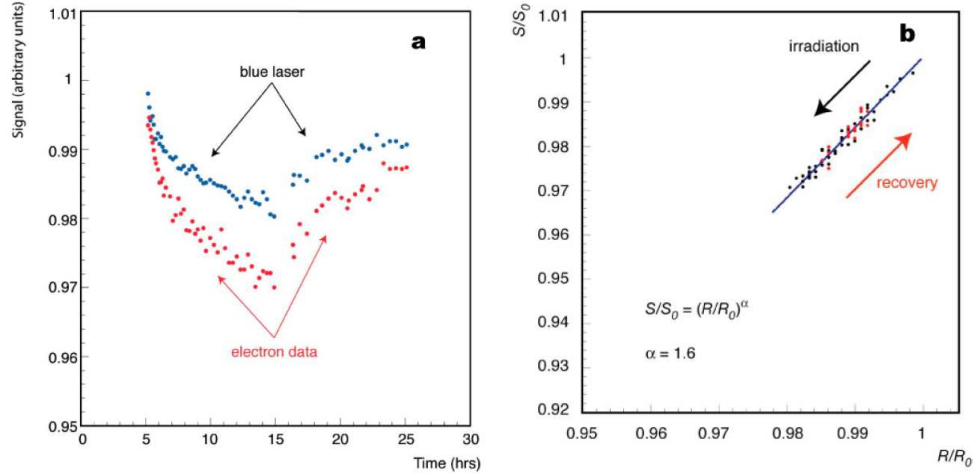


Figure 4.1: Irradiation with 120 GeV electrons and recovery for a single  $PbWO_4$  crystal: (a) upper curve shows APD response to laser injection at 440 nm (blue laser), and lower curve shows response to 120 GeV electrons; (b) the signal response  $S/S_0$  against the laser response  $R/R_0$  for the same data, where the line shows the fit for  $\alpha = 1.6$  [62].

Shanghai Institute of Ceramics, Shanghai, China, where the Bridgman-Stockbarger technique was employed. We refer to the former as the “Russian crystals” and to the latter as the “Chinese crystals.” The average  $\alpha$  value for Russian crystals is 1.52, while the average  $\alpha$  for Chinese crystals is 1.0 [65].

Radiation induced transparency change can significantly affect the signal amplitude read out from a crystal, thus distorting the measurement of the energy deposited by a particle in ECAL. This effect has to be corrected for. The correction is performed by measuring the change in crystal transparency to the laser light, which is then translated into the change in crystal response to the electromagnetic showers created by incident particles (see Equation 4.1).

## 4.2 ECAL Laser Monitoring System

The CMS ECAL Laser Monitoring System [62, 66] utilizes a powerful laser source to monitor the transparency of each crystals. Transparency changes recorded by the



Figure 4.2: Laser monitoring light source, Nd:YLF<sup>1</sup> pump laser and a tunable Ti:Sapphire<sup>2</sup> laser by Quantronix.

Laser Monitoring System are translated into the equivalent change in ECAL response to electrons (Equation 4.1). This information, collected for each crystal, is used to correct the reconstructed data for the effect of radiation-induced crystal transparency change.

The monitoring light source consists of three pairs of lasers. Each pair consists of a Nd:YLF<sup>1</sup> pump laser and a tunable Ti:Sapphire<sup>2</sup> laser, shown in Figure 4.2. All three Ti:Sapphire lasers provide a laser pulse intensity up to 1 mJ, corresponding to about 1.3 TeV energy deposition in  $PbWO_4$  crystals, at a repetition rate of up to 100 Hz. Two wavelengths are available from each pair of lasers. Two pairs provide 440 nm (blue) and 495 nm (green) and the third provides 709 nm (red) and 796 nm (infrared). The 440 nm wavelength was chosen as the monitoring wavelength as it provides the best linearity between the variations of crystal light output and transmittance [68].

In addition to the three pairs of lasers that are operational and have been in use for more than a decade, a new laser has been introduced and commissioned. This new laser is a diode pumped  $YVO_4$  laser<sup>1</sup> providing blue laser light at 447 nm, shown in Figure 4.3. In addition to satisfying the standard specifications of a light source

<sup>1</sup>All three pump lasers are model 527DQ-S Q-switched Nd:YLF lasers, a commercial product of Quantronix [67]. They provide frequency doubled laser pulses at 527 nm with pulse intensity up to 20 mJ at a repetition rate of up to 15 kHz.

<sup>2</sup>All three Ti:Sapphire lasers are custom made Proteus UV(SHG) dual wavelength lasers from Quantronix [67].



Figure 4.3: Laser monitoring light source, diode pumped YVO<sub>4</sub> laser<sup>1</sup> by Photonics.

for the CMS ECAL laser monitoring system, it is more compact, more robust and requires less maintenance. Thus, it represents the future generation of light sources that was phased in during 2012 operation, and will provide the main source of laser light in the future data taking.

The laser light is delivered from the light source to the surface of each individual crystal in the ECAL and to the PN diodes for reference, through a system of optical switches and optical fibers. The schematic light distribution system is shown in Figure 4.4.

By means of a 1x88 optical switch, the monitoring laser pulse is sent to one of the 88 light monitoring modules of the ECAL. Each light module consists of a group of crystals: 900 and 800 in the barrel region and around 900 in endcap region. At the same time, the light is sent to reference PN diodes located within the light monitoring modules.

Laser pulses are injected in the ECAL at a rate of 100 Hz, taking advantage of the gaps in LHC cycle used for kicker magnet operation. These LHC beam gaps occur every 89.924  $\mu$ s and last 3.17  $\mu$ s. Only about 1% of the beam gaps are used for ECAL monitoring data taking. During the LHC operation this sequence is performed continuously, providing monitoring data for each individual crystal every 20 minutes.

The Laser Monitoring data is read out from the detector electronics, reconstructed,

---

<sup>1</sup>Diode pumped YVO<sub>4</sub> laser DP2-447 from Photonics [69]. It provides frequency tripled laser pulse at 447 nm with pulse intensity of 1 mJ at a repetition rate of 100 Hz.

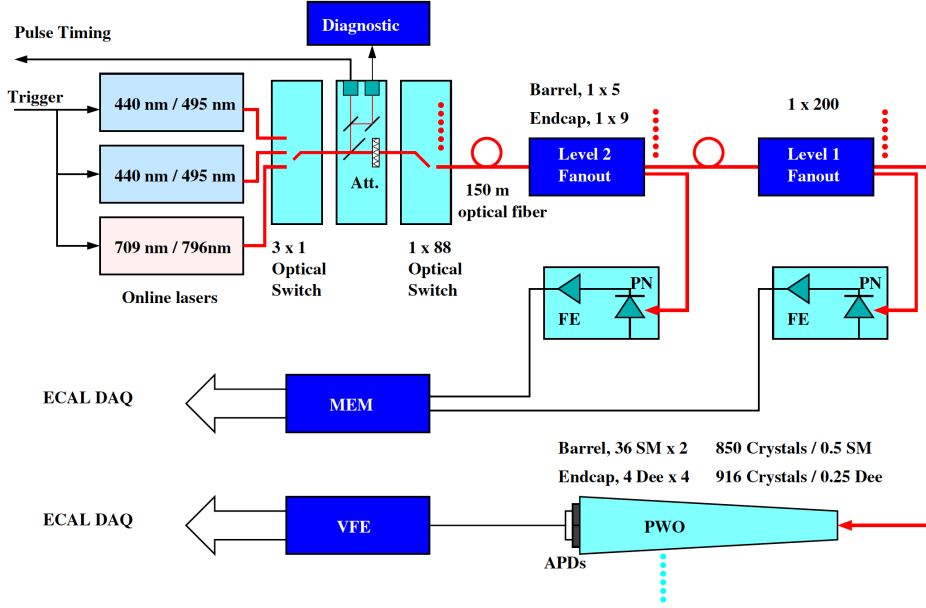


Figure 4.4: Laser Monitoring system is equipped with three pairs of lasers capable of providing the laser light at the frequencies of 440, 495, 709 and 796 nm. Through a system of optical switches and optical cables the light is delivered to the surface of each of the ECAL crystal and to the reference PN diodes.

analyzed and then compressed to the appropriate format convenient for offline event reconstruction. This data is used to correct the physics data for the effect of radiation-induced crystal transparency changes.

The Laser Monitoring System was tested in various test beam exercises as well as in the full global run environment of CMS. The system performs according to design specifications and has exhibited the required stability for maintaining optimal ECAL energy resolution [66](see Figure 4.9).

### 4.3 Laser Monitoring System data-flow

To apply transparency corrections to a physics event, only a reduced subset of the data collected by the laser monitoring system is required. However to ensure that the corrections are robust and consistent, and to correct for systematic effects the amount

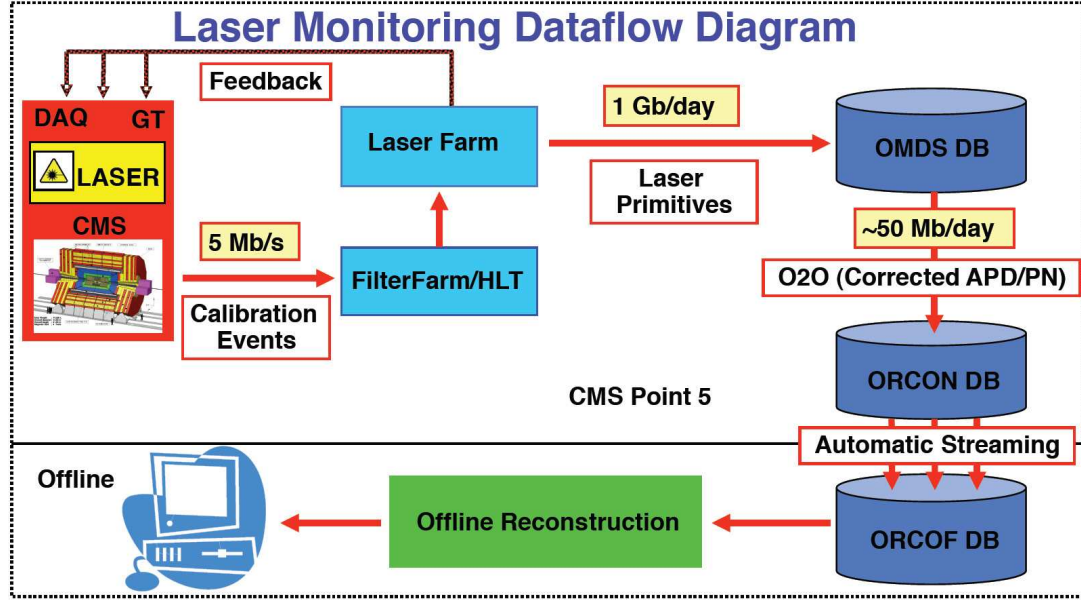


Figure 4.5: Laser Monitoring System data-flow showing steps and procedures involved in the production and transfer of laser corrections from the CMS detector to the offline reconstruction step.

of data handled at various steps of monitoring system operations is significant. To provide timely and consistent availability of monitoring data, a specialized data-flow was designed and implemented for the Laser Monitoring System operation.

### 4.3.1 General data-flow strategy

The schematic representation of the CMS ECAL Laser Monitoring System data-flow is presented in Figure 4.5. Laser monitoring data is taken during CMS running in approximately 1 % of the so-called “beam abort gaps” that occur every  $90\ \mu\text{s}$  in the LHC timing sequence. Event data arrives at the Filter Farm [70], containing, among other data, the ECAL laser monitoring data, which is sorted and then analyzed to extract transparency values. Transparency values represent the ratio of the response to the laser light of the crystal readout electronics to the response of the reference PN diodes. In the barrel Avalanche Photo Diodes (APD) are used for the crystal readout and Vacuum Photo Triodes (VPT) are used in the endcaps, as discussed in

Section 3.2.3. The main monitoring quantity is the APD/PN (VPT/PN) ratio.

After reconstruction and analysis on the Laser Farm, the laser data is stored in the Online Master Data Storage (OMDS) [71] database located in the underground cavern, which is the main Laser Data storage for service, commissioning and monitoring needs. Together with the APD/PN (VPT/PN) ratios this database stores various service parameters relevant for the Laser Monitoring System operation. This database also enables access to other conditions data needed for general CMS operations.

A reduced subset of the Laser Data, namely the APD/PN(VPT/PN) values for each crystal, which is required for the offline reconstruction, is transferred to the Offline Reconstruction Conditions Online subset (ORCON) [71] database in a procedure known as Online to Offline (O2O) transfer. During this (O2O) procedure, corrections and consistency checks are applied to the Laser Data.

The data stored in ORCON, located in underground cavern, is automatically transferred to the Offline Reconstruction Conditions DB Offline subset (ORCOFF) with the rest of the CMS Conditions Data [71].

The laser APD/PN ratios, reference values, and scale factors necessary to implement the transparency correction are kept in ORCOFF, and the radiation induced transparency corrections are applied in the offline reconstruction step.

### 4.3.2 Online database

The Online Master Data Storage (OMDS) database is a standard relational database. It is used to store all the conditions necessary for online detector operations and for the bookkeeping of the status of the detector. The data stored in OMDS is also used for data reprocessing, as needed.

All subsystems of CMS share the same database infrastructure with the Laser Monitoring System being one of them. The Laser Monitoring part of the DB is schematically presented in Figure 4.6. The logic of the entire OMDS is centered on the CMS Run (RUN iov), which uniquely defines a physical CMS run and connects the information from all the subsystems valid for a specific CMS run.

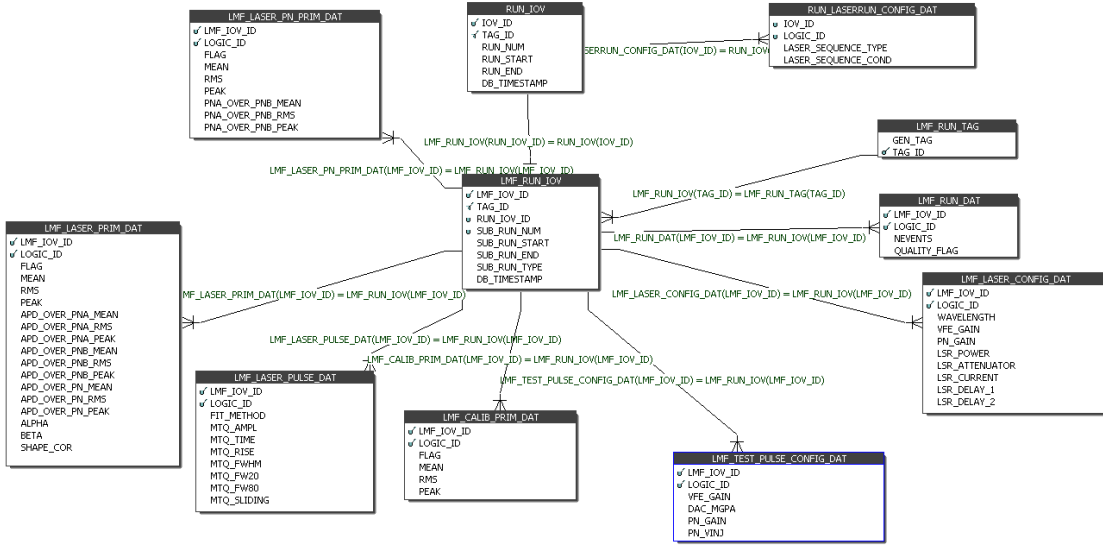


Figure 4.6: OMDS Laser Monitoring System database schematic representation. It is centered around the laser monitoring Run table `LMF_RUN_IOV`, which uniquely defines each laser monitoring system Run. The main transparency measurement information relevant for the data reconstruction is contained in the table `LMF_LASER_PRIM_DAT`.

At the center of the Laser Monitoring part of the OMDS is `LMF_RUN_IOV`, where LMF stands for Laser Monitoring Farm. It defines the time-interval for each run during which a certain set of conditions data is valid, and provides links to that conditions data.

Information about the LMF runs is stored in multiple database tables. The most relevant tables are `LMF_LASER_PRIM_DAT`, containing APD/PN (VPT/PN) values required for the offline reconstruction, and `LMF_LASER_PN_PRIM_DAT`, which provides detailed PN diode readout information.

### 4.3.3 Offline database

The offline database consists of two subsets: online (ORCON) and offline (ORCOFF). The offline subset is located in the main CERN Information Technology department facilities building in direct proximity to the CMS Analysis Facilities and Tier0 of the

CMS computing infrastructure [72], where the initial data reconstruction is taking place. This provides prompt access to conditions data at the reconstruction step for the data arriving from CMS. The online subset, on the other hand, is physically located in the CMS underground cavern providing a fast link to the OMDS. ORCON has exactly the same internal structure as ORCOFF; thus writing to ORCON is equivalent to writing directly to ORCOFF. Online and offline subsets are centrally synchronized, thus preventing each separate subsystem from writing directly to ORCOFF, and providing consistent data for offline reconstruction.

To fill ORCON/ORCOFF we use the POOL/CORAL [73] software framework which allows one to fill the database directly from C++ [74] objects stored within CMSSW [76] data framework. Each entity of the object has an Interval Of Validity (IOV) assigned to it. Access to the data is organized so that only the objects whose IOV contains the current time can be retrieved, thus providing conditions which were valid for that specific moment in detector history.

Each ECAL crystal is flashed with laser light on average every 20 min. On this timescale, the transparency change can be linearly interpolated. In practice, the value of each crystal’s transparency is interpolated from the last three transparency measurements. This requires that we store for each crystal the current transparency value and the previous two, as well as the time when these values were measured. As crystals belonging to the same light monitoring region are flashed with laser pulses at the same time, it is enough to keep only the time for the measurement of each monitoring region and not for each crystal individually. For the offline reconstruction, reference values of the crystal transparencies are required together with the  $\alpha$  values for each crystal. Figure 4.7 shows the three objects which represent the Laser Monitoring part of ORCON/ORCOFF. One can easily see the level of reduction from the OMDS schema to ORCON/ORCOFF objects.

<b>EcalLaserAPDPNRef</b>		<b>EcalLaserAlphas</b>		<b>EcalLaserAPDPNRatios</b>	
Channel ID		Channel ID		Channel ID	
APD/PN		Alpha		Group ID	

Figure 4.7: ORCON/ORCOFF Laser Monitoring System objects representation. EcalLaserAPDPNRef is the initial value of the APD/PN ratio for each crystal. EcalLaserAlpha is the value of  $\alpha$  parameter for each crystal. Finally EcalLaserAPDPNRatios are the last three values of the APD/PN for each crystal together with corresponding timestamps for each measurement.

## 4.4 Data flow specifications and optimization

The Laser Primitive data is information stored for each individual ECAL crystal which is frequently updated, unlike other condition data such as temperature, voltage or any other run conditions which are updated on the run by run basis or even less frequently. Every  $\sim 10$  sec a new light monitoring region is read out, which puts a much stricter requirement on the speed of the laser primitives manipulation in the database transfers. Validation tests showed that using the standard upload/readout procedure in which records for each crystal are updated or read out in a separate database query results in significant delays. It requires on the order of  $\sim 10$  sec to populate the online database with the measurements from one light monitoring region, thus making it almost impossible to keep up with the data accumulation rate.

To improve performance, special OCCI [75] optimization techniques for bulk writing setDataBuffer, executeArrayUpdate and bulk reading setPrefetchRowCount methods were used [63]. In one update, all values contained in an array are written to the database, and in one transaction 1000 values are retrieved. This resulted in a significant reduction of multiple network round-trips to the server.

For testing purposes the data of a full transparency measurement cycle of the ECAL barrel, i.e.  $1700 \times 36$  (61200) channels was used. For each channel APD, PN, and APD/PN values were transferred to corresponding tables. The results before and after optimization are summarized in Table 4.1. The performance after optimization is well within the required update frequencies and enables a smooth laser monitoring

data flow operation.

	Before optimization	After optimization
Writing	75 sec	2 sec
Reading	22 sec	3 sec

Table 4.1: Online database access optimization results. Time in sec required to transfer the laser monitoring data for all the crystals in the ECAL barrel. The optimization implemented significantly reduces the time required to access database.

## 4.5 Summary

The CMS ECAL Laser Monitoring System is designed to monitor the changes in the crystal response due to radiation induced damage. The precision of the crystal transparency measurement is found to be below 0.2%, meeting the design goal required to keep the resolution of the ECAL at the 0.5% level [66]. The optimization of the data handling brought the data-flow well within the design requirements.

During the data taking the laser monitoring system performed according to the specifications and accurate crystal transparency corrections have been obtained. Figure 4.8 shows the time variation of the reconstructed  $\pi^0$  mass peak position with and without laser correction applied [77]. Figure 4.9 shows the evolution over time of the ratio of electron energy  $E$ , measured in the ECAL barrel, to the electron momentum  $p$ , measured in the tracker, for electrons coming from  $W \rightarrow e\nu$  decays, both before and after corrections to the ECAL crystal response due to transparency loss are applied. Figure 4.10 shows the  $e^+e^-$  invariant mass distributions for the  $Z \rightarrow e^+e^-$  candidate events with and without ECAL intercalibration applied, and with and without ECAL crystal transparency corrections applied [78]. These cross-checks show that the laser corrections work as expected.

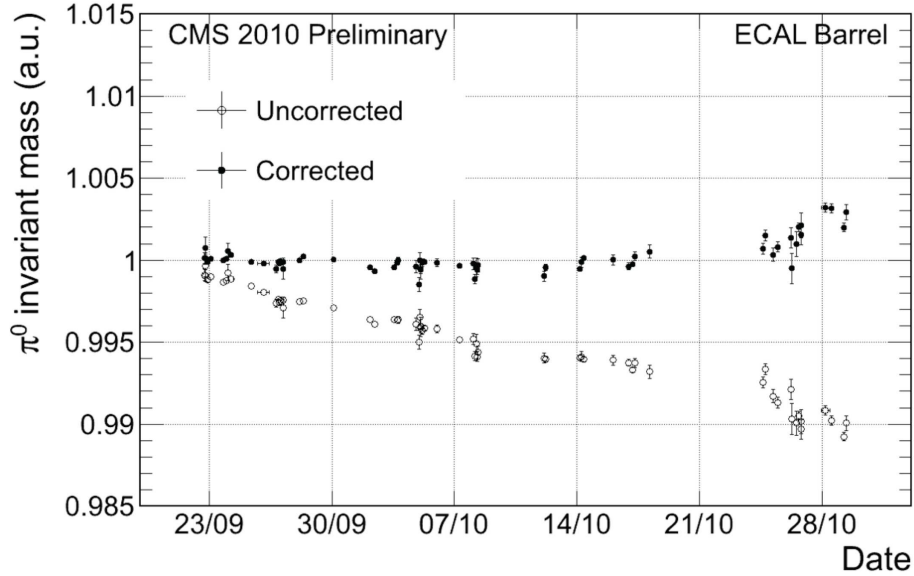


Figure 4.8: Reconstructed  $\pi^0$  mass peak position as a function of time both before and after the crystal transparency correction is applied. The invariant mass is normalized to unity at the start of the data taking period under consideration [77].

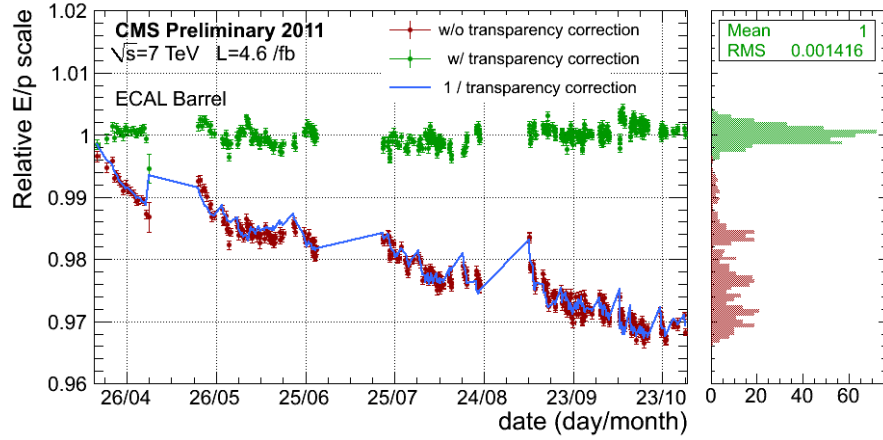


Figure 4.9: Evolution over time of the ratio of electron energy  $E$ , measured in the ECAL barrel, to the electron momentum  $p$ , measured in the tracker, for electrons coming from  $W \rightarrow e\nu$  decays, both before and after corrections to the ECAL crystal response due to transparency loss are applied. The ratio is normalized to unity at the start of the data taking period under consideration [78].

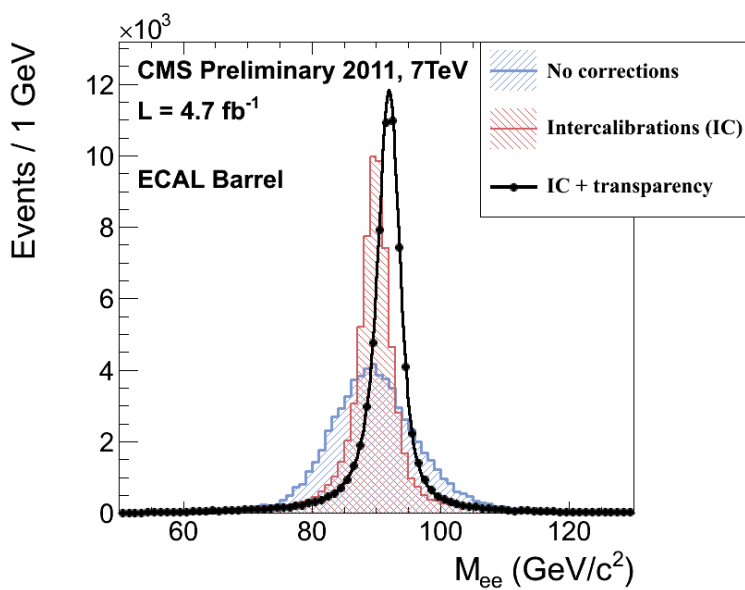


Figure 4.10: Di-electron invariant mass distribution for the  $Z \rightarrow ee$  candidate events with and without ECAL inter-calibration applied, and with and without ECAL crystal transparency corrections applied [78].

# Chapter 5

## Electron Reconstruction

### 5.1 Electron reconstruction overview

In the CMS experiment, electrons are reconstructed as a combination of a track in the silicon tracker and a supercluster (SC) (cluster of clusters) in the electromagnetic calorimeter [80].

Electron reconstruction starts with a seed supercluster in the ECAL which satisfies basic preselection requirements [81]. Having identified a seed SC a helix is propagated to the interaction vertex based on the energy measured by the SC and assuming both charge hypotheses. The algorithm then searches for hits in the pixel vertex detector that can be matched to the helix trajectory. If the algorithm identifies pixel hits compatible with the electron hypothesis, then a search for a compatible track in the silicon tracker is initiated [82].

This seeding strategy is complemented by a tracker-driven seed finding algorithm. The tracker-driven seeding starts from high purity tracks, and makes use of “particle flow” clustering [83].

A dedicated tracking method is used for electron track reconstruction based on the “Gaussian-Sum Filter” (GSF) [84, 85] fit procedure which relies on a proper modeling of electron radiative energy loss in the tracker material.

In the tracker-driven reconstruction algorithm, an ECAL SC is built based on the GSF track. A tangent is then extrapolated from each track measurement towards the ECAL to identify a possible corresponding bremsstrahlung photon. The GSF track is extrapolated from its outermost position into the ECAL to identify a candidate

electron cluster.

For both reconstruction algorithms, after the GSF track and the SC corresponding to it have been reconstructed, a loose preselection criteria is applied to reduce the contribution from QCD jets. The electron momentum is assigned as a weighted average of the momentum measured by the tracker and the energy measured by the ECAL SC, where the weighting depends on the quality of the track and quality of the SC.

Now that we have a general picture of the electron reconstruction strategy I will go into more detail on the SC and track reconstruction, in particular for ECAL-driven electrons, as the analysis described in this thesis relies mainly on electrons of this type. I will also go into more detail on the preselection criteria and momentum determination in the following sections.

## 5.2 ECAL clustering

The energy deposited in the electromagnetic calorimeter by the particles traveling from the interaction point is converted into the scintillating light produced by the ECAL crystals. To measure the energy deposited by a particle in the ECAL, individual crystal responses have to be clustered together. In this so-called clustering procedure groups of crystals with energies above a certain threshold are arranged together to form basic clusters (BCs). Basic clusters are subsequently grouped using a bremsstrahlung hypothesis to form superclusters (SCs).

Energies deposited in the ECAL by individual particles form a pattern that is spread over a number of neighboring crystals. Bremsstrahlung emitted by the electrons traversing the silicon tracking detector is spread in the  $\phi$  direction due to the bending of the electron trajectory by the solenoidal magnetic field. This includes the electrons and positrons produced by conversion of bremsstrahlung photons as well.

Due to the different geometric arrangement of the crystals in the barrel and endcap regions, we apply different clustering algorithms to them. The algorithms in both regions group crystals associated with individual electromagnetic showers. The

showers in a large window in  $\phi$  direction but close in  $\eta$  are collected together to form superclusters. This allows the showers produced by bremsstrahlung photons to be included in the resulting superclusters.

### 5.2.1 Clustering in the barrel region

In the barrel region crystals are clustered together using the so-called Hybrid algorithm. This algorithm exploits the  $\eta - \phi$  geometry of energy deposits in the ECAL crystals. Crystals are grouped together to collect the energy for individual showers, as well as for the sets of showers compatible with a bremsstrahlung hypothesis. Crystals within a rectangular window extended in the  $\phi$  direction are considered as candidates for the cluster. The steps that are performed by the algorithm on the set of crystals, sorted in descending order according to their energy, are summarized below:

- Test the  $E_T$  of the next crystal that does not already belong to a cluster. To avoid obvious noise contamination and low energy backgrounds, the crystal  $E_T$  has to be above a threshold; then if  $E_T > E_T^{hybseed}$ , this crystal can seed the clustering process. If not, the clustering process terminates.
- Construct a  $3 \times 1$  domino of crystals in  $\eta - \phi$ . If  $E_{domino} > E_{wing}$  then extend the domino to  $5 \times 1$  crystals symmetrically about the seed crystal. The default value of  $E_{wing} = 0.0$  ensures that  $5 \times 1$  dominoes are always built.
- Repeat the second step for all crystals with the same  $\eta$  as the seed crystal and within  $\phi < \phi_{road}$ . To be included in the cluster, dominoes must satisfy  $E_{domino} > E_{thresh}$ .
- Group the remaining dominoes into local energy maxima, which are connected by side in the  $\phi$  direction and then remove all dominoes belonging to any local maxima with a highest energy domino below  $E_{seed}$ .

Values of the parameters mentioned above and used in the Hybrid clustering algorithm reconstruction are summarized in Table 5.1. The result of the procedure is

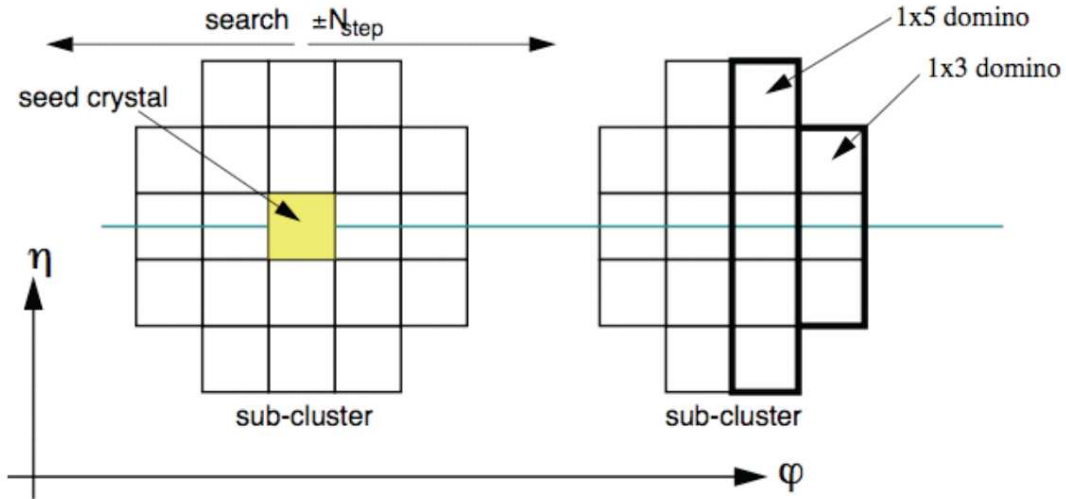


Figure 5.1: An illustration of the Hybrid clustering algorithm used in the ECAL barrel region.

Parameter	Value
$\phi_{road}$	17 crystals
$E_T^{hybseed}$	1 GeV
$E_{wing}$	0 GeV
$E_{thresh}$	0.1 GeV
$E_{seed}$	0.35 GeV

Table 5.1: Values of the Hybrid clustering algorithm parameters.

illustrated in Figure 5.1. The hybrid supercluster is made up of a series of sub-clusters at constant  $\eta$  but spread in the  $\phi$ -direction. Each sub-cluster can be well contained in  $5 \times 5$  crystals.

### 5.2.2 Clustering in the endcap

Since the crystals in the endcap are not arranged in an  $\eta - \phi$  geometry as in the barrel, the hybrid algorithm cannot be applied there. The same idea of collecting energy deposits within a window in  $\eta$  and  $\phi$  must be implemented differently. This is achieved by the so-called Multi  $5 \times 5$  algorithm, which operates on the set of crystals sorted in descending order of  $E_T$ , as follows:

- Test the  $E_T$  of the next crystal that does not already belong to a cluster. If  $E_T > E_T^{seed}$  then this crystal can seed the clustering process. If not, the clustering process terminates.
- Continue if the crystal is a local maximum in energy by comparing its energy to its four adjacent neighbors (the ones that share a side with it, such that the crystal and its neighbors form a cross pattern). If the crystal is not a local maximum, return to the previous step.
- Construct a  $5 \times 5$  matrix of crystals about the seed, including only crystals that do not already belong to a cluster.

To allow closely overlapping showers due to bremsstrahlung to be collected, the outer 16 crystals of the  $5 \times 5$  matrix may seed a new matrix, thus the matrices can overlap. However, no crystal that is already included in a cluster may belong to another.

To produce the final set of clusters by recovering bremsstrahlung, a rectangular window in  $\eta$  and  $\phi$ , which is extended in the  $\phi$ -direction is created around energy deposits with a transverse energy above  $E_T^{seed\ bc}$ . Other energy deposits falling within the window are added to form the cluster. This procedure is performed in descending order of  $E_T$  of the energy deposits and an energy deposit may only belong to one cluster. Values of the parameters used in the Multi  $5 \times 5$  clustering algorithm are summarized in Table 5.2

An example of the result of the processes is shown in Figure 5.2. This illustrates the collection of two overlapping energy deposits that have been identified by the algorithm and grouped. The highest  $E_T$  crystal, which is a local maximum, is clustered first resulting in a full  $5 \times 5$  matrix. The second local maximum has already been clustered, however it is still eligible to seed a new  $5 \times 5$  matrix, this one is constructed using the remaining free crystals.

Parameter	Value
$E_T^{seed}$	0.18 GeV
$E_T^{seed\ bc}$	1.0 GeV
$\eta^{road}$	0.14 rad
$\phi^{road}$	0.6 rad

Table 5.2: Values of the Multi5×5 clustering algorithm parameters.

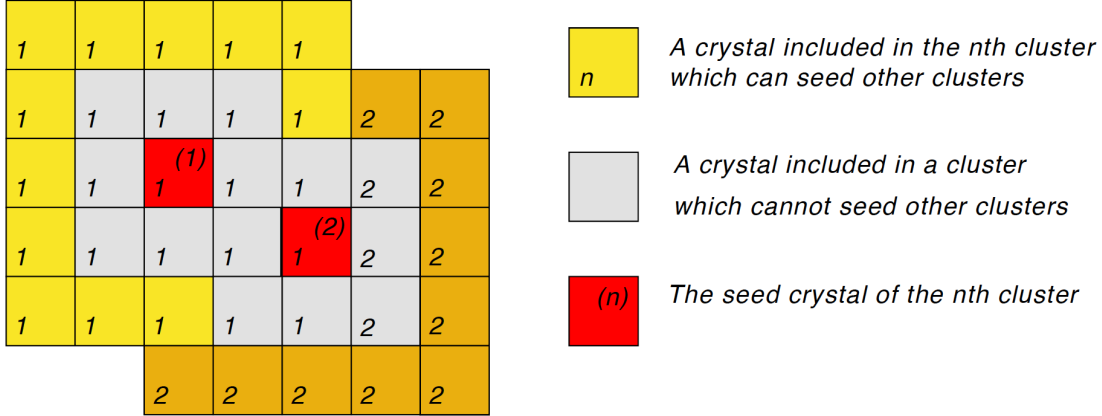


Figure 5.2: An illustration of two overlapping Multi5×5 clusters. Crystals in yellow are eligible to seed further Multi5×5 clusters provided they are local maxima in energy.

### 5.2.3 Recovery of energy deposited in preshower

In the endcap, the region  $1.6 < |\eta| < 2.6$  is covered by the preshower detector (described in Section 3.2.3). Electrons and photons reconstructed in this region will typically deposit some fraction of their energy in the preshower, so this energy must be measured and added to each cluster. This is done by summing the energy from the preshower strips that intersect trajectories extrapolated from the primary vertex to each energy deposit in the ECAL. This energy sum is added to each endcap supercluster before any energy scale corrections are applied.

### 5.2.4 Energy reconstruction

Energies in the ECAL are estimated as follows [87]:

$$E = F \sum_{\text{cluster}} G \times S_i(t) \times c_i \times A_i \quad (5.1)$$

where the sum is over the crystals belonging to the electromagnetic cluster,  $A_i$  is the reconstructed pulse amplitude in crystal  $i$  in ADC counts,  $c_i$  is the corresponding inter-calibration constant, and  $G$  is a global ECAL energy scale (measured in GeV/ADC). The inter-calibration constants are derived by using a number of in-situ methods:  $\pi^0 \rightarrow \gamma\gamma$  and  $\eta \rightarrow \gamma\gamma$  decays; the  $\phi$ -symmetry of energy deposition in ECAL; and a comparison of E/p for electrons from  $W \rightarrow e\nu$  decays. Finally, a combination of these methods is used to assign the inter-calibration constants [88]. The term  $S_i(t)$  is the laser monitoring correction to the crystal amplitude due to the radiation-induced transparency change at the event time  $t$ , as described in Section 4.3. As described below,  $F$  is the product of three individual energy correction factors, which are applied sequentially to the Hybrid superclusters in the barrel (EB). Two out of the three correction factors are applied to SCs reconstructed in the endcap region ( $C_{EB}(\eta)$  is applied only to the barrel superclusters, see below). The three correction factors listed in the order they are applied to the supercluster energies are:

- the  $C_{EB}(\eta)$  factor, which is used to compensate for energy leakage from the lateral faces of the EB crystals. This correction only applies to EB clusters, as only ECAL barrel crystals significantly change their orientation with respect to the magnetic field from the central region towards the endcap region, thus affecting the shower formation within the crystals;
- the  $f(\mathcal{R}_{brem})$  correction, where  $\mathcal{R}_{brem}$  describes the size of the SC in the  $\phi$  direction with respect to the  $\eta$  direction, compensates the response of the clustering algorithm to the showers formed by particles traveling through the tracker material;
- the residual correction  $f(E_T, \eta)$ , which is applied to all reconstructed superclusters, to compensate for any remaining effects coming from the non-linear distribution of material in the detector, and any remaining energy dependence.

As mentioned above, the energy loss due to electron bremsstrahlung is characterized by the variable  $\mathcal{R}_{brem}$  defined as follows:

$$\mathcal{R}_{brem} = \frac{\sigma_\phi}{\sigma_\eta} = \frac{\sum_{cluster} \sqrt{\frac{E_i}{E_{SC}}(\phi_i - \phi_{SC})^2}}{\sum_{cluster} \sqrt{\frac{E_i}{E_{SC}}(\eta_i - \eta_{SC})^2}} \quad (5.2)$$

Due to the solenoidal field, the energy deposited in the ECAL is spread out in the  $\phi$  direction, while no spread occurs in the  $\eta$  direction.  $\sigma_\eta$  describes the natural (not affected by magnetic field) shower size. Normalization of  $\sigma_\phi$  to  $\sigma_\eta$  allows one to treat the showers in various energy ranges, all in a single approach.

In an ideal case, this correction should recover all energy losses in the tracker. However, because of the nonuniform distribution of material in the detector, and a visible dependence on the energy, some additional correction is needed, and has to be parameterized in terms of the transverse energy  $E_T$  and the pseudorapidity  $\eta$ , which is done by  $f(E_T, \eta)$  mentioned above.

That summarizes the process of energy association to a supercluster reconstructed in the ECAL, and the corresponding energy correction strategy. It should be noted that among the parameters that enter the energy calculation formula, the energy scale,  $G$ , is the parameter that has to be validated in data, and represents a set of two numbers, one for the barrel and one for endcap. I will describe in more detail the strategy to validate the energy scale in Section 7.1, and present the results of this study.

### 5.3 Track reconstruction

Having reconstructed ECAL superclusters we proceed to the next step in reconstruction, which is the track reconstruction. The superclusters are used to select trajectory seeds built from the combination of hits from the innermost tracker layers. Superclusters are preselected by applying a 4 GeV threshold on the supercluster transverse energy ( $E_T$ ) and a hadronic veto  $H/E < 0.15$ , where  $H/E$  is the ratio of the hadronic

	1st windows		2nd windows			
	$\delta z$ or $\delta r_T$	$\delta\phi$	$\delta z$	$\delta r_T(PFX)$	$\delta r_T(TEC)$	$\delta\phi$
10 GeV	$\pm 5\sigma z$	[-0.14;0.08] rad	$\pm 0.09$ cm	$\pm 0.15$ cm	$\pm 0.2$ cm	$\pm 4$ mrad
35 GeV	$\pm 5\sigma z$	[-0.05;0.03] rad	$\pm 0.09$ cm	$\pm 0.15$ cm	$\pm 0.2$ cm	$\pm 4$ mrad

Table 5.3: Definition of the seed matching windows. The  $E_T$ -dependent first  $\phi$  window is given for 10 and 35 GeV.  $\sigma_z$  is the beam spot width along the  $z$  axis.

energy in a cone of  $\Delta R = 0.15$  behind the supercluster position over the supercluster energy.

The seeding algorithm takes advantage of the fact that the supercluster position is on the helix of the initial electron trajectory. The seeds are found by back-propagating the helix through the magnetic field toward the innermost part of the tracker. This approach allows significant reduction in the background from jets faking electrons. Trajectory seeds are identified by the two hits in the pixel and TEC detectors which are matched to the helix in windows in  $\phi$  and  $z$  (or transverse radius  $r_T$  in the forward region). The first layer windows are made loose in both  $\phi$  and  $z$  (or  $r_T$ ) in order to account for residual material effects and for the beam spot position uncertainty along the  $z$  axis. Once a hit is matched on the first layer, this information is used to refine the helix parameters and a second hit is looked for in the second layer using smaller windows. The contamination from jets faking electrons is further reduced using  $E_T$ -dependent window definitions in the first layer. The matching window definitions are summarized in Table 5.3.

Electron seeds are then used to initiate a dedicated electron track building and fitting procedure in order to best handle the effect of bremsstrahlung energy loss. The track finding is based on a Gaussian-Sum Filter (GSF) as described in [84], with a dedicated Bethe-Heitler [89] modeling of the electron energy losses. The combinatorics are limited by requiring at most 5 candidate trajectories at each tracker layer, and at most one layer with a missing hit. This track reconstruction procedure allows one to collect hits up to the ECAL, as opposed to the standard Kalman Filter [86] method

where the reconstruction of an electron trajectory would stop whenever a significant change of curvature occurs due to bremsstrahlung radiation.

The hits collected in the procedure described above are passed to a GSF for the final estimation of the track parameters. In such a fit, the energy loss in each layer is approximated by a weighted sum of Gaussian distributions.

The difference between the momentum magnitude at the outermost track position and at the innermost track position is an estimate of the true fraction of energy radiated by the electron. The normalized difference called  $f_{brem}$  is used in the electron classification and electron momentum estimation as discussed in Section 5.4.2.

## 5.4 Preselection and energy determination

### 5.4.1 Preselection

Electron candidates are formed by the association of a supercluster and the corresponding GSF track. In order to reduce the probability of a jet to be reconstructed as an electron a loose preselection is applied to all electron candidates. This preselection is kept loose enough in order not to perturb any analysis level selection criteria.

The following cuts have been already applied at the seeding level:

- $E_T > 4$  GeV, where  $E_T$  is the supercluster transverse energy,
- $H/E < 0.15$ , where  $H$  is the energy deposited in the HCAL towers in a cone of radius  $\Delta R = 0.15$  centered on the electromagnetic supercluster position, and  $E$  is the energy of the electromagnetic supercluster.

In addition to the selection applied at the seeding step, the following track-supercluster matching requirements are applied on electron candidates:

- $|\Delta\eta_{in}| = |\eta_{sc} - \eta_{in}^{extrap}| < 0.02$ , where  $\eta_{sc}$  is the energy weighted position in  $\eta$  of the supercluster and  $\eta_{in}^{extrap}$  is the coordinate of the position of closest approach to the supercluster position, extrapolating from the innermost track position and direction,

- $|\Delta\phi_{in}| = |\phi_{sc} - \phi_{in}^{extrap}| < 0.15$ , where  $\phi_{sc}$  is the energy weighted position in  $\phi$  of the supercluster and  $\phi_{in}^{extrap}$  is the coordinate of the position of closest approach to the supercluster position, extrapolating from the innermost track position and direction.

### 5.4.2 Momentum determination

Both ECAL and tracker measurements are used to obtain the electron momentum magnitude. The momentum estimates from the electron track are particularly useful for low energy electrons and for electrons that are close to the ECAL crack regions.

Electrons are divided into several classes based on the observed number of clusters inside the supercluster in the ECAL and on the measured bremsstrahlung fraction by the tracker. The classes are defined as follows:

- “golden,” or “low bredding” electrons with a reconstructed track well-matched to the supercluster:
  - a supercluster formed by a single cluster (i.e., without any observed bremsstrahlung induced sub-cluster),
  - a ratio  $E/p > 0.9$ , where  $E$  denotes the energy of ECAL supercluster and  $p$  the momentum of the associated track,
  - a measured brem fraction  $f_{brem} < 0.5$ ;
- “big brem,” or electrons with a high bremsstrahlung fraction but no evidence of energy loss effects:
  - a supercluster formed by a single cluster,
  - a ratio  $E/p > 0.9$ ,
  - a measured bremsstrahlung fraction  $f_{brem} > 0.5$ ;
- “showering,” or electrons with an energy pattern highly affected by bremsstrahlung losses:

- a supercluster formed by a single cluster not falling in the “golden” or “big brem” classes, or a supercluster formed by several sub-clusters.
- In addition, “crack” electrons are defined as electrons whose supercluster’s starting crystal is close to a boundary between the ECAL barrel modules, or close to the boundary between the ECAL barrel and ECAL endcaps.

The electron momentum magnitude is defined as the weighted mean of  $E$  and  $p$  when  $|E/p - 1| < 2.5 \sigma_{E/p}$  (weights are the normalized inverse of the variance of each measurement). If the above inequality is not satisfied, the ECAL measurement is taken as the electron momentum magnitude, except for the following cases in the ECAL barrel:

- the electron is golden,  $E < 15$  GeV and  $E/p < 1.15$
- the electron is showering,  $E < 18$  GeV and  $E/p < 1 - 2.5 \sigma_{E/p}$
- the electron is in the crack class,  $E < 60$  GeV and  $E/p < 1 - 2.5 \sigma_{E/p}$

or in the ECAL endcaps:

- the electron is golden and  $E < 13$  GeV and  $E/p < 1.15$

for which the tracker measurement is taken.

The comparison of the tracker-only, ECAL-only, and combined electron momentum estimation for electrons in the ECAL barrel is illustrated in Figure 5.3, where the normalized momentum effective RMS are presented [39]. The tracker measurement is more accurate at low energies, while at high energies ECAL measurement provides best precision. A clear improvement in the momentum determination precision is observed for the combined estimate with respect to the ECAL-only measurement, for energies below  $\sim 25 - 30$  GeV.

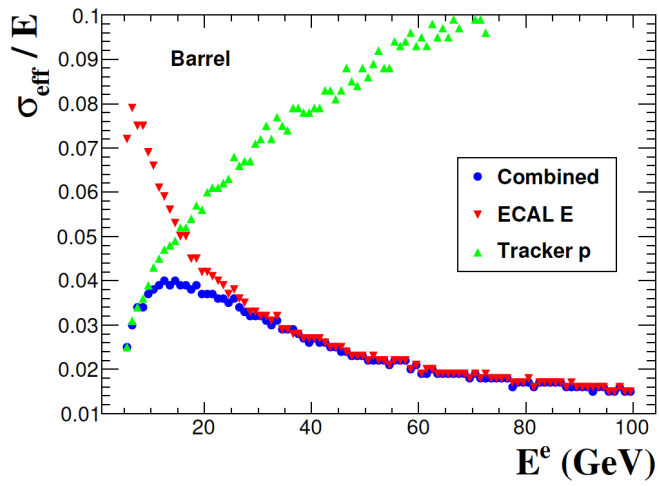


Figure 5.3: Performance of the combined momentum estimate, showing the effective momentum resolution for the ECAL (in red), for the tracker (in green) and the combined momentum estimate (in blue), as a function of the generated electron energy, for electrons in the ECAL barrel. The electrons are from a sample of simulated dielectron events with a uniformly distributed transverse momentum between 2 and 150 GeV [39].



# Chapter 6

## Electron Identification

Electron objects are reconstructed in CMS as a combination of a track in the silicon tracker and a supercluster (cluster of clusters) in the ECAL, as summarized in Chapter 5. Electron reconstruction is designed to incorporate a characteristic signature that electrons leave in the CMS detector. However similar signatures can sometimes be produced by charged hadrons, hadron jets, or photon conversions, as well as secondary electrons. In order to distinguish “real” electrons from such possible contributions a further selection has to be applied to the quantities that carry discriminating power against objects that can mimic electrons.

The initial stage of electron identification (ID) is performed at the reconstruction step by means of a preselection which is designed to be loose enough to satisfy “all possible” analysis requirements (including all channels with electrons in the final state that are analyzed by CMS). Then a specific identification is applied during each analysis to define a “working point” that trades off the selection efficiency for real electrons versus the level of “fake” electron contamination [90]. Typical working points that are often used in CMS have efficiencies in the range of 80% to 95%, with corresponding fake rates of 0.5% to 2% [80].

These identification requirements are different for electron candidates in different regions of the electron energy spectrum. One can identify three distinct categories:

- Low energy electrons, with transverse energy below  $\sim 20$  GeV. This category is characterized by electrons that can lose a significant fraction of their energy to bremsstrahlung as they pass through the material of the tracker. The bremsstrahlung photons, some of which subsequently convert in the tracker, spread out in a large window in the  $\phi$  direction as they travel through the CMS’

3.8 Tesla solenoidal magnetic field. The GSF track reconstruction algorithm [84] provides an accurate trajectory reconstruction and momentum determination, however the cluster-pattern of the energy seen in the ECAL can be substantially affected, making supercluster reconstruction and energy determination more difficult and less accurate.

- Medium energy electrons, where the transverse energy of the electrons is between  $\sim 20$  GeV and  $\sim 100$  GeV. This category, which is mostly populated by electrons that come from Z and W decays, is characterized by electrons that are well-reconstructed, have most of their energy well-clustered in the ECAL, and have a good track quality.
- High energy electrons, with electrons above  $\sim 100$  GeV. In this case most of the bremsstrahlung energy emitted by the electron is typically well-collimated in a narrow cone around the electron trajectory, and the ECAL supercluster can be very well-reconstructed.

In this chapter I describe the variables and criteria used to identify electrons in the medium and high energy electron categories.

## 6.1 Selection variables

The main background to the signal electron events at the LHC comes from QCD events. Signal electrons, for example from Z decays, typically will have an electron that is well isolated and has a very small deposition in the HCAL detector, whereas a typical QCD event will have activity in a wider cone with a significant fraction of the energy deposited in the HCAL.

There are a number of variables that are sensitive to these differences and thus carry discrimination power. These can be split into three categories as follows:

- Isolation variables
- Identification variables

- Photon conversion rejection variables

In the following I will describe in more detail each individual variable from the categories mentioned above.

### 6.1.1 Isolation variables

Isolation variables are defined as a sum of transverse energy or momentum measured by one of the detector systems in a cone in the  $\eta-\phi$  plane. The contribution associated with the electron candidate is removed from the sum. The following isolation variables are used in electron identification:

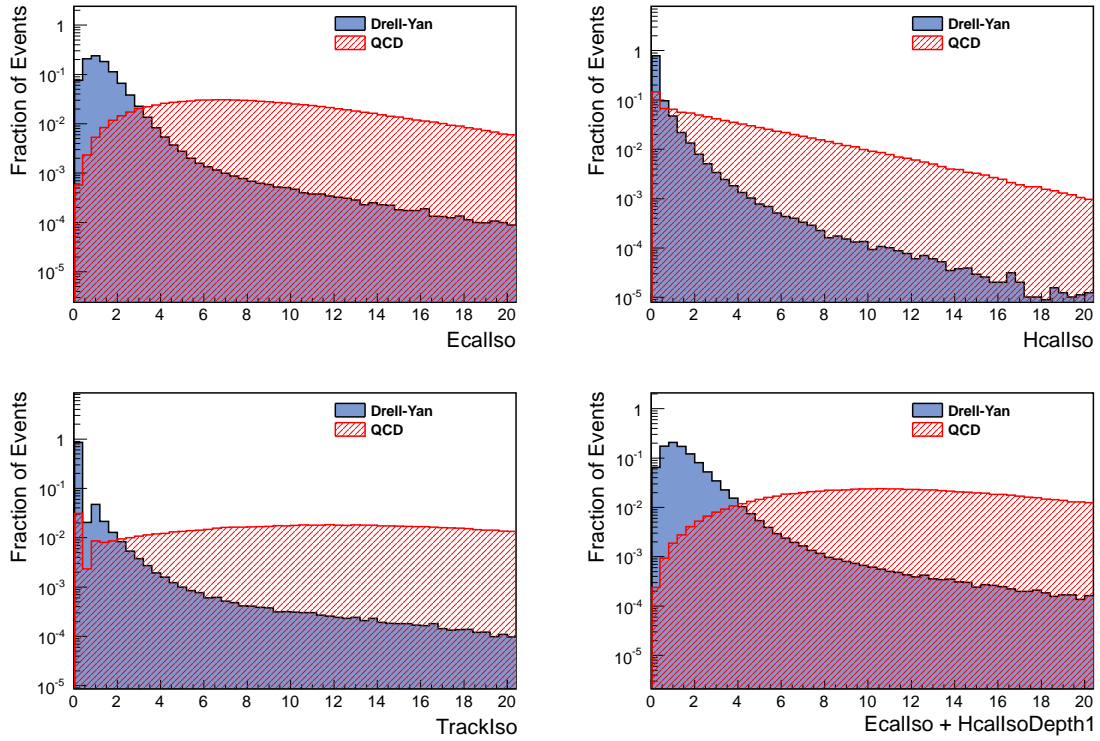


Figure 6.1: Distributions of the isolation variables for characteristic signal electrons originating from the simulated Drell-Yan process, and for background electrons reconstructed in a sample of simulated QCD events. The distributions are for the barrel region.

- *TrackIso* - track isolation, defined as the  $\sum p_T$  of all tracks within a cone of  $\Delta R \in (0.015, 0.3)$  about the electron track satisfying  $p_T > 0.7$  GeV, with a distance of closest approach from the primary vertex in the event  $< 0.2$  cm. A strip in the  $\phi$  direction centered at the electron track position, with a width of  $|\Delta\eta| < 0.015$ , is excluded from the sum.
- *EcalIso* - ECAL isolation, defined as the  $\sum E_T$  of all ECAL crystals within a cone of  $\Delta R < 0.3$  centered on the electron supercluster position satisfying  $E > 0.08$  ( $E_T > 0.1$ ) GeV in the ECAL barrel (endcap). Crystals within an inner cone of radius equal to the size of three crystals, and a strip in the  $\phi$  direction centered at the electron supercluster position with a half width of 1.5 crystals, are excluded from the sum. This is to remove the footprint of the original electron candidate when calculating the energy surrounding it in the ECAL.
- *HcalIso* - HCAL isolation, defined as the  $\sum E_T$  of all HCAL towers within a cone of  $\Delta R \in (0.15, 0.3)$  centered on the electron supercluster position.
- *HcalIsoDepth1* - HCAL isolation at depth 1, defined as the transverse hadronic energy of all the HCAL towers at depth 1 in a cone of  $\Delta R \in (0.15, 0.3)$  centered on the electron supercluster position. Depth 1 is defined as all segments in towers 1-17, segment 1 in towers 18-29, and segment 2 in towers 27-29 (tower segmentation is discussed in Section 3.2.4 and is illustrated in Figure 3.17).
- *HcalIsoDepth2* - HCAL isolation at depth 2, defined as the transverse hadronic energy of all the HCAL towers at depth 2 in a cone of  $\Delta R \in (0.15, 0.3)$  centered on the electron supercluster position. Depth 2 is defined as segment 2 in towers 18-26, and segment 3 in towers 27-29, and is defined only for the endcap region.

Figure 6.1 and Figure 6.2 show the distributions of the isolation variables introduced above, for the barrel and endcap regions respectively.

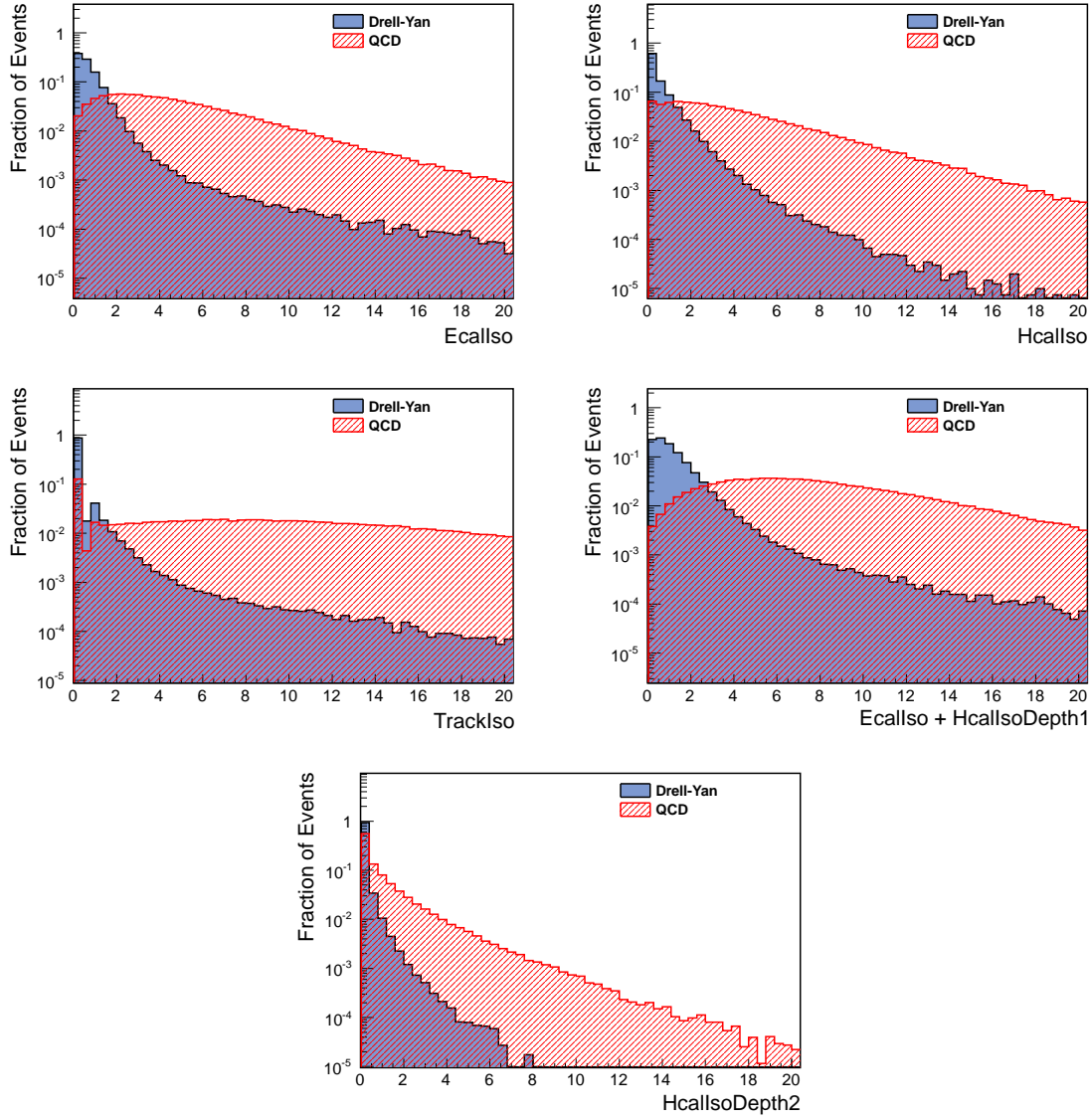


Figure 6.2: Distributions of the isolation variables for characteristic signal electrons originating from the simulated Drell-Yan process, and for background electrons reconstructed in a sample of simulated QCD events. The distributions are for the endcap region.

### 6.1.2 Identification variables

The identification variables detailed in this section are used to characterize the shower profile created by an electron candidate in the calorimeters, both longitudinal and transverse with respect to the electron direction, and provide the basis for evaluating the compatibility between a track and a supercluster.

Electrons are characterized by narrow showers in the  $\eta$  direction, while due to bremsstrahlung and the solenoidal magnetic field the shower can be spread out in the  $\phi$  direction. In contrast, QCD jets have a wide shower in both the  $\eta$  and  $\phi$  directions, so that the shower spread in the  $\eta$  direction can provide discriminating power between electrons and QCD jets. These properties are exploited through the use of the energy-weighted width of the supercluster in the  $\eta$  direction, denoted  $\sigma_{i\eta i\eta}$ , and  $E^{1\times 5}/E^{5\times 5}$  and  $E^{2\times 5}/E^{5\times 5}$ , which also provide information on the spread of the shower in the  $\eta$  direction.

Since the crystals in the ECAL are  $25.8 X_0$  in the barrel and  $24.7 X_0$  in the endcaps [48], electrons typically deposit more than 99 % of their remaining energy in the ECAL (depending on the pseudorapidity electrons travel through 0.4 - 1.8  $X_0$  of tracker material before they reach ECAL), leaving almost no trace in the HCAL. Hadrons, on the other hand, deposit a sizable fraction of their energy in the HCAL (the ECAL crystals have  $\sim 1 \lambda_I$  [48]). Thus the ratio of energy deposited in the HCAL behind the ECAL supercluster to the energy of the ECAL supercluster, provides additional discriminating power.

The spatial compatibility of the ECAL supercluster with the associated track is quantified by  $\Delta\eta_{in}$ ,  $\Delta\phi_{in}$ , also discussed in Section 5.4.1, while the energy - momentum compatibility between the track and supercluster is quantified by  $E_{seed}/p_{in}$ .

The precise definitions of the variables mentioned above are provided below:

- $H/E$  - where  $H$  is the energy deposited in the HCAL towers in a cone of radius  $\Delta R = 0.15$  centered on the electromagnetic supercluster position, and  $E$  is the energy of the electromagnetic supercluster.
- $\Delta\eta_{in} = \eta_{sc} - \eta_{in}^{extrap}$ , where  $\eta_{sc}$  is the energy weighted centroid position in  $\eta$  of

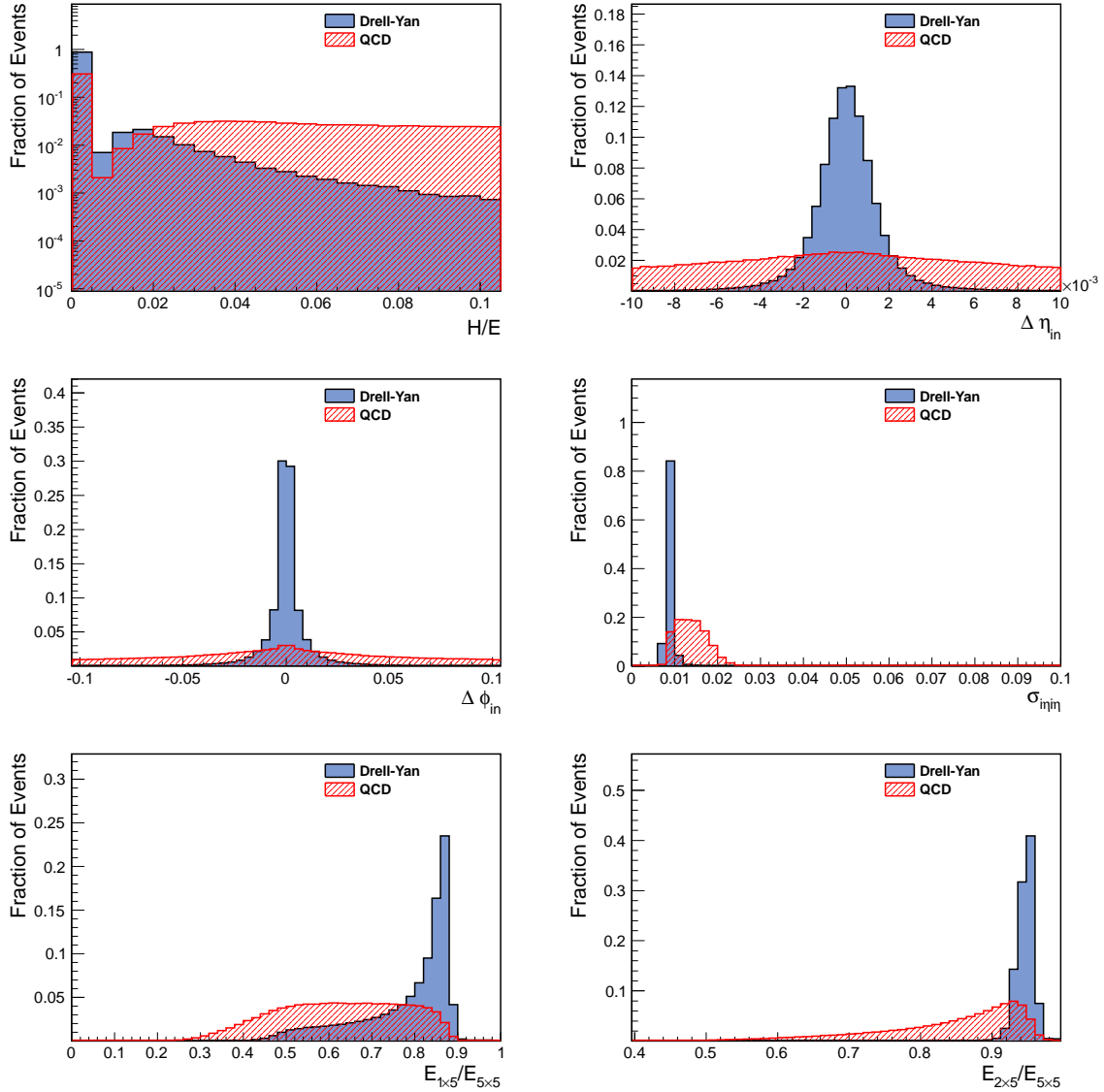


Figure 6.3: Distributions of the identification variables for characteristic signal electrons originating from the simulated Drell-Yan process, and for background electrons reconstructed in a sample of simulated QCD events. The distributions are for the barrel region.

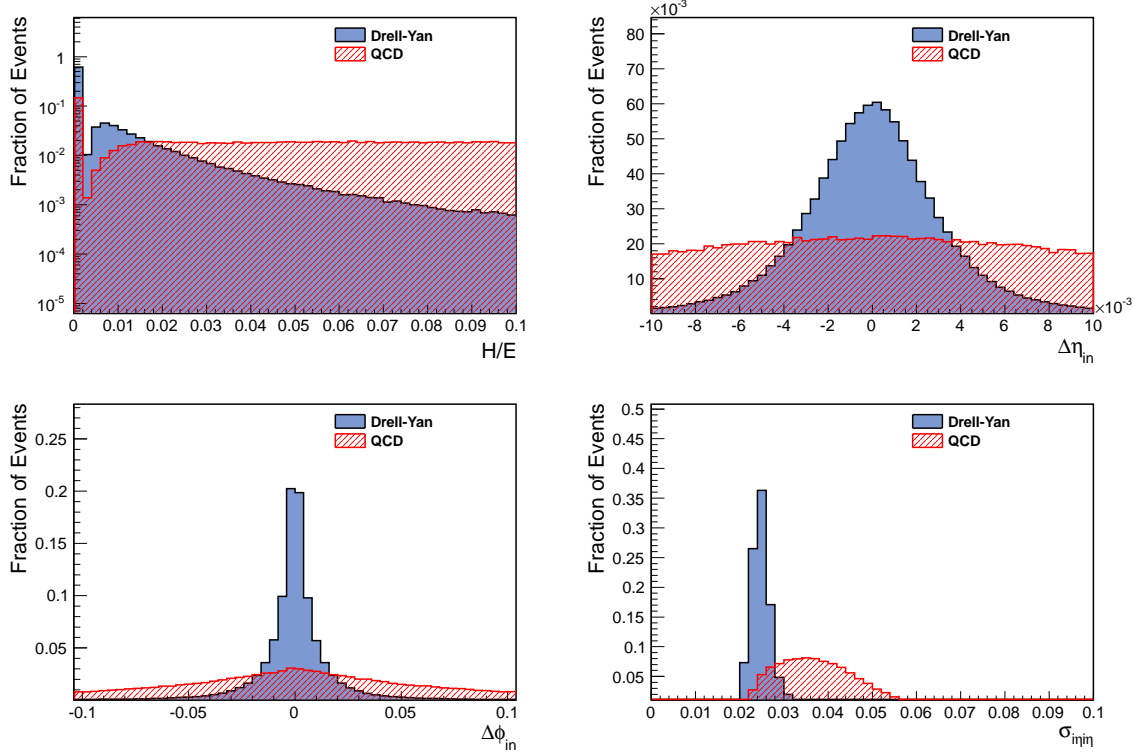


Figure 6.4: Distributions of the identification variables for characteristic signal electrons originating from the simulated Drell-Yan process, and for background electrons reconstructed in a sample of simulated QCD events. The distributions are for the endcap region.

the supercluster, and  $\eta_{in}^{extrap}$  is the associated track pseudorapidity at the ECAL surface as extrapolated from the innermost tracker layer.

- $\Delta\phi_{in} = \phi_{sc} - \phi_{in}^{extrap}$ , where  $\phi_{sc}$  is the energy weighted centroid position in  $\phi$  of the supercluster, and  $\phi_{in}^{extrap}$  is the associated track  $\phi$  coordinate at the ECAL surface as extrapolated from the innermost tracker layer.
- $\sigma_{i\eta i\eta}^1 = \sqrt{\sum_i^{5\times 5} \omega_i (\eta_i - \bar{\eta}_{5\times 5})^2 / \sum_i^{5\times 5} \omega_i}$ , where the index  $i$  runs over all the crystals in a  $5 \times 5$  block of crystals centered on the seed crystal,  $\eta_i$  is the  $\eta$  position of the  $i^{th}$  crystal,  $\bar{\eta}_{5\times 5}$  is the energy weighted mean  $\eta$  of the  $5 \times 5$  block of crystals and  $\omega_i$  is the weight of the  $i^{th}$  crystal and is defined as  $\omega_i = 4.7 + \ln(E_i/E_{5\times 5})$ , where  $E_i$  and  $E_{5\times 5}$  are the energy of the  $i^{th}$  and  $5 \times 5$  block of crystals respectively.
- $E^{1\times 5}/E^{5\times 5}$  - is defined as the ratio of the energy of a strip measuring one crystal in  $\eta$  and 5 crystals in  $\phi$ , centered on the seed crystal, to the energy in a  $5 \times 5$  crystal matrix centered on the seed crystal.
- $E^{2\times 5}/E^{5\times 5}$  - is defined as the ratio of the energy of a strip measuring two crystals in  $\eta$  and 5 crystals in  $\phi$ , centered on the seed crystal, to the energy in a  $5 \times 5$  crystal matrix centered on the seed crystal. The  $2 \times 5$  block is chosen such that it has the highest energy out of the two possible combinations.

Figure 6.3 and Figure 6.4 show the distributions of the identification variables introduced above, for the barrel and endcap regions respectively.

### 6.1.3 Photon conversion rejection

Due to the significant material budget of the CMS tracking system, large multiple scattering, bremsstrahlung and high photon conversion rates are common. Electrons

---

<sup>1</sup>In the calculation of  $\sigma_{i\eta i\eta}$  the  $\eta$  position of each crystal in the barrel is defined as the distance expressed in terms of the number of crystals from the seed crystal. In the endcap “ $i\eta$ ” is no longer related to pseudorapidity alone, but is calculated as  $\sqrt{iX^2 + iY^2}$ , where  $iX$  and  $iY$  are the coordinates of the crystal in units of the number of crystals from the center of the endcap. Then an overall normalization to the average size of the crystals 0.01745 (0.0447) in the barrel (endcap) is applied.

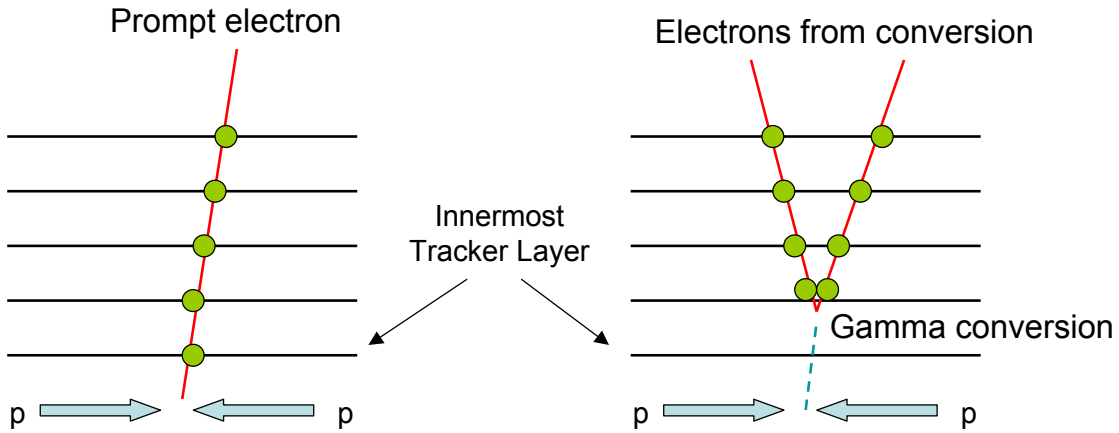


Figure 6.5: Prompt electrons originating from the primary  $pp$  collision vertex (left) usually have “hits” on the innermost Tracker layer. Conversely, electrons from converted photons often do not have hits on the first layer due to photons converting at larger radii.

from photon conversions represent a non-negligible background to prompt electrons, i.e. electrons coming from the interaction vertex. To reduce the contamination coming from converted photons, several selection criteria based on variables that exploit the characteristic topology of converted photons have been used [91]. These variables are defined as follows:

- *MissingHits* - the number of missing hits in the innermost tracker layers for the electron track [92]. As the first photon conversions usually occur inside the tracker volume, and not at the primary vertex, the first valid hit of a resulting electron track may not necessarily be located in the innermost tracker layer. Extrapolating the track of an electron from a photon conversion back to the beam-line, one could cross one or more active detector layers which do not have hits compatible with the track, i.e. a missing hit. For prompt electrons, whose trajectories start from the beam-line, we do not expect any missing hits in the crossed inner tracker layers, as shown in Figure 6.5. We therefore use this expectation of no missing hits at the inner radii to reject electrons from photon conversions.

- $\Delta \cot\theta = \cot(\theta_{\text{partner track}}) - \cot(\theta_{\text{electron track}})$ , where  $\theta_{\text{electron track}}$  is the  $\theta$  direction of the electron track and  $\theta_{\text{partner track}}$  is the direction of its nearest partner track. A partner track is chosen from all the tracks in a cone  $\Delta R < 0.3$  around the electron track and with the charge opposite to the electron charge<sup>2</sup>. Electron tracks from a photon conversion will be nearly parallel to each other at the conversion point, and will remain nearly parallel in the  $r - z$  plane, thus  $\Delta \cot\theta$  can help distinguish a prompt electron from an electron produced in photon conversion.
- *Dist* - is the distance in the  $r - \phi$  plane between the electron track and its nearest partner track (defined above), which is defined as the distance between the track trajectory points where the electron and the partner track directions are parallel to each other. Electrons from photon conversion will have small *Dist* values, thus allowing one to further identify electrons from photon conversions.

## 6.2 Electron selection at intermediate energies

At intermediate electron energies, the selection criteria are optimized to be efficient for electrons from Z and W decays. Two main electron identifications have been used, one with an efficiency of 95 % for electrons from Z decays, and the other with an efficiency of 80 % for W decays, as summarized in the Table 6.1 and Table 6.2 [93].

## 6.3 Electron selection at high energies

At high energies, an electron trajectory in the tracker is close to a straight line, and the majority of the emitted radiation through the bremsstrahlung is well contained within the ECAL supercluster. These electrons are well isolated and have a good matching

---

<sup>2</sup>Partner tracks are chosen from a list of general Kalman Filter (KF) [86] tracks. Tracks that share a significant fraction of their tracker hits with the electron track (which are produced using the Gaussian Sum Filter (GSF) [84, 85] reconstruction algorithm) are excluded from the possible partner track list, as they, to a large extent, represent a Kalman Filter track which is fitted to the same electron track. See Section 5.3 for a discussion of CMS' track reconstruction algorithms.

Variables	Selection in barrel	Selection in endcap
$\Delta\eta_{in}$	< 0.007	< 0.01
$\Delta\phi_{in}$	< 0.8	< 0.7
$H/E$	< 0.15	< 0.07
$\sigma_{in\eta in}$	< 0.01	< 0.03
$TrackIso/p_T$	< 0.15	< 0.08
$EcalIso/p_T$	< 2	< 0.06
$HcalIso/p_T$	< 0.12	< 0.05
$MissingHits$	< 2	< 2

Table 6.1: Electron identification criteria for intermediate energy electrons at 95 % efficiency.

between the track and the ECAL supercluster. The selection criteria used to identify high energy electrons are summarized in Table 6.3. This selection is the main one used to search for high mass dielectron resonances [94], discussed in Chapter 8, and is sometimes referred to as the “HEEP”<sup>3</sup> selection.

---

<sup>3</sup>This identification has emerged from the “High Energy Electron Pairs” Group (HEEP Group), thus the name HEEP selection (or HEEP ID).

<sup>4</sup>The  $E_T$  cut for the endcap electrons is relaxed to 35 GeV when this selection is used to study the electron energy scale and the dielectron mass resolution, as discussed in Section 7.2.

<sup>5</sup>This refers to the electron reconstruction seeding algorithms discussed in Section 5.1. As high energy electrons have a well reconstructed supercluster in the ECAL, ECAL seeding is preferred over track-based seeding.

Variables	Selection in barrel	Selection in endcap
$\Delta\eta_{in}$	< 0.004	< 0.007
$\Delta\phi_{in}$	< 0.06	< 0.03
$H/E$	< 0.04	< 0.025
$\sigma_{i\eta i\eta}$	< 0.01	< 0.03
$TrackIso/p_T$	< 0.09	< 0.04
$EcalIso/p_T$	< 0.07	< 0.05
$HcalIso/p_T$	< 0.10	< 0.025
$MissingHits$	< 1	< 1
$Dist$ or $\Delta cot\theta$	> 0.02	> 0.02
	> 0.02	> 0.02

Table 6.2: Electron identification criteria for intermediate energy electrons at 80 % efficiency.

Variables	Selection in barrel	Selection in endcap
$E_T$	> 35GeV	> 40GeV <sup>4</sup>
$ \eta_{SC} $	< 1.442	$1.56 <  \eta_{SC}  < 2.5$
seed	ECAL seed	ECAL seed <sup>5</sup>
$\Delta\eta_{in}$	< 0.005	< 0.007
$\Delta\phi_{in}$	< 0.06	< 0.06
$H/E$	< 0.05	< 0.05
$\sigma_{i\eta i\eta}$	-	< 0.03
$E^{2\times 5}/E^{5\times 5}$	> 0.94	-
or		
$E^{1\times 5}/E^{5\times 5}$	> 0.83	-
$TrackIso$	< 5GeV	< 5GeV
$EcalIso + HcalIsoDepth1$	$< 2 + 0.03 \times E_T$ GeV	$< 2.5$ GeV, for $E_T < 50$ GeV $< 2.5 + 0.03 \times (E_T - 50)$ GeV, for $E_T \geq 50$ GeV
$MissingHits$	< 1	< 1

Table 6.3: Electron identification criteria at high energies.



# Chapter 7

## ECAL Energy Scale and Dielectron Mass Resolution

The energy measured by the electromagnetic calorimeter represents the sum of the energies measured by each of the individual crystals that have been clustered, and then corrected based on the properties of the cluster (see Section 5.2). The contribution of each individual crystal is uniformized by the inter-calibration procedure [88], which ensures that the response of each crystal is the same for identical energy depositions. However, the inter-calibration constants and cluster corrections provide only the relative corrections. The absolute value of the energy is fixed by the ECAL energy scale  $G$ , which converts the measured amplitude for each individual channel measured in ADC counts<sup>1</sup> to GeV. The ECAL energy scale has been measured in test beams prior to data taking, and then corrected in-situ by the  $\pi^0$  and  $\eta$  measurements [88]. However this scale must be carefully monitored in order to guarantee that the energy measurements are correct.

In this Chapter I will discuss the methods used to validate the ECAL energy scale, and to estimate the dielectron mass resolution.

### 7.1 ECAL energy scale

The cluster energy measured by the electromagnetic calorimeter is expressed as (see Section 5.2):

---

<sup>1</sup>An analog-to-digital converter (abbreviated ADC) is a device that converts a continuous readout signal to a digital number that represents the signal's amplitude. In the case of the ECAL detector, the ADC counts represent the amplitude of the signal read out by the photo-detectors mounted on the surface of the ECAL crystals (see Section 3.2.3).

$$E = F \sum_{cluster} G \times S_i(t) \times c_i \times A_i \quad (7.1)$$

where the sum is over the crystals belonging to the electromagnetic cluster,  $A_i$  is the reconstructed pulse amplitude in ADC counts,  $c_i$  is the inter-calibration constant, and  $G$  is a global ECAL energy scale (measured in GeV/ADC). The term  $S_i(t)$  is the laser monitoring correction to the crystal amplitude, due to the radiation-induced transparency change at the event time  $t$ , as described in Section 4.3. And  $F$  is the supercluster energy correction function described in Section 5.2.

The energy scale  $G$  of the ECAL has been measured for the barrel (EB) and the endcap (EE) regions separately in a series of beam tests prior to LHC operation. In these tests the energy scale was derived by requiring that the energy sum of a  $5 \times 5$  crystal matrix centered around the crystal in the beam matches the electron beam energy. This value then was corrected to take into account the effect of the magnetic field on electromagnetic shower containment and photo-detector gain, as well as the small temperature differences between the test beam and LHC environment.

Thus the ECAL energy scale is defined as the value of  $G$  such that a  $5 \times 5$  crystal cluster will give the correct energy for an unconverted photon of 50 GeV in the ECAL barrel and endcap reference regions, defined as:

- in EB: the central crystals in Module 1, in the low  $\eta$  region of each barrel super-module with the coordinates  $6 \leq |i\eta| \leq 20$  and  $6 \leq (i\phi \bmod 20) \leq 15$ <sup>1</sup> (Figure 7.1)
- in EE: the central part of each EE side (covered by ES), excluding the crystals near the separation between the two halves of each EE side ( $1.7 \leq |\eta| \leq 2.3$  and  $|\phi - \frac{\pi}{2}| > 0.1$  and  $|\phi + \frac{\pi}{2}| > 0.1$ )

---

<sup>1</sup>The notations  $i\eta$  and  $i\phi$  represent (by convention) the coordinates in the  $\eta$  and  $\phi$  directions, expressed in terms of the number of crystals correspondingly. In the expression  $(i\phi \bmod 20) \bmod$  is the standard modulo operator, and 20 crystals correspond to the size of a super-module, i.e. the equation holds for each super-module.

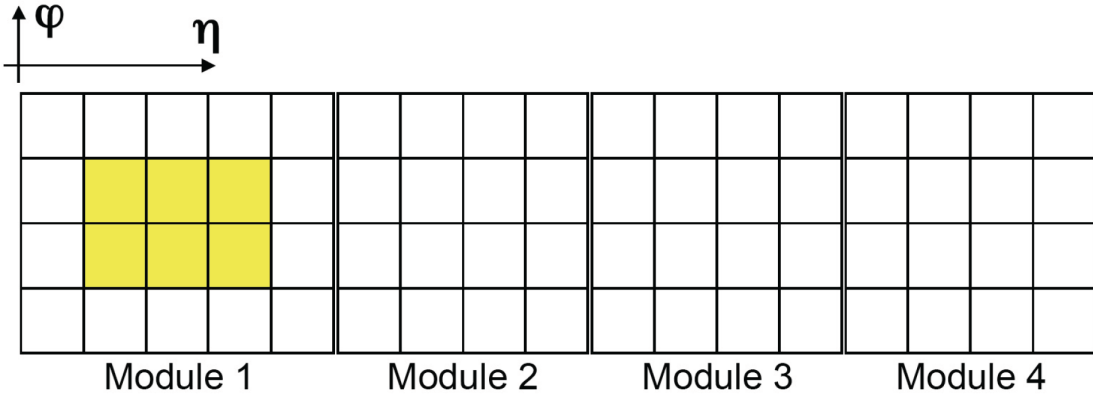


Figure 7.1: Definition of the reference region for energy scale determination in the ECAL barrel region.

In-situ, the ECAL energy scale can be tuned by reconstructing the diphoton and dielectron invariant mass peaks of known particles using unconverted photons and electrons that lose relatively little energy due to bremsstrahlung radiation [88].

The energy scale was set by the measurements done in test beams, and then corrected by measurements using  $\pi^0 \rightarrow \gamma\gamma$  in the early LHC data-taking period. The first validation of the ECAL energy scale with dielectron resonances was done using  $J/\psi \rightarrow e^+e^-$  decays [95], providing the first energy scale validation at low energies (in the 2 - 5 GeV range).  $J/\psi \rightarrow e^+e^-$  events were also used as the first tool to validate electron reconstruction and identification, in particular in the early running period when the LHC luminosity was low and the trigger criteria were significantly relaxed. As the luminosity increased, and the trigger criteria were tightened, the rate at which  $J/\psi$  candidates were reconstructed dropped below the rate of  $Z$  production. At this stage, the  $Z \rightarrow e^+e^-$  decay became the main validation signal for electromagnetic objects, as well as for gauging the ECAL performance.

The energy reconstructed in the ECAL can be affected by the CMS and the LHC operating conditions. In particular, the transparency of the ECAL crystals changes under the influence of the radiation produced in proton-proton collisions as discussed in Section 4.1. As the instantaneous luminosity increased, this effect became more pronounced. The laser corrections applied promptly (see Section 4.1) sometimes

contained small systematic effects that had to be understood and corrected using an extended event data set. To account for that  $Z \rightarrow e^+e^-$  events were used to monitor the ECAL energy scale throughout the data-taking period.

The dielectron invariant mass, assuming  $m_e \ll E_e$ , can be calculated as:

$$M_{inv} = \sqrt{2E_1E_2(1 - \cos(\Theta))} \quad (7.2)$$

or

$$M_{inv} = \sqrt{4E_1E_2 \sin^2\left(\frac{\Theta}{2}\right)}, \quad (7.3)$$

where  $E_1$  and  $E_2$  are the energies of the outgoing electrons, and  $\Theta$  is the angle between them.

The change in the energy scale of individual electrons can be translated to the change in the invariant mass. As can be seen from Equation 7.1, the energy scale can be factored out and should be equal for both electrons, thus:

$$\begin{aligned} M_{inv} &= \sqrt{4E_1E_2 \sin^2\left(\frac{\Theta}{2}\right)} = \sqrt{4 G \cdot E_1^0 G \cdot E_2^0 \sin^2\left(\frac{\Theta}{2}\right)} \\ &= G \sqrt{4E_1^0E_2^0 \sin^2\left(\frac{\Theta}{2}\right)}, \end{aligned} \quad (7.4)$$

where  $E_1^0$  and  $E_2^0$  are the energies of the electrons without energy scale factor applied.

Therefore, if the energy scale is offset by a factor  $\alpha_{ES}$ , then it would result in a shift of the invariant mass peak position as observed in the data with respect to the predictions from the simulation:

$$M_{inv}^{Data} = \alpha_{ES} \cdot M_{inv}^{MC}. \quad (7.5)$$

Assuming that the performance of the reconstruction algorithms and the associated corrections is similar in the data and the MC, then by measuring the Z peak position both in the data and in the MC we can validate the energy scale and the

performance of the energy correction algorithms.

Furthermore, by investigating the width of the  $e^+e^-$  peak, we can compare the energy resolution performance in the data with the one predicted by MC. From Equation 7.3 the  $e^+e^-$  resolution can be factorized as follows:

$$\frac{\sigma_{M_{inv}}}{M_{inv}} = \frac{1}{2} \cdot \frac{\sigma_{E_1}}{E_1} \oplus \frac{\sigma_{E_2}}{E_2} \oplus \frac{\sigma_\Theta}{\tan \frac{\Theta}{2}}, \quad (7.6)$$

or, neglecting the effect of the angular resolution on the invariant mass resolution<sup>1</sup>:

$$\frac{\sigma_{M_{inv}}}{M_{inv}} = \frac{1}{\sqrt{2}} \frac{\sigma_E}{E}. \quad (7.7)$$

In the following sections I will describe the method used to infer the level of agreement of the energy scale between the Data and MC, as well as the dielectron mass resolution agreement, from the  $Z \rightarrow e^+e^-$  events. A similar procedure was implemented and used for the energy scale validation with  $J/\psi \rightarrow e^+e^-$  decays [95].

## 7.2 Energy scale and dielectron mass resolution with $Z \rightarrow e^+e^-$

$Z$  bosons are mainly produced in the Drell-Yan process, which can be easily identified in the dielectron decay channel. By analyzing the dielectron invariant mass spectrum, both in the data and in the MC, we can estimate the ECAL detector performance and derive the necessary correction factors for the physics analysis performed on this data [97].

---

<sup>1</sup>The angular resolution is at the mrad level, which can be neglected in this calculation given the range of opening angles characteristic of  $Z \rightarrow e^+e^-$  decays.

### 7.2.1 Energy scale and dielectron mass resolution estimation method

To estimate the dielectron mass resolution and the electron energy scale, we perform a fit to the dielectron invariant mass spectrum of a functional form which represents the convolution of the Crystal Ball (CB) (Equation 7.8) and the Breit Wigner (BW) (Equation 7.9) functions. In this approximation, the Breit Wigner shape is used to describe the underlying physical process, in this case  $Z \rightarrow e^+e^-$  decays. The BW peak position and width are fixed to the  $Z$  mass and width, according to the PDG average [8]. The Crystal Ball part of the fit, with all parameters allowed to float, represents the detector effects, such as a finite resolution and possible energy losses. In particular,  $\sigma_{CB}$  can be used as a measure of the dielectron mass resolution and  $\Delta m$  as the energy scale offset.

Functional forms of both the Crystal Ball and Breit Wigner shapes, as implemented in RooFit [96], are presented below:

$$f_{CB}(m; \alpha, n, \Delta m, \sigma_{CB}) = N \cdot \begin{cases} \exp\left(-\frac{(m-\Delta m)^2}{2\sigma_{CB}^2}\right) & , (m - \Delta m)/\sigma_{CB} > -\alpha \\ A \times (B - \frac{m-\Delta m}{\sigma_{CB}})^{-n} & , (m - \Delta m)/\sigma_{CB} \leq -\alpha \end{cases}$$

where  $A = (\frac{n}{|\alpha|})^n \times \exp(-|\alpha|^2/2)$ ,  $B = \frac{n}{|\alpha|} - |\alpha|$ ,

(7.8)

where  $\Delta m$  is the shift of the peak from nominal position,  $\sigma_{CB}$  is the width of the peak,  $\alpha$  is the cut off location where the Gaussian shape transitions to a power-law tail,  $n$  is the power of the low-end tail, and  $N$  is a normalization factor.

$$f_{BW}(m; m_0, \Gamma) = \frac{N}{(m - m_0)^2 + \Gamma^2/4},$$
(7.9)

where  $\Gamma$  is the width of the resonance,  $m_0$  is the resonance mass, and  $N$  is a normalization factor.

This choice of the signal parametrization proved to be convenient, and provides a reasonable accuracy for the parameter estimation, as will be shown in the following

sections.

By performing a fit to the convolution of the Breit Wigner and Crystal Ball functions, both in experimental data and in the Monte-Carlo simulation, we can get estimates of  $\sigma_{CB}$  and  $\Delta m$  for the data and the MC respectively. Then by comparing the  $\Delta m$  in the data and the MC we can monitor the energy reconstruction performance and estimate the energy scale uncertainty.

The difference in the Crystal Ball width between the data and the Monte Carlo simulation can be attributed to effects that are not included in the simulation, or are not modeled properly. This difference can be conservatively attributed to the constant term in the energy resolution parametrization (see Section 3.2.3). Thus the quantity

$$\sigma_{CB}(\text{extra}) = \sqrt{\sigma_{CB}^2(\text{Data}) - \sigma_{CB}^2(\text{MC})} \quad (7.10)$$

can be used to correct the estimation of the mass resolution derived from Monte Carlo. By adding in quadrature  $\sigma_{CB}(\text{extra})$  to the mass resolution derived from Monte Carlo, we recover the resolution observed in the data.

These techniques are used to estimate the mass resolution in the region above the  $Z$  peak when searching for new heavy dielectron resonances, as well as to estimate the energy scale uncertainty (see Section 8.4).

In the following section I will describe the results of the validation studies for several data-taking periods, as well as for several categories of events corresponding to different topologies of energy deposition in the ECAL.

## 7.2.2 Method performance in data

To investigate the performance of this method, events from dielectron  $Z$  decays are selected in the region of the  $Z$  mass peak.

**$Z \rightarrow e^+e^-$ selection**

The data sets used for this study are summarized in Table 7.1. They correspond to several reprocessings of the 2010 and a fraction of the 2011 data sets.

DATA
/EG/Run2010A-WZEG-Dec22Skim_v2/Raw-Reco
/Electron/Run2010B-WZEG-Dec22Skim_v2/Raw-Reco
/EG/CMSSW_4_2_0-GR_R_42_V8_RelVal_wzEG2010A-v1/RECO
/Electron/CMSSW_4_2_0-GR_R_42_V8_RelVal_wzEG2010B-v1/RECO
/DoubleElectron/Run2011A-May10ReReco-v1/RECO
/DoubleElectron/Run2011A-May3ReReco-v1/RECO
Monte Carlo
/DYToEE_M-20_TuneZ2_7TeV-pythia6/
Winter10-E7TeV_ProbDist_2010Data_BX156_START39_V8-v1/
GEN-SIM-RECO
/DYToEE_M-20_TuneZ2_7TeV-pythia6/Summer11-PU_S3_START42_V11-v2/
GEN-SIM-RECO

Table 7.1: Datasets used for the study of the ECAL energy scale validation method.

As a first step in the event selection, we consider only events that correspond to the periods declared as “good” by each sub-detector from the running conditions point of view. The list of such periods is summarized and certified by the Physics Validation Team (PVT).

Then we require that the event has at least one good reconstructed vertex, which is defined as a vertex with at least 4 associated tracks, located less than 2 cm from the center of the detector in the direction transverse to the beam, and within 24 cm in the direction along the beam.

To select  $Z \rightarrow e^+e^-$  candidates we require events to have two electrons that pass the electron identification criteria corresponding to 95 % signal efficiency (VBTF95) (see Section 6.2). To reconstruct the invariant mass of the  $Z$  candidates, the energy of the supercluster (SC) associated with the electron and the electron direction at the vertex are used. We use the energy of the supercluster instead of the associated electron energy, as the energy of the electron is in some cases a weighed average

of the energy measured by the ECAL (super cluster energy) and the momentum of the electron measured by the tracker (see Section 5.4). By choosing only the ECAL superclusters energy, we are making sure that any shift in the  $Z$  peak position is a result of ECAL-only effects. In general the ECAL energy determination is more precise for electron energies above  $\sim 15$  GeV, which constitutes the majority of the selected events in the  $Z$  peak region. For high energy electrons (above 100 GeV), the precision of the the energy measurement in the ECAL completely dominates the tracker momentum determination. The same invariant mass calculation is adopted in the analysis developed for the search for heavy dielectron resonances (see Chapter 8).

The selected  $Z$  candidates are split in two categories, one with candidates having both electrons in the ECAL barrel region, and another with both electrons in the ECAL endcap region.

The dielectron mass resolution can be affected by the reconstruction procedure and subsequent corrections, as well as inter-calibration and transparency corrections. To better estimate these effects, we split the electrons in categories according to their showering profiles and supercluster shapes.

The categorization of electrons according to their showering profile (“brem” categories) is done as follows:

- Showering:  $n_{brem} > 0$  and  $(p_{in} - E_{SC})/p_{in} \geq 0.1$
- Non-Showering:  $n_{brem} = 0$  or  $(p_{in} - E_{SC})/p_{in} < 0.1$

where  $n_{brem}$  is the number of brem clusters<sup>1</sup> associated with the electron supercluster,  $p_{in}$  is the momentum of the electron as measured at the vertex, and  $E_{SC}$  is the energy of the supercluster.

An additional categorization of electrons according to the SC shape (“r9” categories) is done as follows:

- Low  $r9$  (barrel) :  $r9 < 0.94$

---

<sup>1</sup>A brem cluster is a cluster that is a part of a super cluster but different from the seed cluster. Brem clusters are usually the result of a significant bremsstrahlung occurring in the tracker material, so that the electron changes slightly its direction and the energy deposited in the ECAL is no longer continuous (thus the name - “brem” cluster).

- High  $r9$  (barrel) :  $r9 \geq 0.94$
- Low  $r9$  (endcap) :  $r9 < 0.95$
- High  $r9$  (endcap) :  $r9 \geq 0.95$

where  $r9 = E_{5\times 5}/E_{SC_{raw}}$ ,  $E_{5\times 5}$  is the energy contained in a  $5\times 5$  matrix of ECAL crystals centered on the seed crystal of the supercluster,  $E_{SC_{raw}}$  is the raw energy of the supercluster associated with an electron candidate. This categorization is used to investigate the dielectron mass resolution in the categories adopted for the photon selection, which is also used for Higgs searches in the diphoton final state.

### $Z \rightarrow e^+e^-$ results for 2010 Data and MC.

The results for  $Z \rightarrow e^+e^-$  candidates with both electrons in the ECAL barrel region are presented in Figure 7.2. For illustration, the results without any categorization (left) and with both electrons identified as Non-Showering (right) are presented. The peak position in the data is adjusted to match that of the MC, in order to illustrate the agreement between the data and the MC in the shape and width of the distributions.

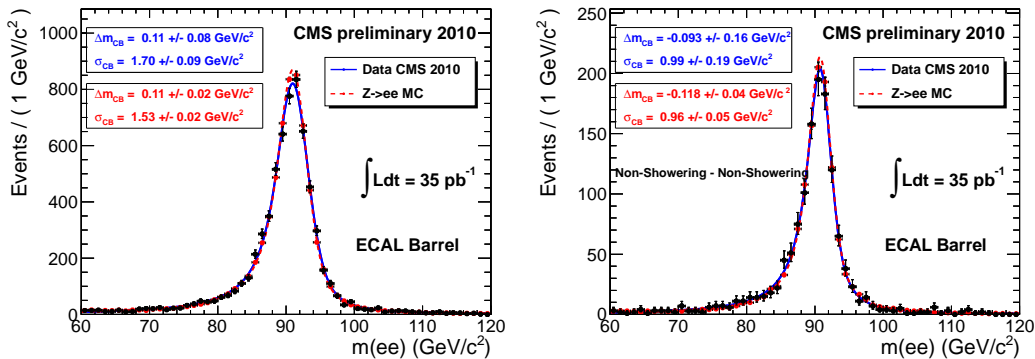


Figure 7.2:  $Z \rightarrow e^+e^-$  candidates with both electrons in the ECAL barrel together with the result of a CB $\otimes$ BW fit for the data and the MC, for all categories (left) and for both non-showering electrons (right).

This result was obtained from the data collected by the CMS detector during the 2010 data taking period. For the Non-Showering category, a good agreement

between the data and the Monte Carlo is observed; in particular the values of the  $\sigma_{CB}$  agree within their uncertainties between the data and MC. This agreement provides confidence in the performance of the energy reconstruction and the energy correction algorithms.

### Performance for electrons in $Z \rightarrow e^+e^-$ events in the 2011 data and MC (“brem” categories)

The results for  $Z \rightarrow e^+e^-$  candidates with both electrons in the ECAL barrel region are presented in Figure 7.3. Events are divided in two categories, one with both electrons identified as showering (left) and one with both non-showering electrons (right). The results of the fit procedure applied to  $Z$  candidates with both electrons in the ECAL endcap region, divided in the same categories are presented in Figure 7.4. A subset of the 2011 data was used to produce these results.

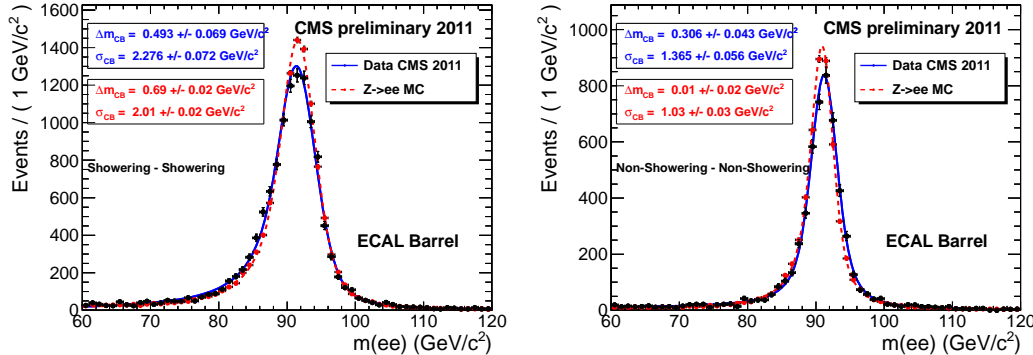


Figure 7.3:  $Z \rightarrow e^+e^-$  candidates with both electrons in the ECAL barrel together with the result of a CB $\otimes$ BW fit for the data and the MC, for both showering electrons (left) and for both non-showering electrons (right).

### Performance for electrons in $Z \rightarrow e^+e^-$ events in the 2011 data and MC (“r9” categories)

Figures 7.5, 7.6 show the results for  $Z \rightarrow e^+e^-$  candidates with both electrons in the ECAL barrel and the ECAL endcap, respectively. Events are divided in two

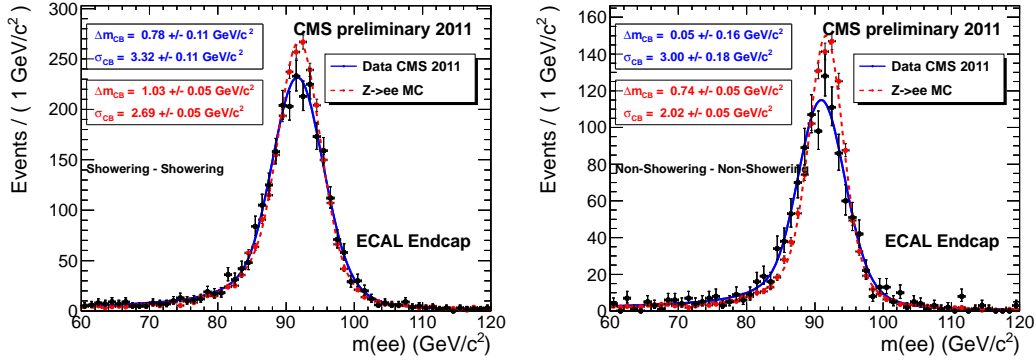


Figure 7.4:  $Z \rightarrow e^+e^-$  candidates with both electrons in the ECAL endcap together with the result of a CB $\otimes$ BW fit for the data and the MC, for both showering electrons (left) and for both non-showering electrons (right).

categories, one with both Low  $r9$  electrons and one with both High  $r9$  electrons. These categories, as defined above, are characteristic of  $\gamma$  candidates. Investigating these categories can provide input to the diphoton mass resolution studies. The same data set as in the previous section was used to produce these plots.

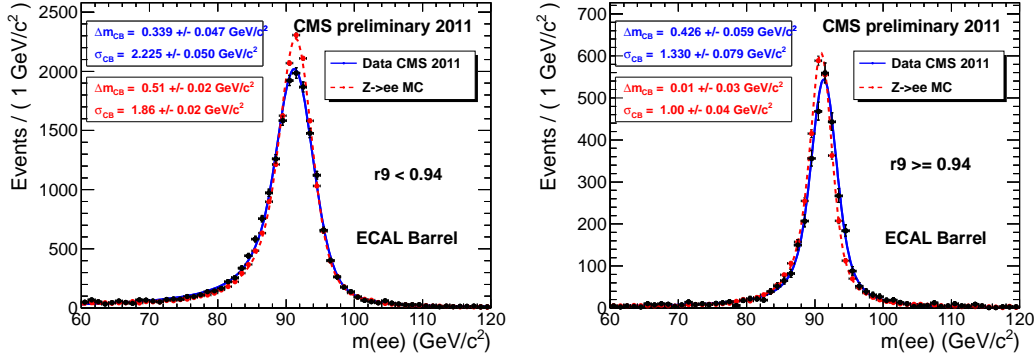


Figure 7.5:  $Z \rightarrow e^+e^-$  candidates with both electrons in the ECAL barrel together with the result of a CB $\otimes$ BW fit for the data and the MC, for both electrons with Low  $r9$  (left) and for both electrons with High  $r9$  (right).

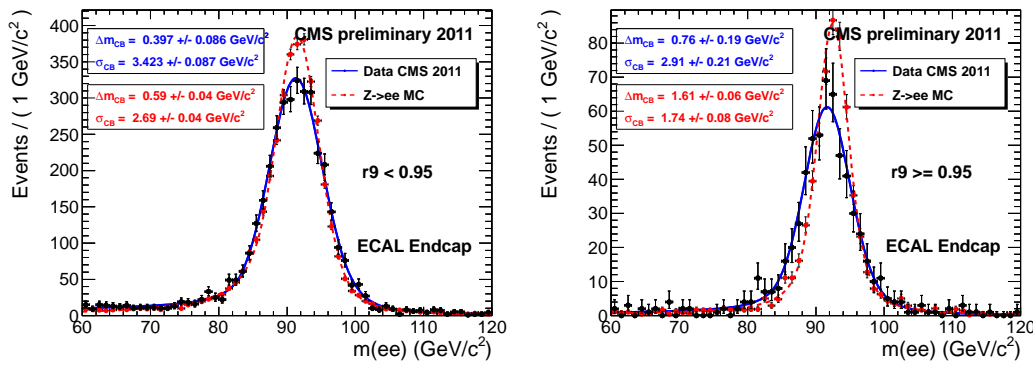


Figure 7.6:  $Z \rightarrow e^+e^-$  candidates with both electrons in the ECAL endcap together with the result of a CB $\otimes$ BW fit for the data and the MC, for both electrons with Low r9 (left) and for both electrons with High r9 (right).

### 7.2.3 Fixed Crystal Ball cut off parameter consideration

In the early periods of data-taking, when the number of Z candidates was not large enough, the values of the fit parameters showed large variations. The parameter which had a particular vulnerability in this case was the  $\alpha_{CB}$  parameter, referred to as the “CB cut off” parameter. It represents the value, in units of  $\sigma_{CB}$ , of the position where the Gaussian shape turns into a power law. To overcome this instability the value of  $\alpha_{CB}$  could have been fixed to a value reasonably expected from the Monte Carlo, however that could have affected the result of the fit procedure.

To study this effect, we perform a series of fits with the  $\alpha_{CB}$  parameter fixed to a value in the range from 1.0 to 2.0. The effect on  $\Delta m_{CB}$  for the barrel and endcap regions is presented in Figures 7.7 and 7.8 respectively.

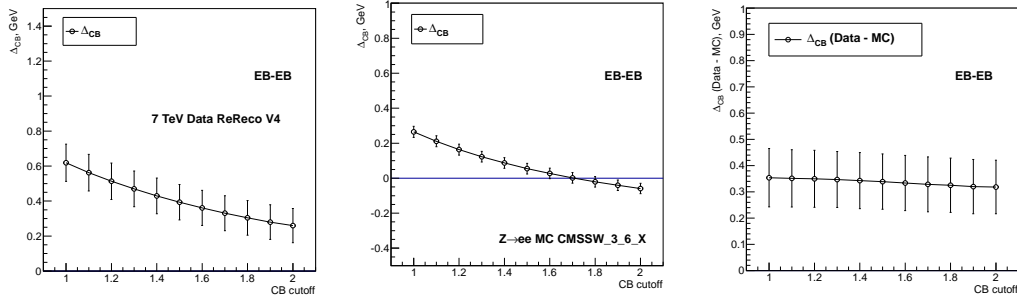


Figure 7.7: The effect of  $\alpha$  parameter variation in the  $\text{CB} \otimes \text{BW}$  fit on the  $\Delta m_{CB}$  in the barrel region. Fit results obtained from the fit to the data (left), to MC (center), and the difference between the data and MC (right).

While  $\Delta m_{CB}$  is affected by the particular choice of the  $\alpha_{CB}$  the difference  $\Delta m_{CB}(\text{data}) - \Delta m_{CB}(\text{MC})$  shows little variation. Special care must be taken when a fixed  $\alpha_{CB}$  parameter is considered. While the effect on the difference of  $\Delta m_{CB}$  between the data and MC is small, in this analysis we always let the  $\alpha_{CB}$  float when performing fitting procedure.

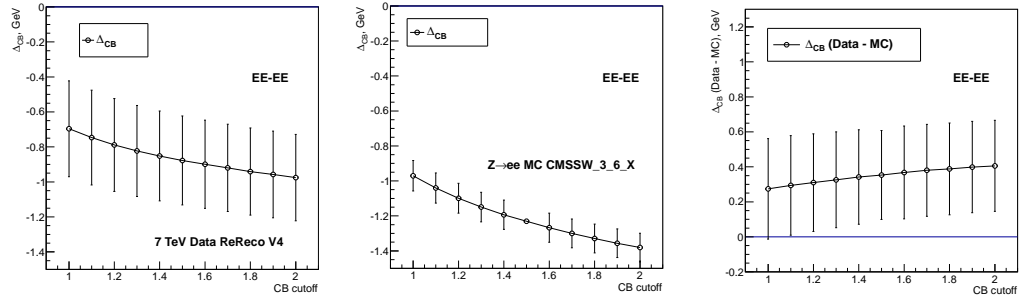


Figure 7.8: The effect of  $\alpha$  parameter variation in the  $CB \otimes BW$  fit on the  $\Delta m_{CB}$  in the endcap region. Fit results obtained from the fit to the data (left), to MC (center), and the difference between the data and MC (right).

## 7.3 Summary

The ECAL energy scale should be continuously and precisely monitored, as this is key to maintaining the high resolution of the ECAL and thus the sensitivity to many potential new physics channels, including the  $Z'$  channel presented in this thesis.

The unbinned likelihood fit to the convolution of the Crystal Ball and the Breit-Wigner shapes, discussed in this chapter, provides us with a method to measure both the ECAL energy scale and resolution. The difference  $\Delta m_{CB}(data) - \Delta m_{CB}(MC)$  estimates the deviation of the energy scale in the data with respect to our expectations from the Monte Carlo, while  $\sigma_{CB}(extra)$  (see Equation 7.10) provides us with a measure by which we can estimate realistically the ECAL mass resolution by adjusting our Monte Carlo expectations.



# Chapter 8

## Search for Heavy Neutral Resonances

As discussed in Section 2.3, a number of theoretical models of physics beyond the Standard Model predict the existence of a heavy neutral gauge boson [14, 15, 16, 19, 17], generically referred to as  $Z'$ . If such a particle exists, the CMS detector is capable of capturing its production at the LHC. In particular, the  $Z' \rightarrow e^+e^-$  decay channel has a clear final state signature, and its signal would manifest itself as a peak on the smoothly falling background in the  $e^+e^-$  invariant mass distribution.

The most prominent Standard Model process that contributes to the  $e^+e^-$  invariant mass spectrum is Drell–Yan production [102] (Figure 8.1), and is the irreducible background to this search. A relatively small (10 - 15 % of the total) background contribution comes from  $t\bar{t}$ ,  $tW$ , and diboson production when the secondary electrons are identified as the primary ones. An even smaller background (2 - 4 % of the total) originates from QCD di-jet events when the jets are misidentified as electrons.

The search for  $Z'$  is performed using a so-called “shape-based” analysis. An extended unbinned likelihood function based on the analytical shapes of the background and expected signal is constructed from the  $e^+e^-$  invariant mass spectrum, and is used to infer the compatibility of the observed invariant mass spectrum with the existence of a new heavy  $e^+e^-$  resonance (see Section 8.6.3).

This analysis is based on the data set collected by the CMS detector during the 2011 proton-proton data-taking period corresponding to an integrated luminosity<sup>1</sup> of  $5.0 \text{ fb}^{-1}$ .

---

<sup>1</sup>The total integrated luminosity of  $5.6 \text{ fb}^{-1}$  has been recorded by the CMS detector during the 2011 proton-proton data-taking period. However some of the CMS sub-systems were not fully

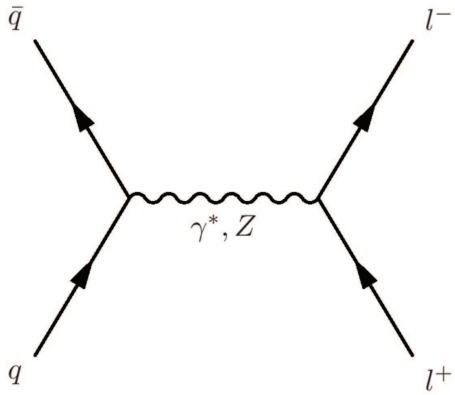


Figure 8.1: Feynman diagram of the tree level Drell–Yan process.

In the following sections I will discuss the event selection and its efficiency, the mass resolution parametrization and energy scale validation, the methods used for background estimation, and present the results of a search for a heavy  $e^+e^-$  resonance.

For the remainder of the chapter I will sometimes refer to both electrons and positrons as “electrons”, and to an  $e^+e^-$  pair as a “dielectron” pair.

## 8.1 Event selection

If  $Z'$  particles exist, they would produce a distinct signature in the CMS detector consisting of a highly energetic  $e^+e^-$  pair, as illustrated in Figure 8.2. To identify events with a similar topology, we apply the selection criteria summarized below.

We require that the event has at least one good reconstructed vertex, defined as a vertex with at least 4 associated tracks, located less than 2 cm from the center of the detector in the direction transverse to the beam, and within 24 cm from the center in the direction along the beam.

We select events that have been triggered by one of the “dielectron” or “diphoton” triggers. Trigger selection and the data sets used to select candidate events are summarized in Section 8.1.1.

---

operational at times, so that some of the data couldn’t be reliably reconstructed. The final physics analysis data set corresponding to an integrated luminosity of  $5.0 \text{ fb}^{-1}$  was obtained by removing the affected data.

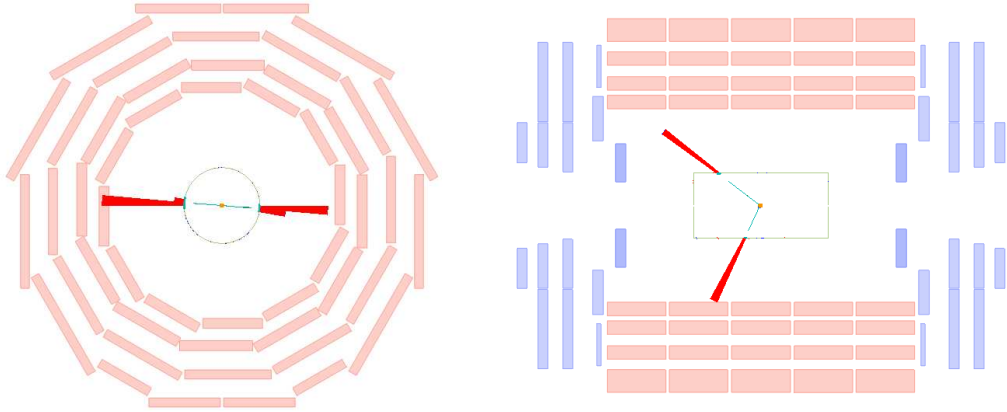


Figure 8.2: CMS event display for a  $Z'_{SSM}$  candidate in simulation. The blue tracks correspond to electron tracks, and the red towers are electron energy depositions in the ECAL. Only the tracks with  $p_T > 3$  GeV are shown.

We require the events to have two electrons that both pass the selection criteria for high energy electrons summarized in Section 6.3. Only the highest  $p_T$  pair is selected in the case where more than two electrons satisfy the selection criteria. We further require that at least one of the electrons is in the ECAL barrel region ( $|\eta_{SC}| < 1.442^1$ ). This requirement is applied due to the higher rate of jets being misidentified as electrons in the ECAL endcap region (2 – 7 %, see Section 8.5.3), thus reducing the signal over background ratio.

No charge requirement is applied to the electron candidates, as the 1 – 3 % charge misidentification rate [104] would result in a 2 – 6 % efficiency loss, thus decreasing the possible reach of the search for  $e^+e^-$  resonances.

### 8.1.1 Data sets and trigger

This analysis is based on the data set collected during the 2011 proton-proton data-taking period, corresponding to an integrated luminosity of  $5.0 \text{ fb}^{-1}$ . The 2011 data-taking period is split into two major periods, 2011A and 2011B. The 2011B period is characterized by a higher instantaneous luminosity of  $2 - 3 \times 10^{33} \text{ cm}^{-2}\text{s}^{-1}$  and

---

<sup>1</sup>An electron is considered to be reconstructed within the ECAL barrel region if the position of the ECAL supercluster associated to the electron is in the ECAL barrel, defined as  $|\eta_{SC}| < 1.442$  to exclude superclusters on the border between the ECAL barrel and endcap regions.

Data set Name	run-number
/Photon/Run2011A-05Jul2011ReReco-ECAL-v1/AOD	160404 - 168437
/Photon/Run2011A-05Aug2011-v1/AOD	170249 - 172619
/Photon/Run2011A-PromptReco-v6/AOD	172620 - 175770
/Photon/Run2011B-PromptReco-v1/AOD	175832 - 180252

Table 8.1: A summary of the data sets used in the analysis.

a higher pile up of 11 events per bunch crossing on average [103], compared to  $0.1 - 2 \times 10^{33} \text{ cm}^{-2}\text{s}^{-1}$  instantaneous luminosity and an average pileup of 6 for the run 2011A. Due to the increased instantaneous luminosity in run 2011B, most of the low  $E_T$  electromagnetic triggers have been prescaled to allow the CMS computing system to cope with the influx of collected data.

As CMS accumulated data throughout the year, our understanding of the detector continually improved. In particular, more data was available for the in-situ ECAL intercalibration. Understanding of the ECAL crystal transparency changes and performance of the ECAL laser monitoring system also improved. Therefore, the data collected in earlier periods have been reprocessed to take advantage of the improved detector understanding. The list of data sets used in the analysis corresponding to several versions of the data reprocessing is summarized in Table 8.1.

Additionally, only the lumisections qualified by the data quality monitoring as “Good”, meaning all the sub-detectors functioning normally, were selected. Approximately 5 % of the data recorded by CMS have been disqualified for one reason or another.

While the “Photon” Primary Dataset (PD)<sup>1</sup> is the main analysis data set, “DoubleElectron” and “MuEG” Primary Datasets have been used for supporting investigations. The DoubleElectron data set was used to validate the electron energy scale and to derive the dielectron mass resolution parametrization (Section 8.4). It contains an unprescaled double electron trigger which has a low enough  $E_T$  threshold<sup>2</sup> as to not distort the dielectron Z peak. The MuEG PD was used to validate the Monte Carlo contribution from flavor symmetric processes such as  $t\bar{t}$ ,  $tW$ , and diboson production

Trigger	run range
HLT_DoublePhoton33	160404-163869
HLT_DoubleEle33_CaloIdL	165088-180252
HLT_DoubleEle33_CaloIdT	178420-180252
HLT_DoubleEle45_CaloIdL	178420-180252

Table 8.2: The triggers used in the analysis, together with their run ranges. The HLT\_DoubleEle33\_CaloIdL trigger was occasionally prescaled for runs after 178420.

(Section 8.5.2).

The signal events are collected by a combination of the diphoton and dielectron triggers, as summarized in Table 8.2. The majority of the data was recorded by the HLT\_DoubleEle33\_CaloIdL trigger. When instantaneous luminosity reached  $3 \times 10^{33} \text{ cm}^{-2}\text{s}^{-1}$  this trigger was pre-scaled. For the remainder of the year the HLT\_DoubleEle33\_CaloIdT and HLT\_DoubleEle45\_CaloIdL triggers were used for signal selection.

All signal triggers require two superclusters with  $\text{H}/\text{E} < 0.15$  in the barrel and  $\text{H}/\text{E} < 0.1$  in the endcap, where  $\text{H}/\text{E}$  is the ratio of the energy deposited in the HCAL to that in the ECAL. The HLT\_DoubleEle33\_CaloIdL trigger additionally requires that the clusters pass a loose shower-shape cut ( $\sigma_{inj\eta}^3 < 0.014$  in barrel and  $\sigma_{inj\eta} < 0.035$  in endcap) and have an online pixel match. The HLT\_DoubleEle33\_CaloIdT trigger further tightens the shower-shape cut to  $\sigma_{inj\eta} < 0.011$  in the barrel and  $\sigma_{inj\eta} < 0.031$  in the endcap. The number in the trigger naming scheme (e.g., 33) corresponds to the  $E_T$  threshold applied to the superclusters.

Simulated event samples for the signal and background processes were gener-

<sup>1</sup>The data collected by the CMS was grouped in Primary Datasets (PD’s) based on a set of similar triggers. The “Photon” PD contains events triggered by a collection of photon triggers. The “DoubleElectron” and “MuEG” PD’s contain events triggered by a collection of dielectron triggers, and a combination of photon-muon and electron-muon triggers, respectively.

<sup>2</sup>Throughout the 2011 data-taking the trigger HLT\_Ele17\_Y\_Ele8\_Y, Y=CaloIdL\_CaloIsoVL, remained unprescaled. This trigger requires two HLT electrons that have  $E_T$  above 17 and 8 GeV respectively.

<sup>3</sup>The shower shape variable  $\sigma_{inj\eta}$  is the energy-weighted width of the supercluster in  $\eta$  direction (see, Section 6.1.2)

ated with the PYTHIA, MADGRAPH, and POWHEG event generators. The MADGRAPH [105] matrix-element generator was used for  $t\bar{t}$  and W + jets samples, while the POWHEG framework [106] was used for the Drell-Yan process. Both of these generators were interfaced with the PYTHIA [107] parton-shower generator. All other processes were generated using PYTHIA. The CTEQ6L1 [108] parton distribution function (PDF) was used for all the samples. The response of the detector was simulated in detail using GEANT4 [109]. These samples were further processed through the trigger emulation and event reconstruction chain of the CMS experiment.

## 8.2 Validation of the Monte Carlo simulation with the data

In order to validate the data reconstruction and to show that the simulation adequately describes the data, we perform Data versus Monte Carlo comparisons. These comparisons are done in the signal-enriched region near the Z peak ( $80 \text{ GeV} < M_{ee} < 100 \text{ GeV}$ ). In Figures 8.3 through 8.6, we present results of the comparisons performed on a set of events that pass the analysis selection criteria. The comparison is made for all the variables that enter the electron identification criteria (see Chapter 6).

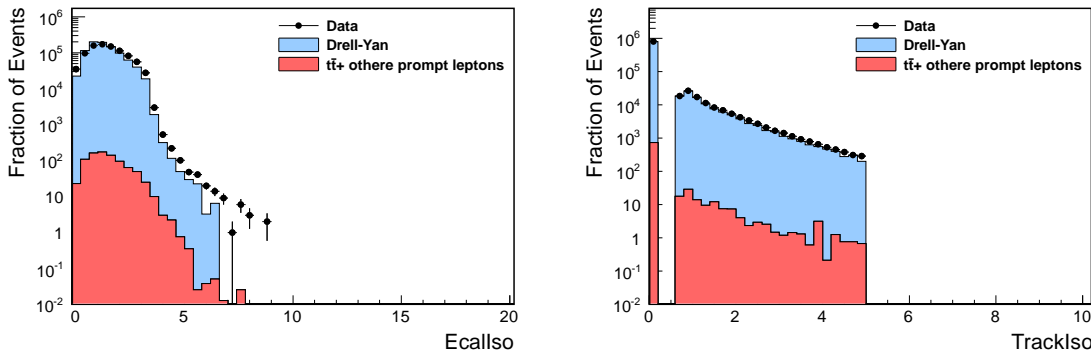


Figure 8.3: The data vs. simulation comparison for the isolation variables in the barrel region for the pairs of electrons that pass the analysis selection, with their invariant mass in the Z mass window. The data is represented by points with error bars, and the MC simulation is represented by filled histograms. The Drell-Yan process is shown in blue, while in red the combination of samples that are sources of secondary electrons ( $t\bar{t}$ ,  $tW$ ,  $W + \text{jets}$  and diboson production) is presented.

As is illustrated in Figures 8.3 through 8.6, the data is reasonably well described by the MC simulation. This provides confidence in the data reconstruction and electron identification.

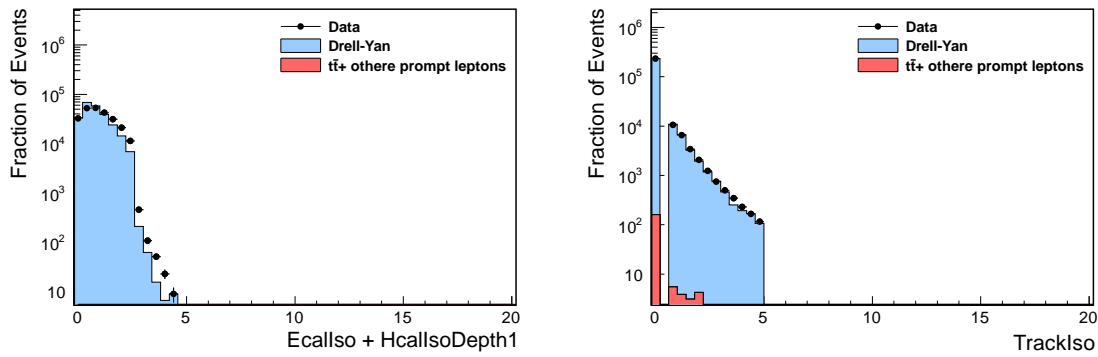


Figure 8.4: The data vs. simulation comparison for the isolation variables in the endcap region for the pairs of electrons that pass the analysis selection, with their invariant mass in the Z mass window. The data is represented by points with error bars, and the MC simulation is represented by filled histograms. The Drell-Yan process is shown in blue, while in red the combination of samples that are sources of secondary electrons ( $t\bar{t}$ ,  $tW$ ,  $W + \text{jets}$  and diboson production) is presented.

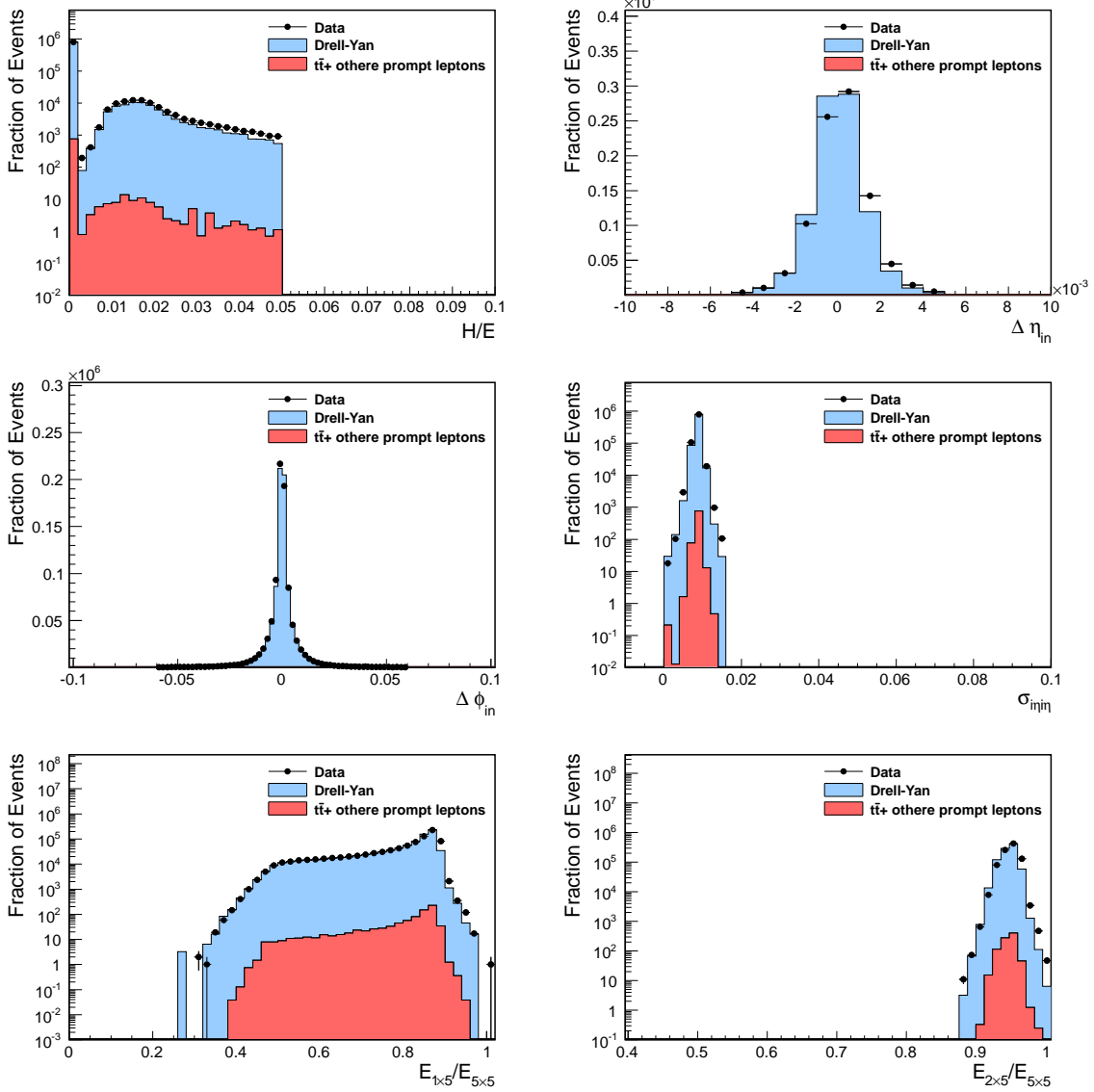


Figure 8.5: The data vs. simulation comparison for the identification variables in the barrel region for the pairs of electrons that pass the analysis selection, with their invariant mass in the Z mass window. The data is represented by points with error bars, and the MC simulation is represented by filled histograms. The Drell-Yan process is shown in blue, while in red the combination of samples that are sources of secondary electrons ( $t\bar{t}$ ,  $tW$ ,  $W +$  jets and diboson production) is presented.

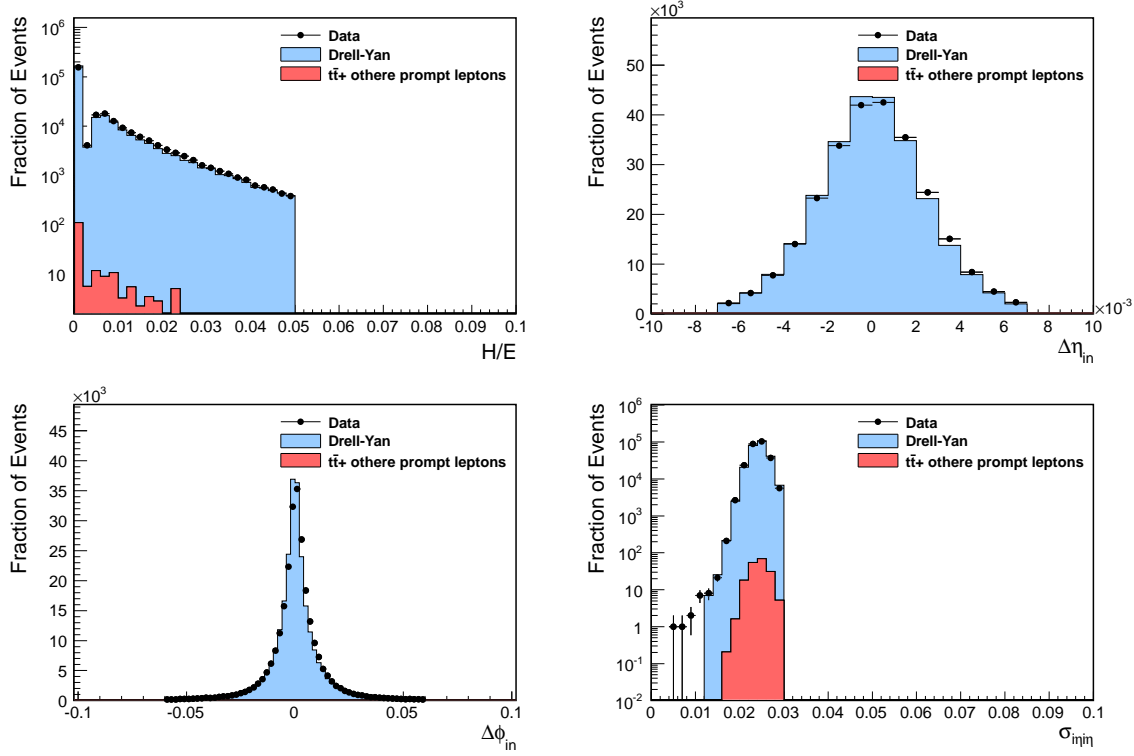


Figure 8.6: The data vs. simulation comparison for the identification variables in the endcap region for the pairs of electrons that pass analysis the selection, with their invariant mass in the Z mass window. The data is represented by points with error bars, and the MC simulation is represented by filled histograms. The Drell-Yan process is shown in blue, while in red the combination of samples that are sources of secondary electrons ( $t\bar{t}$ ,  $tW$ ,  $W +$  jets and diboson production) is presented.

## 8.3 Selection efficiency

### 8.3.1 Trigger efficiency

The trigger efficiencies are divided into three parts: the Level 1 (L1) trigger selection, an online  $E_T$  cut (turn on effect), and the online electron identification.

All signal triggers require one of the electrons to pass the L1 trigger. Out of the 504518 events selected by the analysis using the HLT\_DoubleEle33\_CaloIdL trigger, 500369 have both electrons passing L1. This implies an efficiency of  $99.58 \pm 0.01\%$ <sup>1</sup> for a selected electron to pass L1. Since only one electron is required to pass the L1 trigger, the L1 efficiency of the signal triggers is effectively 100 %<sup>2</sup>.

The online  $E_T$  cut of 33 GeV has been estimated to be 100 % efficient above 35 GeV in the barrel and above 45 GeV in the endcap [94]. The endcap region was affected by the fact that the laser transparency corrections have not been applied at the trigger level, but were available only for the offline reconstruction.

The final component of the efficiency comes from the online pixel-match and shower-shape cuts. It was estimated as the fraction of the events selected by the double photon trigger that pass double electron trigger. The efficiency was found to be  $99.7 \pm 0.2\%$ .

To summarize, for events with two electrons passing signal selection and with  $E_T$  above 35 GeV in the barrel and above 45 GeV in the endcap, the trigger efficiency is taken to be 100 %. Therefore, no trigger requirements are applied on the Monte Carlo simulated samples.

---

<sup>1</sup>If  $p_{L1}$  is the probability of an electron passing analysis selection to pass L1 criteria, and  $N_1$  is the number of events that have at least one electron passing the L1 criteria (in our case 504518) and  $N_2$  is the number of events that have both electrons passing L1 (in our case 500369), then  $p_{L1} = 2N_2/(N_1 + N_2)$ . This comes from a simple consideration: assume  $N$  is the total number of the events with two electrons passing the selection criteria, then  $N_1 = N(1 - (1 - p_{L1})^2)$  and  $N_2 = Np_{L1}^2$ . Solving for  $p_{L1}$  gives us the formula above.

<sup>2</sup>If  $p_{L1}$  is the probability of an electron that passed the analysis selection to pass the L1 criteria, then the probability to have at least one out of two electrons that pass the analysis selection to pass the L1 criteria is  $1 - (1 - p_{L1})^2$ .

### 8.3.2 Electron identification efficiency scale factors

To estimate the data to MC efficiency scale factor, the electron identification efficiency was measured both in the data and the MC using a “tag and probe” method [98, 99]. A pair of electrons forms a “tag and probe” pair, where one electron satisfies a stringent selection requirement (the “tag”) and the second electron (the “probe”) satisfies a relaxed selection requirement. The invariant mass of the pair should belong to the the region of high signal purity (for example close to the Z mass). Then the efficiency of the selection criteria in question is determined as the rate at which the probe passes these criteria.

The efficiencies were measured in the  $Z$  peak region  $60 < M_{ee} < 120$  GeV, where a sample of electrons with high purity is available. The data to MC efficiency scale factors for the high energy electron selection criteria was found to be  $0.993 \pm 0.007$  and  $0.992 \pm 0.004$  for the barrel and the endcap regions, respectively [99, 94]. These factors are used to correct the Monte Carlo signal efficiencies used in the analysis.

An additional measurement of the efficiency scale factors in the high mass Drell-Yan tail  $M_{ee} > 140$  GeV was used as a systematic cross check. The value of the scale factors was found to be  $0.976 \pm 0.013$  and  $0.980 \pm 0.014$  for the barrel and the endcap regions, respectively. As a result, a conservative uncertainty of 2 % is assigned to the efficiency scale factors derived by this method.

### 8.3.3 Total reconstruction and identification efficiency

The total electron reconstruction and selection efficiency is factorized as:  $\varepsilon = \varepsilon_{cand} \times \varepsilon_{id}$ , where  $\varepsilon_{cand}$  is the efficiency for an electron to be reconstructed as an electron candidate, and  $\varepsilon_{id}$  is the efficiency for an electron candidate to pass all the high energy electron selection criteria. The  $\varepsilon_{cand}$  efficiency is common for all CMS analyses, and is determined by the CMS Electron and Photon Commissioning group [100], and the corresponding data-MC scale factor was found to be consistent with one [101].

The total reconstruction and selection efficiency as a function of  $E_T^{truth}$  predicted by the Monte Carlo simulation is shown in Figure 8.7. The efficiency is in the range

of 76 % to 89 % in the barrel, and from 75 % to 88 % in the endcap. The signal efficiency parametrization for the statistical data interpretation is further discussed in Section 8.6.2.

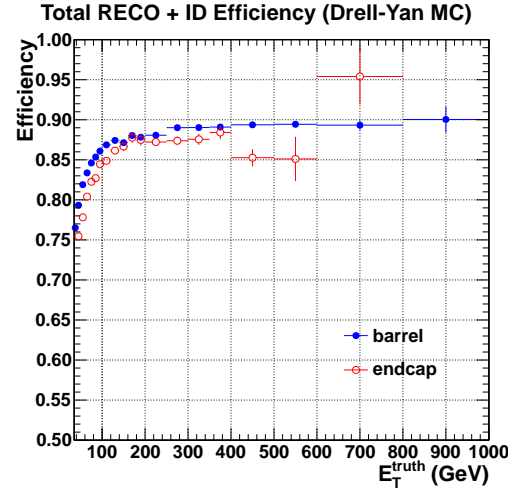


Figure 8.7: The MC estimated total reconstruction and selection efficiency vs  $E_T^{truth}$ .

## 8.4 Dielectron mass resolution and electron energy scale

### 8.4.1 Energy scale validation

The electron energy scale is validated in the data with respect to the Monte Carlo (MC) following the method described in Section 7.2. The results of the fit to the Crystal Ball (CB) convoluted with the Breit Wigner (BW) function at the Z peak are presented in Figures 8.8 and 8.9, both for the data and the MC. The  $\Delta m_{CB}$  parameter represents the shift of the Z mass peak position with respect to the PDG value of the Z mass. The values of this parameter measured in the data and the MC are summarized in Table 8.3. The electron energy scale is found to be in good agreement between the data and the MC in the category with both electron candidates in the barrel region, and in the category with one electron in the barrel and one electron in the endcap region. A slight disagreement of  $\approx 1\%$  is observed in the category with both electrons in the endcap.

region	$\Delta m_{CB}(\text{Data}), \text{GeV}/c^2$	$\Delta m_{CB}(\text{MC}), \text{GeV}/c^2$
EB-EB	$0.04 \pm 0.01$	$0.52 \pm 0.01$
EB-EE	$1.34 \pm 0.01$	$1.04 \pm 0.02$
EE-EE	$2.02 \pm 0.02$	$1.12 \pm 0.03$
EB-EB & EB-EE	$0.27 \pm 0.01$	$0.64 \pm 0.01$

region	$\frac{\Delta m_{CB}(\text{Data}) - \Delta m_{CB}(\text{MC})}{m(Z^0)}, \%$
EB-EB	$-0.53 \pm 0.02$
EB-EE	$0.32 \pm 0.03$
EE-EE	$0.99 \pm 0.04$
EB-EB & EB-EE	$-0.40 \pm 0.02$

Table 8.3: The electron energy scale summary for the different ECAL regions as measured at the Z peak. Comparison between the data and MC.

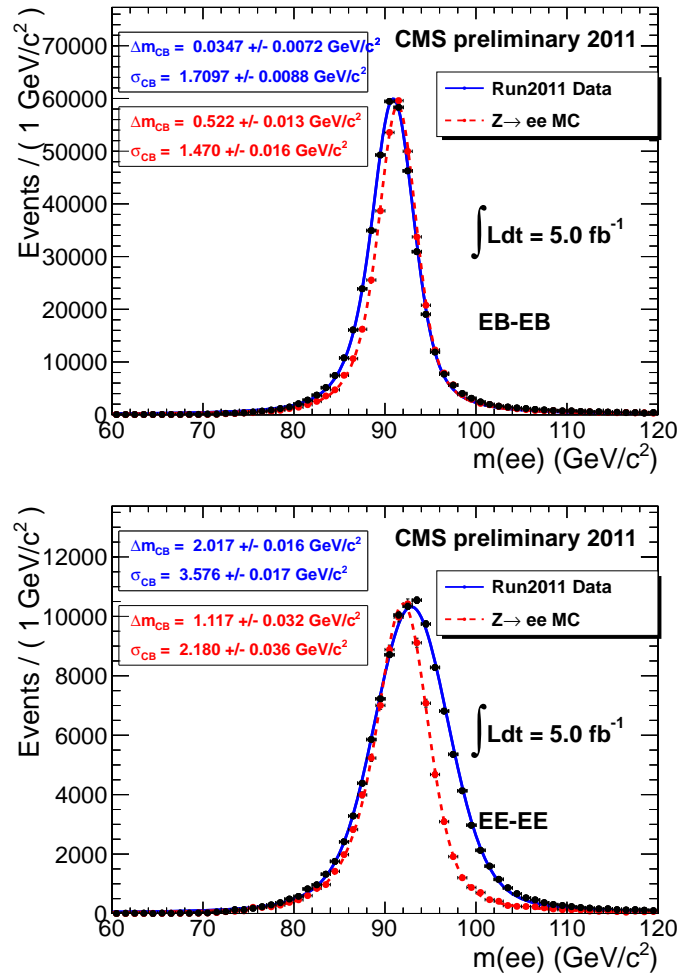


Figure 8.8: The invariant mass spectrum of the data and MC overlaid with the CB $\otimes$ BW fit results. Left: both electron candidates in the ECAL barrel region (EB-EB), right: both electron candidates in the ECAL endcap region (EE-EE).

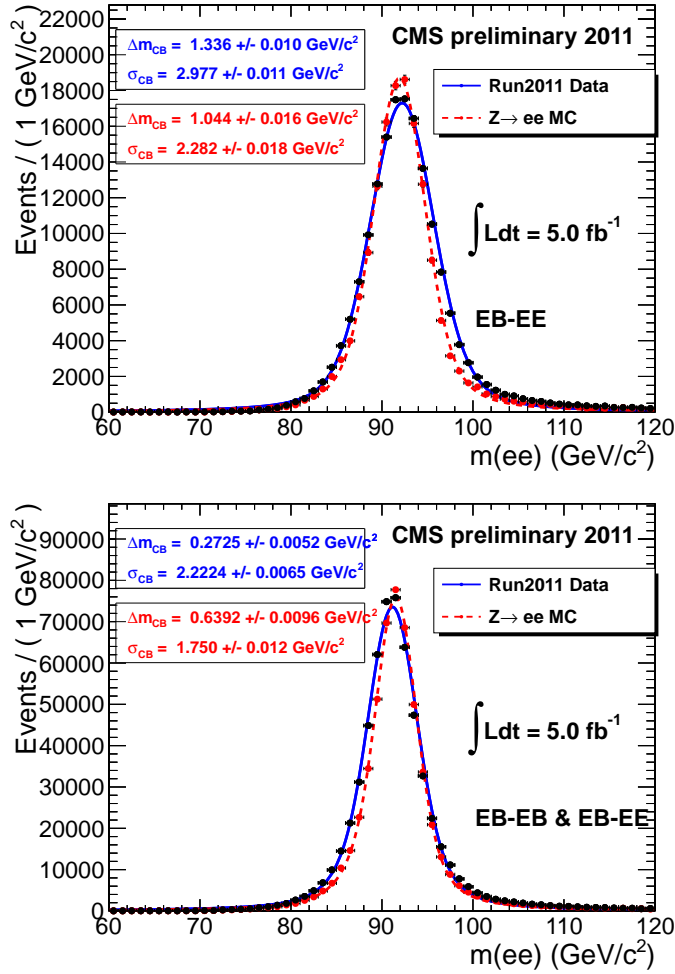


Figure 8.9: The invariant mass spectrum of the data and MC overlaid with the  $\text{CB} \otimes \text{BW}$  fit results. Left: one of the electron candidates is in the ECAL barrel region and the other one in the ECAL endcap (EB-EE), right: one of the electron candidates is in the ECAL barrel region and the other one in the ECAL endcap, or both electron candidates in the ECAL barrel region (EB-EB & EB-EE).

### 8.4.2 Resolution parametrization

To quantify the dielectron mass resolution we use the  $\sigma_{CB}$  parameter of the Crystal Ball (CB) convoluted with Breit Wigner (BW) function as described in Section 7.2. The results of these measurements at the Z peak are summarized in Table 8.4. The difference in the dielectron mass resolution between the data and the MC is assigned to the difference between the constant terms of the ECAL energy resolution (see Section 3.2.3).  $\sigma_{CB}(\text{extra})$ , defined as  $\sqrt{\sigma_{CB}(\text{Data})^2 - \sigma_{CB}(\text{MC})^2}$ , is used to estimate the dielectron mass resolution in the high mass region.  $\sigma_{CB}(\text{extra})$  is added in quadrature to  $\sigma_{CB}(\text{MC})$  expected from the MC in the mass region of interest.

region	$\sigma_{CB}(\text{Data}), \%$	$\sigma_{CB}(\text{MC}), \%$	$\sigma_{CB}(\text{extra}), \%$
EB-EB	$1.87 \pm 0.01$	$1.62 \pm 0.02$	$0.96 \pm 0.02$
EB-EE	$3.26 \pm 0.02$	$2.51 \pm 0.02$	$2.10 \pm 0.03$
EE-EE	$3.92 \pm 0.02$	$2.40 \pm 0.04$	$3.11 \pm 0.04$
EB-EB & EB-EE	$2.43 \pm 0.01$	$1.92 \pm 0.01$	$1.50 \pm 0.02$

Table 8.4: The dielectron mass resolution for different ECAL regions, as measured at the Z peak for the data and the MC. For the definition of parameters, see the text.

To estimate the resolution in the MC at high mass we use a CB fit to  $m_{\text{RECO}} - m_{\text{true}_{\text{MC}}}$  derived from the Drell-Yan MC in different mass regions, where  $m_{\text{RECO}}$  is the dielectron invariant mass as measured after the detector simulation and reconstruction, and  $m_{\text{true}_{\text{MC}}}$  is the dielectron invariant mass at generator level. This was also validated with the CB $\otimes$ BW fit to the Z' signal MC. The two methods show good agreement with each other [110], and the first method is chosen for use. The Drell-Yan MC provides more data points for the resolution parametrization, as opposed to the discrete values for the Z' MC masses. Results of these estimates corrected by  $\sigma_{CB}(\text{extra})$  derived at the Z peak are shown in Figures 8.10 and 8.11. A parametrization similar to the ECAL energy resolution parametrization (Section 3.2.3) is used to describe the mass resolution as a function of mass.

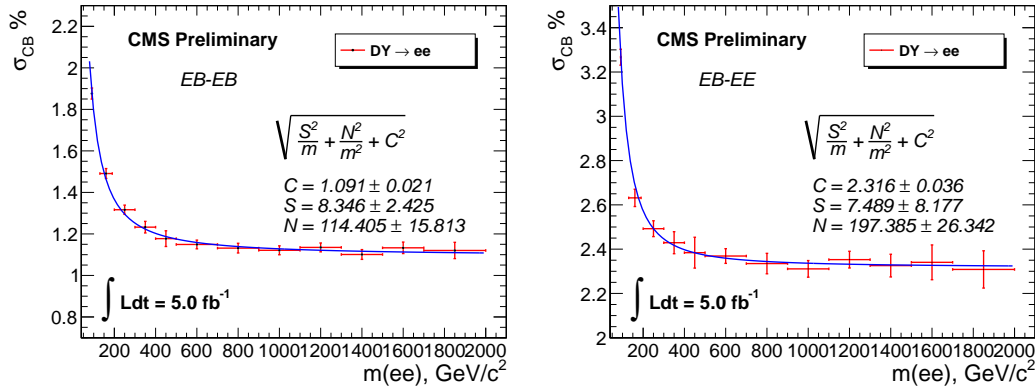


Figure 8.10: The dielectron mass resolution as a function of the mass, derived from the DY MC and corrected by the  $\sigma_{CB}(\text{extra})$  measured at the Z peak. Left: both electron candidates in the ECAL barrel region, right: one of the electron candidates in the ECAL barrel region and the other in the ECAL endcap region.

### 8.4.3 Energy scale evolution

The behavior of the electron energy scale in different time periods of the 2011 data-taking has been investigated, to evaluate the electron energy scale change throughout the year.

First we split the data set in two run periods, corresponding to Run2011A and Run2011B. The results for each run period are shown in Figure 8.12. A slight negative overall shift of the electron energy scale is observed in the Run2011B period with respect to the Run2011A period. The Run2011B period is characterized by higher pile up conditions and increased instantaneous luminosity.

The Run2011B period is further subdivided in 5 sub-periods to investigate the behavior of the electron energy scale in more detail. The results of these measurements are summarized in Table 8.5. A small positive drift, less than 1 %, is observed in the endcap, and a small negative drift, less than 0.5 % is observed in the barrel in the Run2011B period. As a result, conservative systematic uncertainties of 1 % and 2 % are assigned to the electron energy scales in the barrel and the endcap regions, respectively.

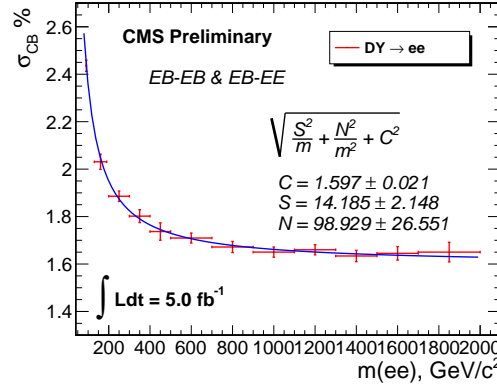


Figure 8.11: The dielectron mass resolution as a function of the mass, derived from the DY MC and corrected by the  $\sigma_{CB}(\text{extra})$  measured at the Z peak, for the EB-EB and EB-EE categories.

Run Range	EB-EB	EB-EE	EE-EE	EB-EB & EB-EE
Run2011A All of (160404-175770)	- 0.33 $\pm$ 0.02	0.08 $\pm$ 0.02	0.65 $\pm$ 0.04	- 0.31 $\pm$ 0.02
Run2011B All of (175832-180252)	- 0.74 $\pm$ 0.02	0.58 $\pm$ 0.03	1.34 $\pm$ 0.04	- 0.49 $\pm$ 0.02
Run2011B	175832-177515	- 0.65 $\pm$ 0.02	0.32 $\pm$ 0.02	0.92 $\pm$ 0.05
	177516-178078	- 0.60 $\pm$ 0.03	0.72 $\pm$ 0.05	1.53 $\pm$ 0.07
	178079-178677	- 0.82 $\pm$ 0.02	0.77 $\pm$ 0.04	1.74 $\pm$ 0.07
	178678-179431	- 0.76 $\pm$ 0.03	0.79 $\pm$ 0.05	1.67 $\pm$ 0.08
	179432-180252	- 0.99 $\pm$ 0.03	0.88 $\pm$ 0.05	1.75 $\pm$ 0.07

Table 8.5:  $(\Delta m_{CB}(\text{Data}) - \Delta m_{CB}(\text{MC})) / m(Z^0)$  in % for the different run periods and electron topologies.

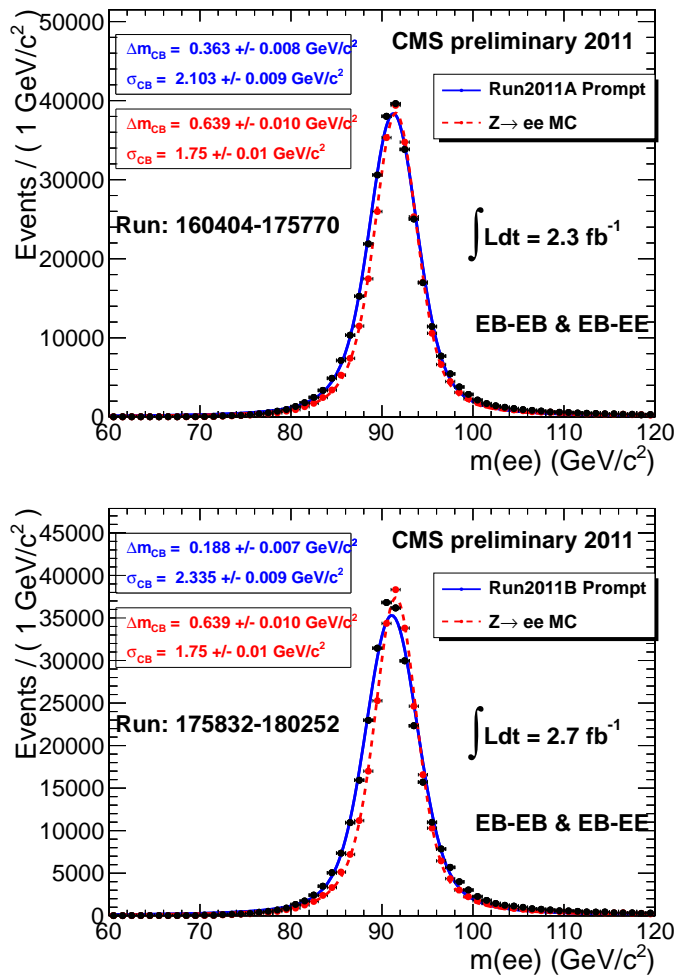


Figure 8.12: The invariant mass spectrum of the data and MC overlaid with the  $\text{CB} \otimes \text{BW}$  fit results for EB-EB & EB-EE category. Top: Run2011A, bottom: Run2011B.

## 8.5 Background estimation

Standard Model processes that contribute to the dielectron mass spectrum can be divided into three distinct categories:

- Drell–Yan production ( $Z/\gamma^*$ ) - this is the main Standard Model process that contributes to the dielectron mass spectrum, and represents what is sometimes referred to as “irreducible background”<sup>1</sup>. This category accounts for 88 % of the events in the mass region above 120 GeV.
- Events with secondary electrons produced in leptonic decays of  $t\bar{t}$ ,  $tW$ , diboson production, and Drell–Yan in the  $\tau\tau$  channel. This category<sup>2</sup> accounts for less than 9 % of the events in the mass region above 120 GeV.
- Events with one or more misidentified electrons, such as  $W+\text{jets}$  or multi-jet events, where the jet is misidentified as an electron. This category accounts for less than 3 % of the background in the mass region above 120 GeV.

Contributions from the first two categories are estimated from Monte Carlo simulation. The Drell–Yan contribution is normalized to the number of events observed in the  $Z$  peak region. The contribution from secondary electrons is validated using  $e\mu$  events, as these processes are flavor symmetric. The contribution from misidentified electrons is estimated directly from data, based on the probability of a jet to be misidentified as an electron. These procedures are described in the following sections.

### 8.5.1 Standard Model Drell-Yan

The contribution of the Standard Model Drell–Yan process to the invariant mass spectrum is estimated based on the POWHEG event generator [106], which includes next-to-leading order matrix element calculations. This background is scaled to the

---

<sup>1</sup>Electron pairs produced in the Drell–Yan process are identical to those arising from  $Z'$  decays, and represent pairs of prompt electrons.

<sup>2</sup>This category is sometimes referred to as “ $t\bar{t}$  and other prompt leptons”. Where “other” refers to other than Drell–Yan electrons.

observed number of dielectron events in the Z peak region (60–120 GeV), which removes the uncertainty due to the luminosity measurement. Normalization to the Z peak region in the data also allows us to remove the uncertainty on the absolute value of the Drell-Yan cross section, leaving the main uncertainty only on the relative ( $\sigma(Z/\gamma^*)_{\text{High mass}} / \sigma(Z/\gamma^*)_{\text{Z peak}}$ ) differential cross section.

The uncertainty on the Drell-Yan differential cross section (relative to the cross section at the Z peak) due to the parton distribution function (PDF) uncertainty is estimated to be 5 to 20 % in the mass range of 400–2000 GeV [112]. An average uncertainty of 10 % on the Drell-Yan event yield prediction is assumed.

To estimate the Drell-Yan mass spectrum variation due to the different orders of precision in the cross section calculation, we compare the leading order (LO) PYTHIA simulation with the next-to-leading order (NLO) POWHEG event generator, as shown in Figure 8.13. The distributions are normalized to each other in the Z peak region (60–120 GeV), and agree within 6 %. Similar comparisons between LO PYTHIA and NLO (as well as NNLO) FEWZ<sub>z</sub> [115] event generators were found to agree within 6 % [113]. As a result we assign a 6 % uncertainty on the Drell-Yan event yield prediction due to the NLO calculation.

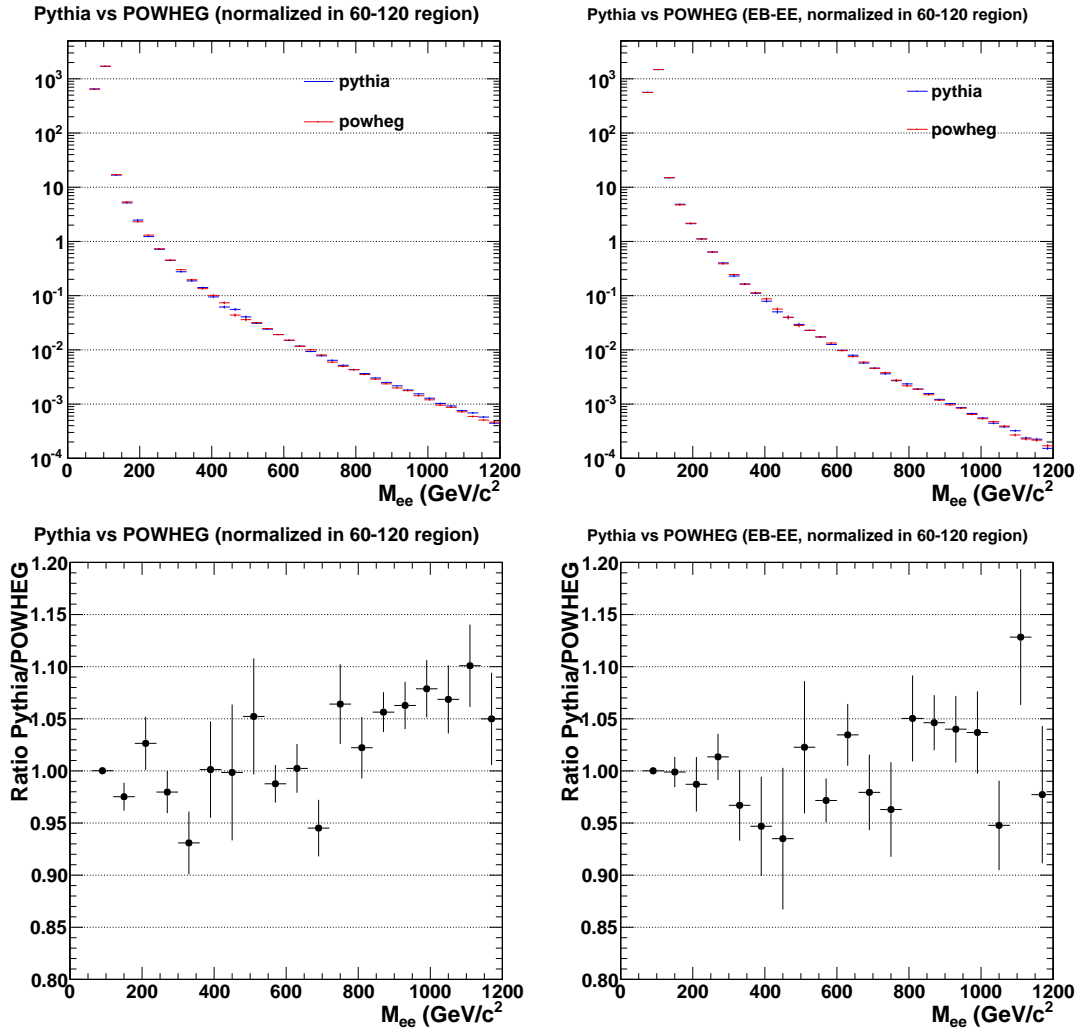


Figure 8.13: Comparison between the predictions of the (LO) PYTHIA and (NLO) POWHEG at the generator level. The top plots display the predicted mass spectra, and the bottom plots show the ratio of the two predictions. The left column corresponds to the decays with both electrons in the ECAL barrel region, while the right column corresponds to decays with one electron in the ECAL barrel and one in the endcap region.

### 8.5.2 Other prompt electrons

Pairs of prompt electrons can arise from leptonic decays of  $t\bar{t}$ ,  $tW$ ,  $WW$ ,  $WZ$  and  $Z \rightarrow \tau\tau$ , and represent the main non–Drell–Yan background. The contribution of these backgrounds to the dielectron spectrum is estimated from Monte Carlo, and represents 9 % of the total background above 120 GeV. The main contribution comes from  $t\bar{t}$ , which is simulated at next-to-leading order using MADGRAPH [105]. The uncertainty on this background estimate is dominated by the theoretical uncertainty of 15 % on the  $t\bar{t}$  production cross section [111].

These processes are lepton flavor symmetric, producing twice as many  $e\mu$  pairs as  $ee$  pairs. This enables the use of the  $e\mu$  spectrum from the data to validate the Monte Carlo estimated contribution of these processes.

Muons are required to be reconstructed as “global muons”<sup>1</sup> and satisfy the standard muon selection<sup>2</sup> used for high momentum muon analyses in CMS [112]. Electrons are required to pass the HEEP identification criteria described in Section 6.3 and to be in the ECAL fiducial region  $|\eta| < 2.5$  (excluding the barrel-endcap gap), while the muon is required to be in the region covered by the muon system ( $|\eta| < 2.4$ ). Events are selected from the “MuEG” primary data set, where the events collected using the muon-photon and muon-electron triggers are present.

The invariant mass spectrum of  $e^\pm\mu^\mp$  pairs corresponding to a luminosity of  $5.0 \text{ fb}^{-1}$  as obtained in collaboration with the CMS  $Z'$  muon analysis [112] team, and used in a common analysis by both groups, is shown in Figure 8.14 [112, 94, 114]. The contribution arising from jets being misidentified as leptons is derived from the same-sign  $e\mu$  spectrum, where the deficit of the data relative to the Monte Carlo prediction is ascribed to jets misidentified as leptons.

The number of observed  $e\mu$  events in data was found to be 3863 (1175) in the

---

<sup>1</sup>Muon tracks are reconstructed separately in both the muon system and the inner tracker, and the resulting tracks are matched and fitted simultaneously to form a so called “global muon”. More details on the muon reconstruction can be found in [116].

<sup>2</sup>Muons must have a transverse impact parameter with respect to the beam spot of less than 0.2 cm, at least one hit in the pixel detector, hits in at least nine silicon tracker layers, and matched segments in two or more muon stations. The sum of the  $p_T$  of all tracks (excluding muon track) within a cone of  $\Delta R < 0.3$  about the muon candidate’s track must be less than 10 % of the candidate’s  $p_T$ .

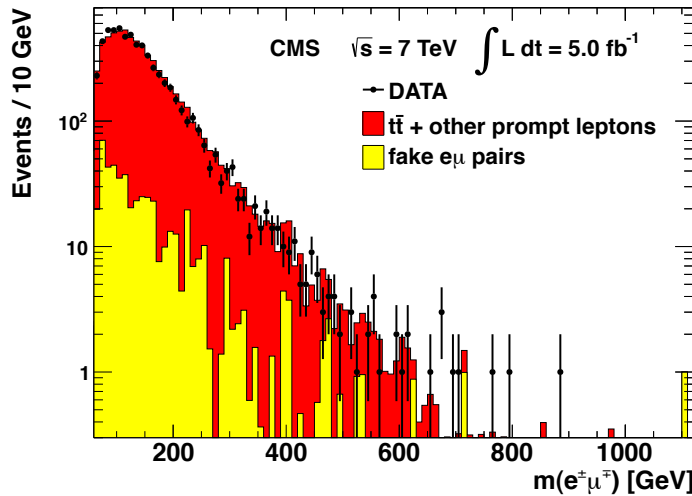


Figure 8.14: The observed opposite-sign  $e^\pm\mu^\mp$  dilepton invariant mass spectrum (data points). The filled red histogram shows the contribution to the spectrum from  $t\bar{t}$  and other sources of prompt leptons ( $tW$ , diboson production,  $Z \rightarrow \tau\tau$ ), as derived from simulations. The background where at least one of the reconstructed objects is not a real lepton is shown in yellow, and is estimated from the data using the same-sign  $e^\pm\mu^\pm$  spectrum [114].

mass region above 120 (200) GeV, and was found to compare well with the prediction from the simulation of  $4081 \pm 406$  ( $1305 \pm 123$ ) events.

The “ $e\mu$  method” provides sufficient validation of the prompt electron background contribution to the dielectron spectrum, thus providing us with confidence in the Monte Carlo estimation of these processes.

### 8.5.3 Jets and misidentified electrons

The jet background consists of contributions from multi-jet events where two jets are reconstructed as electrons,  $W + jets$  events where one jet is reconstructed as an electron, and  $\gamma + jets$  events where the photon converts and the jet is reconstructed as an electron. The jet background is estimated using the fake rate method explained below. The multi-jet component is estimated from the data, while the  $W + jets$  and  $\gamma + jets$  components are estimated from Monte Carlo samples using the fake rate probabilities derived from the data.

#### Fake rate measurement

The fake rate is defined as the probability of a jet that is reconstructed as an electron candidate and satisfies the preselection criteria, to pass the HEEP selection:

$$p_{FR}(E_T, \eta) = \frac{N_{\text{pass HEEP ID}}(E_T, \eta)}{N_{\text{pass preselection}}(E_T, \eta)}, \quad (8.1)$$

where the preselection criteria are summarized in Table 8.6.

The fake rate is measured from the data using a jet enriched sample of events with only one electron with  $E_T$  above 10 GeV (this removes most of the Drell–Yan contribution). The fake rate is then calculated as the number of electrons passing the HEEP selection, over the number of electrons that pass the preselection criteria. The contamination from  $W + jets$  and  $\gamma + jets$  is estimated from Monte Carlo simulation, and is subtracted.

The fake rate, measured as a function of the electron transverse energy, is presented in Figure 8.15 [94]. The fit results for the fake rate parametrization are also summarized in Table 8.7.

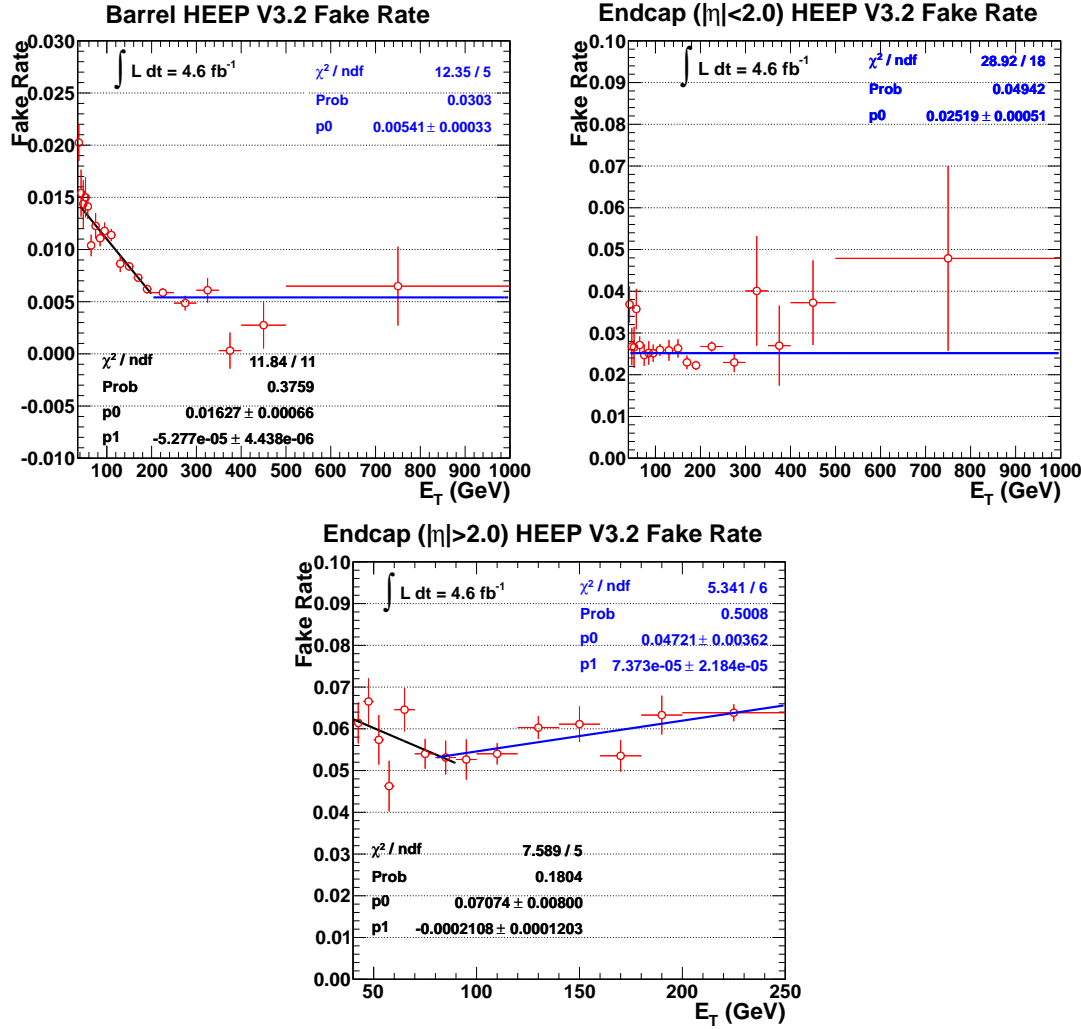


Figure 8.15: The “fake rate” probability for a jet to be identified as a HEEP electron as a function of  $E_T$  for the three pseudo-rapidity regions (with a linear fit applied).

variable	barrel	endcap
$\sigma_{in\eta}$	0.013	0.034
H/E	0.15	0.10
nr. missing hits	= 0	= 0

Table 8.6: The electron preselection requirements for the “fake rate” calculation, where  $\sigma_{in\eta}$  is the the electron shower shape, H/E is the ratio of energies deposited in the HCAL over the energy in the ECAL, and “nr. missing hits” is the number of tracker layers missing before the first hit is recorded. All of these variables are described in more detail in Chapter 6.

$\eta$ region	functional form
$ \eta  < 1.442$	for $E_T < 205.1$ : $0.01627 - 5.3 \cdot 10^{-5} \cdot E_T$ , else $5.4 \cdot 10^{-3}$
$1.56 <  \eta  < 2.0$	$0.02519$
$2.0 <  \eta  < 2.5$	for $E_T < 82.7$ : $0.07074 - 2.108 \cdot 10^{-4} \cdot E_T$ , else $0.4721 + 7.373 \cdot 10^{-5} \cdot E_T$

Table 8.7: The functional form of the “fake rate” for the three pseudo-rapidity regions.

### Jet background contribution to the dielectron mass spectrum.

The jet background contribution to the dielectron invariant mass spectrum is estimated by reweighting a sample of events with two electrons passing the preselection criteria (Table 8.6). Electrons are required to fail the HEEP selection, in order to suppress  $Z \rightarrow ee$  contamination. As a result, the event has to be weighted<sup>1</sup> by an additional  $1/(1-p_{FR})$  factor for each electron ( $p_{FR}$  defined in Equation 8.1)).

This estimate does not include the  $W + jets$  and  $\gamma + jets$  contributions (due to the requirement to fail the HEEP ID on both electrons). We estimate the contributions from these processes from the Monte Carlo simulation. We do it in a semi-data-driven way. For both  $W + jets$  and  $\gamma + jets$  we require one HEEP electron, and one preselected electron which fails HEEP selection, and we weight the events by the fake rate probability.

The jet background can also be estimated by reweighting a sample of events with one HEEP electron<sup>2</sup> and one electron passing the preselection cuts. The preselected electron is required not to pass the HEEP selection in order to reduce  $Z \rightarrow ee$  contamination. The remaining  $Z \rightarrow ee$  contamination is removed by subtracting the Monte Carlo estimation (using the same procedure as the one applied to the data).

The comparison of the two estimation methods is presented in Figure 8.16. The estimation from a sample of one HEEP-selected and one preselected electron, suffers from reduced statistics due to the application of HEEP selection to one of the electrons. That is why we use the estimation from a sample with two preselected electrons for the jet background estimation to the dielectron spectrum.

Figure 8.16, shows that both methods are in a good agreement, however statistics is low in the high mass tail. An additional investigation of the estimation to a mass spectrum with one HEEP electron and one electron passing preselection, but failing the track isolation criteria, has shown that a conservative 40 % uncertainty on the

---

<sup>1</sup>Let  $N$  be the number of jets that are reconstructed as an electron and pass preselection,  $N_{pass}$  – the number of these electrons that pass the HEEP selection, and  $N_{fail}$  the number that fail this selection. Then  $N = N_{pass} + N_{fail}$ , and  $N_{pass} = N \times p_{FR}$ , where  $p_{FR}$  is the fake rate probability. We can then estimate the number of electrons that would have passed the ID:  $N = N_{pass}/p_{FR}$ , so  $N_{pass} = N_{pass}/p_{FR} - N_{fail}$ , and  $N_{pass} = N_{fail} \times p_{FR}/(1 - p_{FR})$ .

<sup>2</sup>Electron passing the high energy electron selection (HEEP) summarized in Section 6.3.

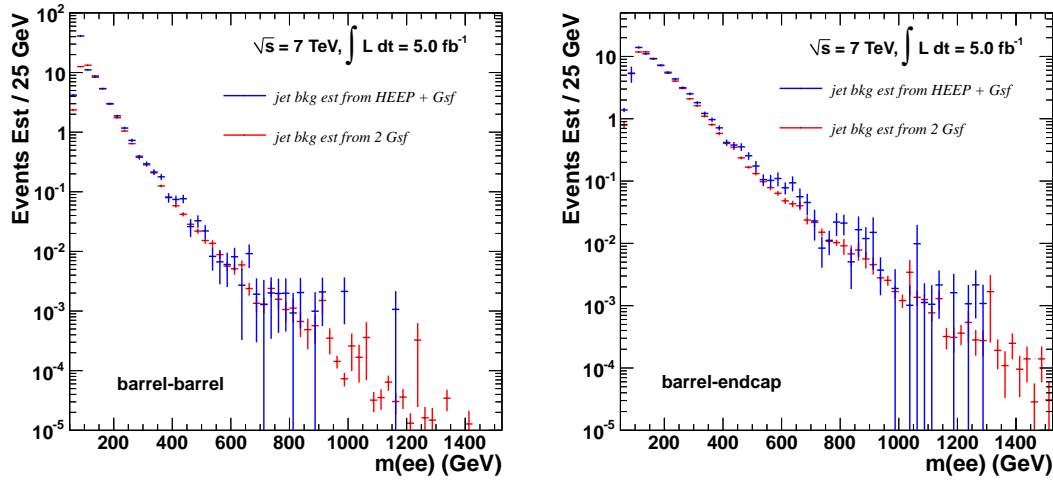


Figure 8.16: Comparison of the two jet background estimation methods. Using a sample of a HEEP electron and a preselected GSF<sup>1</sup> electron (blue), and a sample of two preselected GSF electrons (red), with both electrons in barrel (left), and with one electron in barrel and one in the endcap (right).

jet background estimation method can be assigned [94]. As the contribution of jet backgrounds to the dielectron mass spectrum is under 3 %, this results in only a  $\sim 1\%$  uncertainty on the total background estimation.

---

<sup>1</sup>It is sometimes convenient to use “GSF electron” or “GSF” notation, which refers to a reconstructed electron, GSF stands for the track reconstruction method used for electron reconstruction described in Chapter 5. In particular it is convenient to use these in the context where several electrons are discussed, such as HEEP electron, which refers to an electron passing the HEEP selection.

## 8.6 Results

In Section 8.3, we studied the performance of the electron selection in the data, and derived the corresponding MC to data scale factors. The electron energy scale was validated using Z decays and a corresponding uncertainty was derived (see Section 8.4). The dielectron mass resolution was measured at the Z peak and a mass-dependent parametrization was derived in Section 8.4. The background contributions from the  $t\bar{t}$  and other backgrounds with prompt electrons were validated using the  $e\mu$  spectrum (see Section 8.5.2). The background contribution from jets was evaluated using the fake-rate method (see Section 8.5.3). The uncertainty on the Drell-Yan backgrounds was estimated in Section 8.5.1.

We are now ready to check how the data compares to the Standard Model MC prediction, and perform a search for heavy narrow resonances.

### 8.6.1 Dielectron mass spectrum

Figure 8.17 shows the dielectron mass spectrum obtained from the data, together with the estimated Standard Model backgrounds. These events are obtained following the electron selection described in Section 8.1.

The Drell-Yan,  $t\bar{t}$  and other backgrounds with prompt electrons are estimated from the Monte Carlo simulation. Backgrounds with jets misidentified as electrons are estimated directly from the data using the “fake rate” method. The additional contributions from the  $W \rightarrow e\nu + \text{jet}$  and  $\gamma + \text{jet}$  backgrounds are estimated by applying the  $\text{jet} \rightarrow e$  fake rate probabilities to MC simulated events.

Backgrounds derived from simulation are normalized to each other according to the predicted cross section for each process. The global background normalization is obtained by using the number of events observed in the data within a mass window of 60 – 120 GeV around the Z resonance peak.

Figure 8.18 shows the cumulative invariant mass distribution for the data and the simulation, where the value of each bin is equal to the number of events having that mass or greater.

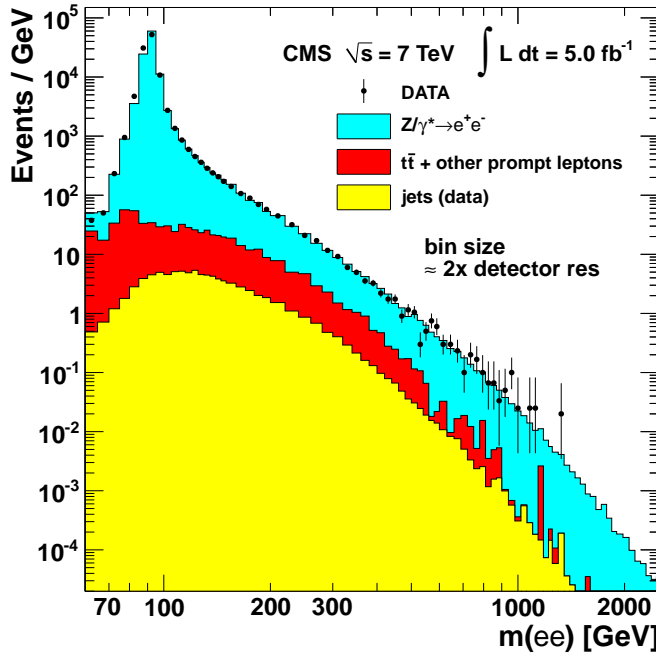


Figure 8.17: The invariant mass spectrum of  $ee$  events. The points with error bars represent the data. The uncertainties in the data points are statistical only. The histograms represent the expectations from SM processes:  $Z'/\gamma^*$ ,  $t\bar{t}$  and other sources of prompt leptons ( $tW$ , diboson production,  $Z \rightarrow \tau\tau$ ), and the multijet backgrounds. Multijet backgrounds contain at least one jet that has been misidentified and reconstructed as a lepton.

The expected yields in the control region (120–200 GeV) and in the high invariant mass region (above 200 GeV) are listed in Table 8.8. The observed data yields agree well with the background expectation. The highest invariant mass event has  $M_{ee} = 1309$  GeV.

No obvious signs of possible new physics are observed. In the following sections we describe the statistical interpretation of the observed invariant mass spectrum.

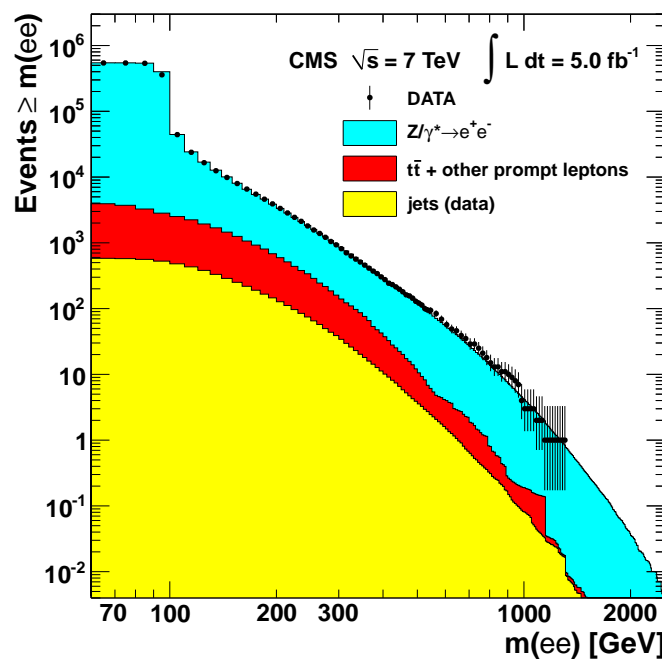


Figure 8.18: The cumulative distribution of the dielectron invariant mass spectrum. The points with error bars represent the data; the histograms represent the background expectations from SM processes. The value of each bin is equal to the number of events having that mass or greater.

Source	Number of events	
	(120 – 200) GeV	> 200 GeV
Data	13207	3335
Total background	$13286 \pm 625$	$3209 \pm 276$
$Z/\gamma^*$	$11945 \pm 597$	$2615 \pm 262$
$t\bar{t}$ + other prompt leptons	$1087 \pm 163$	$467 \pm 70$
Jets	$254 \pm 102$	$127 \pm 51$

Table 8.8: The number of dilepton events with an invariant mass in the control region  $120 < m_{ee} < 200$  GeV and in the search region  $m_{ee} > 200$  GeV. The total background is the sum of the events for the SM processes listed. The quoted uncertainties include both the statistical and systematic errors, added in quadrature.

### 8.6.2 Signal and background parametrization

In order to interpret the observed mass spectrum, we parametrize both the signal and background spectra as analytical functions of mass. These functional forms will be used as probability density functions (p.d.f.) in the construction of the extended likelihood function (see Section 8.6.3).

To describe the signal, we use a convolution of Gaussian and Breit-Wigner functions. The width of the Breit-Wigner function  $\Gamma_{BW}$  models the new resonance width and the width of the Gaussian function  $\sigma_G$  represents the smearing of the reconstructed invariant mass peak due to finite detector resolution:

$$f_S(m|M, \Gamma_{BW}, \sigma_G) = BW(m|M, \Gamma_{BW}) \otimes Gauss(m|\sigma_G). \quad (8.2)$$

The fit of the Breit-Wigner function to the  $Z'$  resonance mass distribution at the generator level is shown in Figure 8.19 for the  $Z'_{SSM}$  and  $Z'_{\Psi}$  models. The fit is performed for several mass points, and a linear parametrization of the  $\Gamma_{BW}$  is also extracted. The width of the Gaussian function is estimated from Monte Carlo simulation, and is corrected by the factor derived from the data in the  $Z$  peak region, as described in Section 8.4.

To describe the background in the region above 200 GeV, the following function is used:

$$f_B(m|A, \alpha, \beta) = A e^{\alpha \cdot m} m^\beta \quad (8.3)$$

where the parameters  $\alpha$  and  $\beta$  have been determined from a fit to the background invariant mass spectrum derived from simulation. The result of this fit is shown in Figure 8.20. This functional form describes well the behavior of the background in a wide mass region. Figure 8.21 shows that the observed dielectron spectrum agrees well with this fit.

$\epsilon(m)$ , defined as the overall signal kinematic acceptance times the efficiency of electron reconstruction and identification as estimated from Monte Carlo simulation,

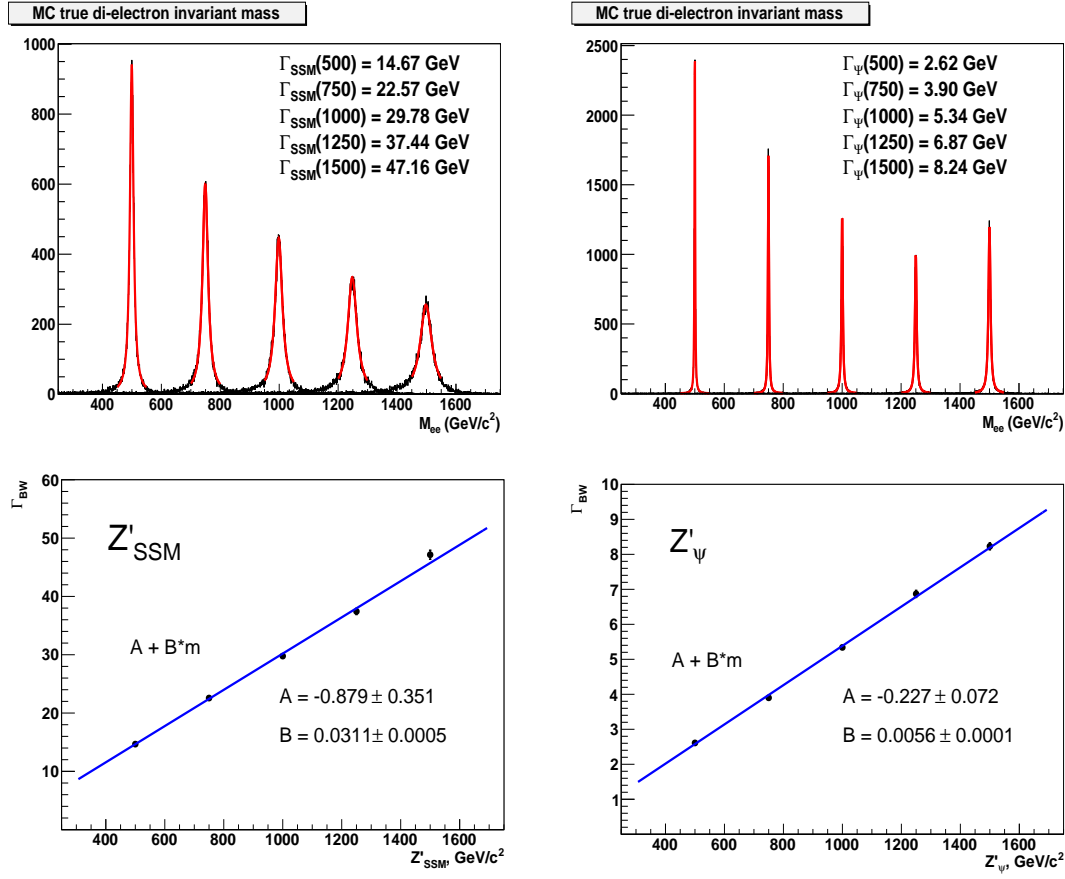


Figure 8.19: (Top) Results of Breit-Wigner function fit to the true MC invariant mass distribution for several mass points for the  $Z'_{SSM}$  and  $Z'_{\Psi}$  models. (Bottom) results of the linear parametrization of  $\Gamma_{BW}$  as a function of mass.

is shown in Figure 8.22. A simple parametrization of  $\epsilon(m)$  is performed, according to the formula:

$$\epsilon(m) = A + \frac{B}{m + C}. \quad (8.4)$$

The electron identification and reconstruction efficiency is corrected by the MC to data scale factor derived in Section 8.3, when it is used for data interpretation in Section 8.6.3.

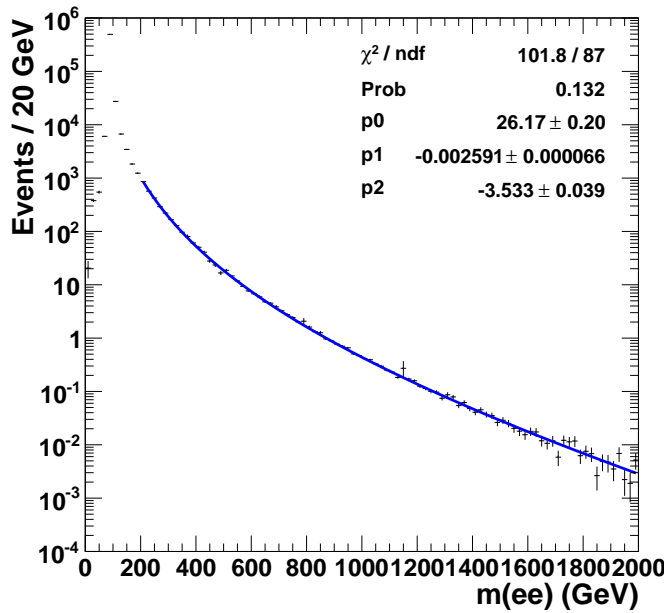


Figure 8.20: The background parametrization. The fit is performed to the invariant-mass spectrum from all background sources.

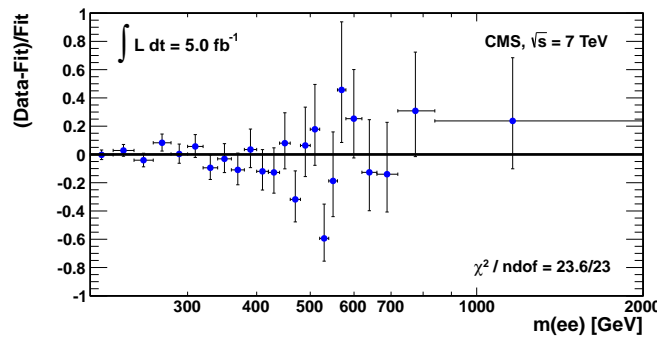


Figure 8.21: The relative difference between the data and the fitted parametrization of the simulated background, where the latter is normalized to the data. The binning is chosen such that each bin has a prediction of at least 10 events, with a minimum bin size of 20 GeV.

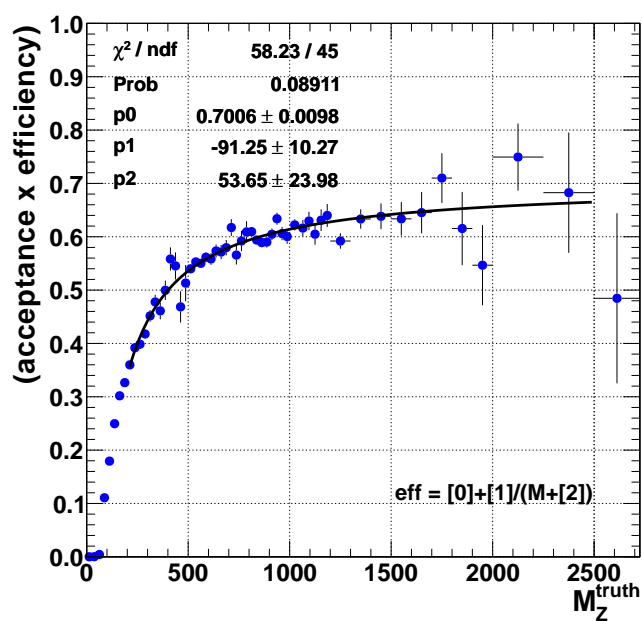


Figure 8.22:  $\epsilon(m)$ , the kinematic acceptance times electron reconstruction and identification efficiency, parametrized as a function of the dielectron invariant mass.

### 8.6.3 Statistical interpretation

The observed invariant mass spectrum agrees well with the Standard Model background prediction. To set limits on the possible contributions from new narrow heavy resonances, we use as a parameter of interest the ratio  $R_\sigma$  of the production yield of  $Z'$  to that of  $Z$ :

$$R_\sigma = \frac{\sigma(pp \rightarrow Z' + X \rightarrow ee + X)}{\sigma(pp \rightarrow Z + X \rightarrow ee + X)}. \quad (8.5)$$

By using the ratio  $R_\sigma$ , we eliminate the uncertainty on the integrated luminosity, and reduce the dependence on the experimental acceptance, trigger, and offline efficiencies. This also provides us with a convenient form for future interpretation of search results in a wide range of theoretical models.

We construct an extended unbinned likelihood function (Eq. 8.6) for the dielectron invariant mass spectrum above 200 GeV, using a sum of analytic probability density functions (pdfs) for the signal and background shapes discussed in Section 8.6.2:

$$\begin{aligned} \mathcal{L}(\mathbf{m}|R_\sigma, M, \Gamma_{BW}, \sigma_G, \alpha, \beta, \mu_B) = & \frac{\mu^N e^{-\mu}}{N!} \prod_{i=1}^N \left( \frac{\mu_S(R_\sigma)}{\mu} f_S(m_i|M, \Gamma_{BW}, \sigma_G) \right. \\ & \left. + \frac{\mu_B}{\mu} f_B(m_i|\alpha, \beta) \right), \end{aligned} \quad (8.6)$$

where  $\mathbf{m}$  denotes the data set in which the observables are the invariant mass values of the electron pairs,  $m_i$ ;  $N$  is the total number of events observed above 200 GeV,  $\mu_S$  and  $\mu_B$  are the Poisson means for signal and the background event yields, and  $\mu = \mu_S + \mu_B$  is Poisson mean for the total event yield.

The width  $\Gamma_{BW}$  is conservatively taken to be that of the  $Z'_{SSM}$ , which has the largest width of the resonances considered, namely 3.1 %.

The Poisson mean of the signal event yield is parametrized as follows  $\mu_S = R_\sigma \cdot \mu_Z \cdot R_\epsilon$ , where  $R_\epsilon$  is the ratio of the kinematic acceptance times the selection efficiency for a  $Z'$  signal to that of the  $Z$ , and  $\mu_Z$  is the Poisson mean of the number of  $Z \rightarrow ee$  events in the  $Z$  peak mass region (60–120 GeV). We estimate  $\mu_Z$  by the number of

observed events in the 60–120 GeV mass window, corrected for a small background contamination ( $\sim 0.4\%$ ).

The ratio  $R_\epsilon$  is estimated from the Monte Carlo simulation, using the parametrization of the acceptance and efficiency shown in Section 8.6.2 for the signal, normalized to the acceptance and efficiency in the Z peak region (60–120 GeV) which is estimated to be 0.109. To correct for the difference between the Monte Carlo and data, a scale factor of 0.992 is applied to this ratio, as discussed in Section 8.3.

The upper limit on the ratio  $R_\sigma$  of the cross section times branching fraction of a Z' boson relative to that for a Z boson was found using the Bayesian technique. The 95 % credible interval is obtained by finding the value  $R_\sigma^{95}$  for which:

$$0.95 = \int_0^{R_\sigma^{95}} p(R_\sigma | \mathbf{m}) dR_\sigma \quad (8.7)$$

where  $p(R_\sigma | \mathbf{m})$  is the posterior pdf, obtained using Bayes's theorem (the likelihood function is multiplied by the prior pdfs, and the nuisance parameters are integrated out), with a uniform prior for  $R_\sigma$ . The integration is performed using the Markov Chain Monte Carlo technique [117] as implemented in RooStats [118].

The systematic uncertainty on  $R_\epsilon$  is conservatively set to be 8 %, as a result of the uncertainties on the scale factors derived to correct the efficiency estimated from simulation to the data (see Section 8.3). An uncertainty of 1 % on the mass scale (due to the energy scale uncertainty) has been used (see Section 8.4), and a conservative uncertainty of 15 % have been assigned to the estimated number of background events ( $\mu_B$ ), which includes the uncertainties discussed in Section 8.5. Log-normal priors have been used to account for the systematic effects discussed above.

To compute the mass limits for the specific benchmark models discussed in Chapter 2, we compute the ratio  $R_\sigma$  for each signal model as a function of mass. The leading-order cross section predictions for  $Z'_{SSM}$  and  $Z'_{\Psi}$  derived from PYTHIA are corrected by mass dependent k-factors obtained using ZWPRODP [120, 121, 122], to account for the next-to-next-to-leading order (NNLO) corrections. To normalize the Z' cross sections we use the NNLO prediction for the  $Z/\gamma$  production cross section in

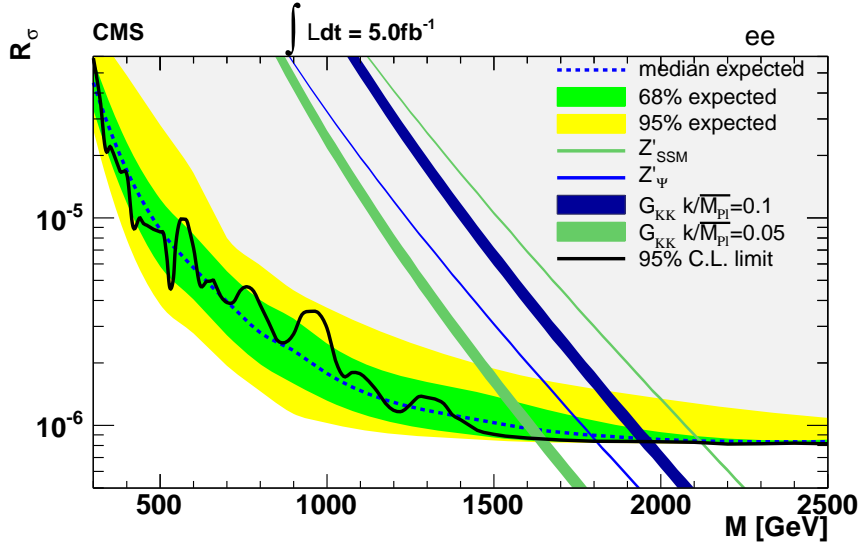


Figure 8.23: Upper limits as a function of the resonance mass  $M$  on the production ratio  $R_\sigma$  of cross section times branching fraction into electron pairs for  $Z'_{SSM}$ ,  $Z'_{\Psi}$ , and  $G_{KK}$  production to the same quantity for  $Z$  bosons. Shaded green and yellow bands correspond to the 68 % and 95 % quantiles for the expected limits. The predicted cross section ratios are shown as bands, with widths indicating the theoretical uncertainties. The differences in the widths reflect the different uncertainties in the  $k$ -factors used.

the mass window 60–120 GeV, of  $0.97 \pm 0.04$  nb [119].

These results can also be interpreted to set limits on possible Kaluza-Klein graviton ( $G_{KK}$ ) excitations arising in the Randall-Sundrum model of extra dimensions [125, 126]. The acceptance for  $G_{KK}$  resonances is higher than that for the  $Z'$ , by less than 8 % over the mass range 0.75 – 2.0 TeV. This difference in acceptance is conservatively neglected when calculating the corresponding limits. The leading-order cross section predicted by PYTHIA is corrected by a constant next-to-leading order  $k$ -factor of 1.6 [123].

Figure 8.23 shows the upper limit on the ratio  $R_\sigma$  as a function of the resonance mass, together with the  $R_\sigma$  curves for the  $Z'_{SSM}$ ,  $Z'_{\Psi}$  and for  $G_{KK}$  with couplings 0.10 and 0.05. The uncertainties on the  $k$ -factors are included as the bands on the  $R_\sigma$  curves (1 – 3 % on the  $Z'$  and 10 % for  $G_{KK}$ ) [124].

At 95 % C.L. the production of  $Z'_{SSM}$  and  $Z'_{\Psi}$  resonances are excluded for masses

below 2120 and 1810 GeV, respectively. The corresponding lower limits on the mass for  $G_{KK}$  resonances with couplings of 0.10 (0.05) are 1940 (1640) GeV.

The largest deviation from SM expectations at high masses occurs at 960 GeV, with a local significance of  $\mathcal{Z} = 1.7$ , where  $\mathcal{Z}$  is the number of Gaussian standard deviations in a one-sided test. The probability to observe an enhancement at least as large as the one found, occurring anywhere between 600 and 2500 GeV, was found to be 38 %.

#### 8.6.4 Combination with the dimuon channel

A similar analysis searching for heavy neutral resonances in the dimuon final state was performed in CMS by the high momentum muon group [112]. The search was performed on a slightly larger data set with respect to the dielectron analysis due to less stringent requirements on the CMS subsystems' availability. The dimuon data set corresponds to an integrated luminosity of  $5.3 \text{ fb}^{-1}$ . Below I summarize the results of the combination of the dimuon and dielectron analyses [112, 94, 114].

Figure 8.24 shows the upper limit on the ratio  $R_\sigma$  as a function of the resonance mass for the combination of dielectron and dimuon channels [114]. The 95 % CL lower limits on the mass of a heavy neutral dilepton resonance are 2330 GeV for  $Z'_{SSM}$ , 2000 GeV for  $Z'_\psi$ , and 890 (540) GeV for  $Z'_{St}$  with  $\epsilon = 0.06$  (0.04). The RS Kaluza-Klein gravitons are excluded below 2140 (1810) GeV, for couplings of 0.10 (0.05).

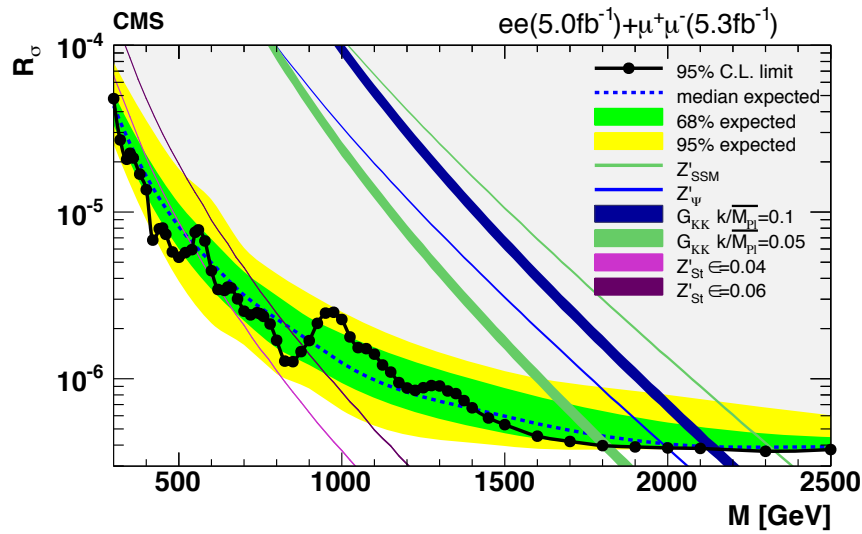


Figure 8.24: Upper limits as a function of the resonance mass  $M$  on the production ratio  $R_\sigma$  of cross section times branching fraction into lepton pairs for  $Z'_{SSM}$ ,  $Z'_{\Psi}$ ,  $Z'_{St}$ , and  $G_{KK}$  production to the same quantity for  $Z$  bosons. Shaded green and yellow bands correspond to the 68 % and 95 % quantiles for the expected limits. The predicted cross section ratios are shown as bands, with widths indicating the theoretical uncertainties. The differences in the widths reflect the different uncertainties in the  $k$ -factors used.



# Chapter 9

## Conclusion

### 9.1 Summary

A search for dielectron decays of heavy neutral resonances has been performed using proton-proton collision data collected at  $\sqrt{s} = 7$  TeV by the CMS experiment at the LHC in 2011. The data sample corresponds to an integrated luminosity of  $5 \text{ fb}^{-1}$ . The dielectron mass distribution is consistent with Standard Model predictions. An upper limit on the ratio of the cross section times branching fraction of new bosons, normalized to the cross section times branching fraction of the Z boson, is set at the 95 % confidence level. This result is translated into limits on the mass of new neutral particles at the level of 2120 GeV for the  $Z'$  in the Sequential Standard Model, 1810 GeV for the superstring-inspired  $Z'_{\psi}$  resonance, and 1940 (1640) GeV for RS Kaluza-Klein gravitons with the coupling parameter  $k/M_{Pl}$  of 0.10 (0.05).

In combination with the dimuon channel [114], 95 % CL lower limits on the mass of a heavy neutral dilepton resonance are set at 2330 GeV for  $Z'_{SSM}$ , 2000 GeV for  $Z'_{\psi}$ , and 890 (540) GeV for  $Z'_{St}$  with  $\epsilon = 0.06$  (0.04). The RS Kaluza-Klein gravitons are excluded below 2140 (1810) GeV, for couplings of 0.10 (0.05).

### 9.2 Current status and outlook

The search for heavy neutral resonances in both the dielectron and dimuon final states was updated with the 2012 data set, corresponding to an integrated luminosity of  $20 \text{ fb}^{-1}$  collected at  $\sqrt{s} = 8$  TeV [127].

In the updated dielectron analysis the electron identification was slightly modified [128] to address the increase of the pile up background. In addition, the search was performed separately for events having both electrons in the barrel and events where one electron in in the barrel and one in the endcap, due to the difference in resolution and signal to background ratio.

The final dielectron and dimuon mass spectra are presented in Figure 9.1 [127]. The data are found to be in agreement with the Standard Model predictions, and limits are set on the possible contribution of heavy narrow resonances.

Upper limits on the ratio of the cross section times the branching fraction of a new boson to that of the Z boson for the combination of the electron and muon channels are presented in Figures 9.2. A Sequential Standard Model  $Z'_{SSM}$  was excluded for masses less than 2960 GeV , and a superstring-inspired  $Z'_{\psi}$  less than 2600 GeV was excluded at the 95 % confidence level [127].

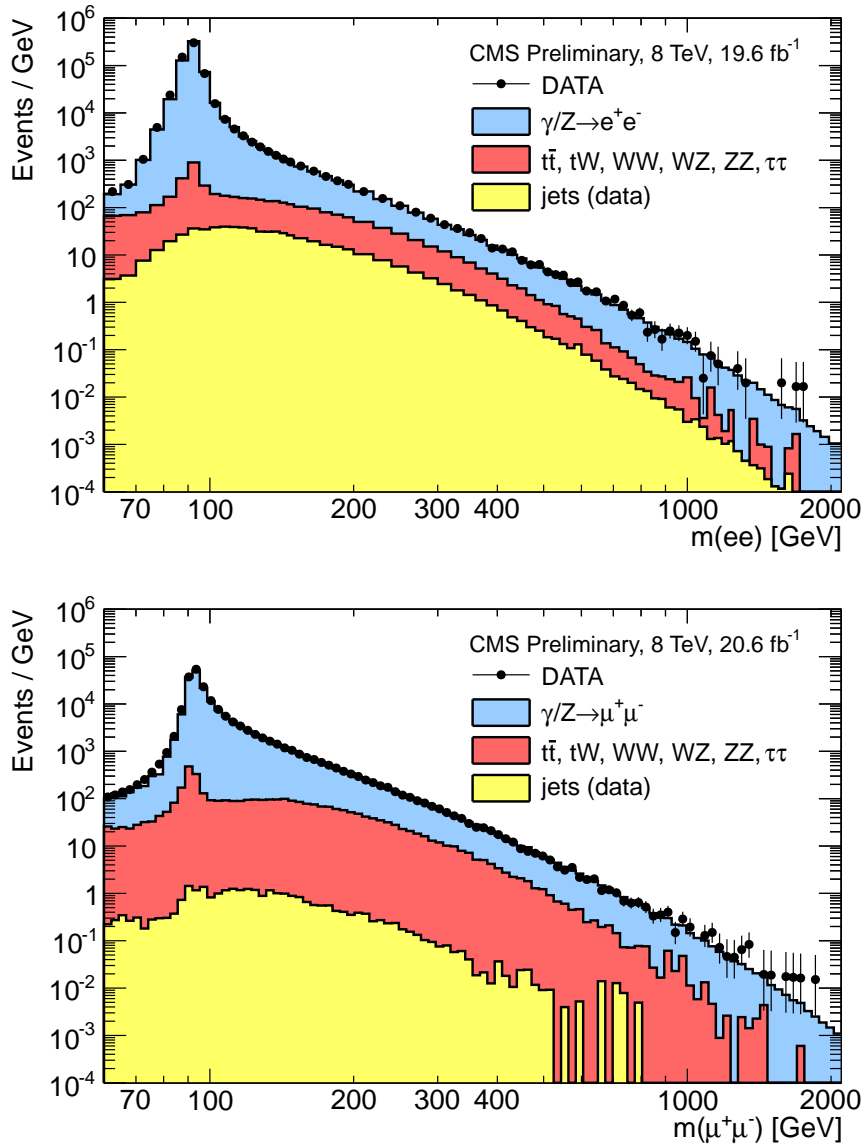


Figure 9.1: The invariant mass spectra of  $ee$  (top) and  $\mu^+\mu^-$  (bottom) events. The points with error bars represent the data. The histograms represent the expectations from standard model processes:  $Z/\gamma$ ,  $t\bar{t}$  and other sources of prompt leptons ( $tW$ , diboson production,  $Z \rightarrow \tau\tau$ ), and the multi-jet backgrounds. Multi-jet backgrounds contain at least one jet that has been misreconstructed as a lepton. The Monte Carlo simulated backgrounds are normalised to the data in the region of  $60 < m < 120 \text{ GeV}$ .

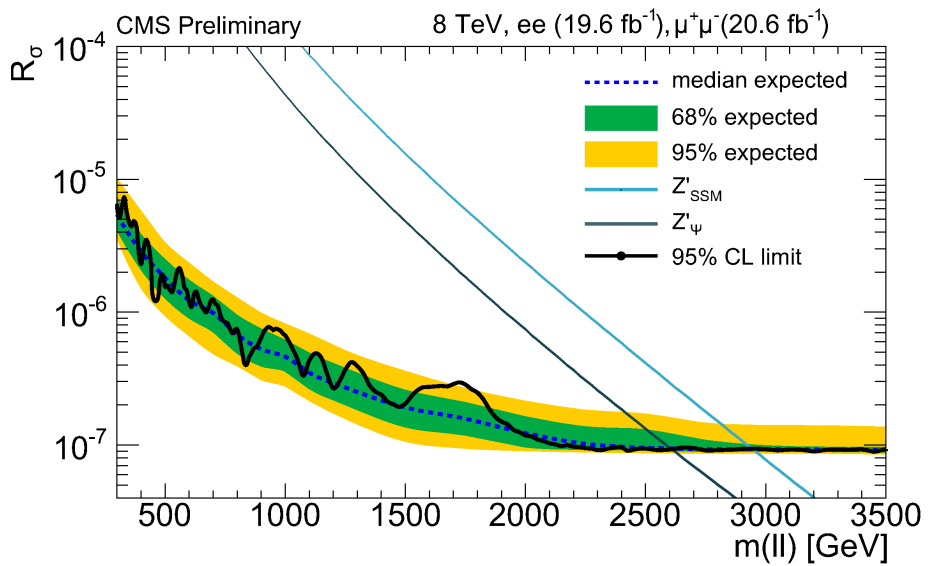


Figure 9.2: Upper limits as a function of resonance mass on the production ratio  $R_\sigma$  of cross section times branching fraction into lepton pairs for  $Z'_{SSM}$  and  $Z'_{\psi}$  boson production to the same quantity for  $Z$  bosons. The limits are shown for the combination of dielectron and dimuon final states. Shaded green and yellow bands correspond to the 68 % and 95 % quantiles for the expected limits.

# Bibliography

- [1] S.L. Glashow, Nucl. Phys. **22** (1961) 579;  
 S. Weinberg, Phys. Rev. Lett. **19** (1967) 1264;  
 A. Salam, *Elementary Particle Theory*, Ed. N. Svartholm *et al.*, 367 (Almqvist and Wiksell, Stockholm, 1968);  
 S.L. Glashow, J. Iliopoulos and L. Maiani, Phys. Rev. **D 2** (1970) 1285.
  
- [2] M. Gell-Mann, Phys. Lett. **8** (1964) 214;  
 G. Zweig, CERN-Report 8182/TH401 (1964);  
 H. Fritzsch, M. Gell-Mann and H. Leutwyler, Phys. Lett. **B 47** (1973) 365;  
 D. Gross and F. Wilczek, Phys. Rev. Lett. **30** (1973) 1343;  
 H.D. Politzer, Phys. Rev. Lett. **30** (1973) 1346;  
 G. t Hooft, Marseille Conference on YangMills elds (1972).
  
- [3] P.A.M. Dirac, Proc. Roy. Soc. Lond. **A 114** (1927) 243;  
 P. Jordan and W. Pauli, Z. Phys. **47** (1928) 151;  
 W. Heisenberg and W. Pauli, Z. Phys. **56** (1929) 1;  
 S. Tomonaga, Progr. Theor. Phys. **1** (1946) 27;  
 J. Schwinger, Phys. Rev. **73** (1948) 416;  
 R. Feynman, Phys. Rev. **76** (1949) 749.
  
- [4] E. Fermi, Nuovo Cim. **11** (1934) 1;  
*ibid.* Z. Phys. **88** (1934) 161;  
 R. Feynman and M. Gell-Mann, Phys. Rev. **109** (1958) 193.
  
- [5] G. t Hooft, Nucl. Phys. **B 33** (1971) 173;  
*ibid.* Nucl. Phys. **B 35** (1971) 167;  
 G. t Hooft and M. Veltman, Nucl. Phys. **B 44** (1972) 189.

- [6] H.D. Politzer, *Reliable Perturbative Results for Strong Interactions?*, Phys. Rev. Lett. **30** (1973) 1346;  
 D.J. Gross and F. Wilczek, *Ultraviolet Behavior of Non-Abelian Gauge Theories*, Phys. Rev. Lett. **30** (1973) 1343.
- [7] F. Englert, R. Brout, Phys. Rev. Lett. **13** (1964) 321;  
 P.W. Higgs, Phys. Lett. **12** (1964) 132;  
 P.W. Higgs, Phys. Rev. Lett. **13** (1964) 508;  
 G.S. Guralnik, C.R. Hagen, T.W.B. Kibble, Phys. Rev. Lett. **13** (1964) 585;  
 P.W. Higgs, Phys. Rev. **145** (1966) 1156;  
 T.W.B. Kibble, Phys. Rev. **155** (1967) 1554.
- [8] J. Beringer *et al.*(Particle Data Group), *Review of Particle Physics*, Phys. Rev. **D 86** (2012) 010001.
- [9] ALEPH, DELPHI, L3, OPAL Collaborations and the LEP Electronweak Working Group, *A Combination of Preliminary Electroweak Measurements and Constraints on the Standard Model*, CERN-PH-EP/2006-042, hep-ex/0612034.
- [10] ATLAS Collaboration, *Observation of a new particle in the search for the Standard Model Higgs boson with the ATLAS detector at the LHC*, Phys. Lett. **B 716** (2012) 1-29.
- [11] CMS Collaboration, *Observation of a new boson at a mass of 125 GeV with the CMS experiment at the LHC*, Phys. Lett. **B 716** (2012) 29-61.
- [12] W. Marciano, in: Proc. APS Division of Particles and Fields Meeting (Salt Lake City, UT, January 1987), eds C. DeTar and J.S. Ball (World Scientific, Singapore, 1987);  
 H. Georgi, H. Quinn and S. Weinberg, Phys. Rev. Lett. **33** (1974) 451.

- [13] Michael Dine, *Supersymmetry and String Theory*, Cambridge University Press, (2007).
- [14] J. L. Hewett and T. G. Rizzo, Phys. Rep. **183** (1989) 193.
- [15] J. L. Rosner, Comments Nucl. Part. Phys. **15** (1986) 195.
- [16] D. London and J.L. Rosner, Phys. Rev. **D 34** (1986) 1530;  
P. Langacker, R.W. Robinett and J.L. Rosner, Phys. Rev. **D 30** (1984) 1470.
- [17] Paul Langacker, Rev. Mod. Phys. **81** (2009) 1199.
- [18] M. Cvetic and S. Godfrey in T. Barklow (ed.) *Electroweak Symmetry Breaking and Physics Beyond the Standard Model*, World Scientific, (1995) 383, [hep-ph/9504216].
- [19] B. Kors and P. Nath, *A Stueckelberg extension of the standard model*, Phys. Lett. **B 586** (2004) 366.
- [20] B. Kors and P. Nath, *Aspects of the Stueckelberg extension*, JHEP **0507** (2005) 069.
- [21] E. C. G. Stueckelberg, Helv. Phys. Acta **11** (1938) 225.
- [22] V. I. Ogievetskii and I. V. Polubarinov, Sov. Phys. JETP **14** (1962) 179.
- [23] D. Feldman, Z. Lium and P. Nath, *Probing a very narrow Z' boson with CDF and D0 Data*, Phys. Rev. Lett. **97** (2006) 021801.
- [24] L. Randall and R. Sundrum, *An alternative to compactification*, Phys. Rev. Lett. **83** (1999) 4690;  
L. Randall and R. Sundrum, *A large mass hierarchy from a small extra dimension*, Phys. Rev. Lett. **83** (1999) 3370.
- [25] H. Davoudiasl, J. L. Hewett and T. G. Rizzo, *Phenomenology of the Randall-Sundrum Gauge Hierarchy Model*, Phis. Rev. Lett. **84** (2000) 2080.

- [26] D0 Collaboration, V. Abazov *et al.*, Nucl. Instrum. Meth. **A 565** (2006) 463; CDF Collaboration, F. Abe *et al.*, Nucl. Instrum. Meth. **A 271** (1988) 487.
- [27] ALEPH Collaboration, D. Decamp *et al.*, Nucl. Instrum. Meth. **A 294** (1990) 121-178; DELPHI Collaboration, P. Aarnio *et al.*, Nucl. Instrum. Meth. **A 303** (1991) 233-276; L3 Collaboration, B. Adeva *et al.*, Nucl. Instrum. Meth. **A 289** (1990) 35-102; OPAL Collaboration, K. Ahmet *et al.*, Nucl. Instrum. Meth. **A 305** (1991) 275-319.
- [28] J. Alcaraz *et al.* [ALEPH, DELPHI, L3, OPAL Collabs., LEP Electroweak Working Group], *A Combination pf Preliminary Electroweak Measurements and Constraints on the Standard Model*, CERN-PH-EP/2006-042, hep-ex/0612034.
- [29] The D0 Collaboration, *Search for a heavy neutral gauge boson in the dielectron channel with 5.4 fb-1 of ppbar collisions at sqrt(s) = 1.96 TeV*, Phys. Lett. **B 695** (2011) 88.
- [30] The CDF Collaboration, *Search for High-Mass  $e^+e^-$  Resonances in pp̄ Collisions at  $\sqrt{s} = 1.96$  TeV* Phys. Rev. Lett. **102** (2009) 031801.
- [31] G. K. Wilson, *Confinement of quarks*, Phys. Rev. **D 10** (1974) 2445-2459.
- [32] Lyndon Evans and Philip Bryant, *The CERN Large Hadron Collider: Accelerator and Experiments*, JINST **3** (2008) S08001.
- [33] The LEP collaboration, *LEP design report. v.2 : The LEP main ring*, CERN-LEP-84-01 (1984).
- [34] J. P. Blewett, *200 GeV intersecting storage accelerators*, Proc. 8-th Int. Conf. on High-Energy Accelerators, CERN, Geneva, Switzerland (1971).
- [35] Christiane Lefèvre, *The CERN accelerator complex. Complexe des accélérateurs du CERN*, Dec 2008, URL: <https://cdsweb.cern.ch/record/1260465>.

- [36] Christiane Lefèvre, *LHC: the guide (English version). Guide du LHC (version anglaise)*, CERN-Brochure-2009-003-Eng, Feb 2009,  
URL: <http://cds.cern.ch/record/1165534>.
- [37] M. Bajko *et al.*, *Report of the Task Force on the Incident of 19th September 2008 at the LHC*, CERN-LHC-PROJECT-Report-1168, CERN, Geneva (2009).
- [38] The ATLAS Collaboration, *ATLAS: detector and physics performance technical design report. Volume 1*, CERN-LHCC-99-14, ATLAS-TDR-14 (1999);  
The ATLAS Collaboration, *ATLAS: detector and physics performance technical design report. Volume 2*, CERN-LHCC-99-15, ATLAS-TDR-15 (1999);  
The ATLAS Collaboration, *The ATLAS experiment at the CERN Large Hadron Collider*, JINST **3** (2008) S08003.
- [39] The CMS Collaboration, *CMS Physics TDR, Volume I*, CERN-LHCC-2006-001 (2006);  
The CMS Collaboration, *The CMS experiment at the CERN LHC*, JINST **3** (2008) S08004.
- [40] The ALICE collaboration, *ALICE : Technical proposal for a Large Ion collider Experiment at the CERN LHC*, CERN-LHCC-95-71 (2005);  
The ALICE collaboration, *The ALICE experiment at the CERN LHC*, JINST **3** (2008) S08002.
- [41] The LHCb Collaboration, *LHCb : Technical Proposal*, CERN-LHCC-98-004 (1998);  
The LHCb Collaboration, *The LHCb Detector at the LHC*, JINST **3** (2008) S08005.
- [42] The LHC Programme Coordination, *LHC Luminosity Plots for the 2011 Proton Run*, (2012), URL: [http://lpc.web.cern.ch/lpc/lumiplots\\_2011.htm](http://lpc.web.cern.ch/lpc/lumiplots_2011.htm).

- [43] The CMS Collaboration, *CMS Luminosity - Public Results, 2011 Proton-Proton Collisions*, February 2013,  
URL: <https://twiki.cern.ch/twiki/bin/view/CMSPublic/LumiPublicResults>.
- [44] The CMS Collaboration, *The CMS experiment at the CERN LHC*, JINST **3** (2008) S08004.
- [45] David Barney, *CMS Slice (2004 version)*, IPPOG Document 12-v1,  
URL: <https://cms-docdb.cern.ch/cgi-bin/PublicEPPOGDocDB>ShowDocument?docid=12>.
- [46] The CMS collaboration, *The CMS tracker system project: technical design report*, CERN-LHCC-98-006 (1998).
- [47] The CMS collaboration, *The CMS tracker: addendum to the technical design report*, CERN-LHCC-2000-016 (2000).
- [48] The CMS Collaboration, *The Electromagnetic Calorimeter Technical Design Report*, CERN/LHCC (1997) 97-33.
- [49] M. Kobayashi *et al.*, *Improvement of radiation hardness of PbW<sub>0</sub><sub>4</sub> scintillating crystals by La-doping*, Nucl. Instrum. Meth. **A 404** (1998) 149;  
M. Kabayashi *et al.*, *Significant improvement of PbW<sub>0</sub><sub>4</sub> scintillating crystals by doping with trivalent ions*, Nucl. Instrum. Meth. **A 434** (1999) 412.
- [50] A.A. Annenkov, M.V. Korzhik and P. Locoq, *Lead tungstate scintillation material*, Nucl. Instrum. Meth. **A 490** (2002) 30.
- [51] P. Adzic *et al.*, *Energy resolution of the barrel of the CMS Electromagnetic Calorimeter*, Journal of Instrumentation (JINST) **2** (2007) P04004.
- [52] The CMS Collaboration, *The CMS Hadron Calorimeter Project: Technical Design Report, volume 2 of Technical Design Report CMS*, CERN, Geneva, June 1997; CERN-LHCC-97-031; CMS-TDR-002.

- [53] P. Cushman, A. Heering and A. Ronzhin, *Custom HPD readout for the CMS HCAL*, Nucl. Instrum. Meth. **A 442** (2000) 289.
- [54] D. Baden et al., *HCAL Partition Definitions*, CMS Note IN-2005-027 (2005).
- [55] The CMS HCAL and ECAL Collaboration, *The CMS barrel calorimeter response to particle beams from 2 to 350 GeV/c*, Eur. Phys. J., vol. **C 60** (2009) 359-373.
- [56] P. A. Cherenkov, *Visible emission of clean liquids by action of gamma radiation*, Doklady Akademii Nauk SSSR, **Vol. 2** (1934) 451.
- [57] The CMS HCAL Collaboration, *Design, performance and calibration of the CMS forward calorimeter wedges*, Eur. Phys. J., vol **C 53** (2008) 139-166.
- [58] The CMS Collaboration, *The CMS muon project: Technical Design Report, volume 3 of Technical Design Report CMS*, CERN, Geneva, December 1997, CERN-LHCC-97-032; CMS-TDR-003.
- [59] X.D. Qu, L.Y. Zhang and R.Y. Zhu, *Radiation Induced Color Centers and Light Monitoring for Lead Tungstate Crystals*, Proc. IEEE Trans. Nucl. Sci. vol **47** no. 6 (2000) 1741-47.
- [60] R.-Y. Zhu, *Radiation Damage in Scintillating Crystals*, Nucl. Instr. and Meth. **A 413** (1998) 297-311.
- [61] M. Huhtinen, P. Lecomte, D. Luckey, F. Nessi-Tedaldi, F. Pauss, *High-energy proton induced damage in PbWO<sub>4</sub> calorimeter crystals*, Nucl. Instr. and Meth. **A 545** (2005) 63-87.
- [62] M. Anfrevilleb et al., *Laser monitoring system for the CMS lead tungstate crystal calorimeters*, CMS NOTE-2007-028 (2008).
- [63] V. Timciuc, *Database usage in the CMS ECAL laser monitoring system*, J. Phys.: Conf. Ser. **219** (2010) 022045.

- [64] P. Bonamy *et al.*, *The ECAL Calibration: Use of the Light Monitoring System. Version 2.0* CMS NOTE-1998-013 (1998).
- [65] CMS Collaboration, *Electron and photon energy calibration and resolution with the CMS ECAL at  $\sqrt{s} = 7$  TeV*, CMS Physics Analysis Summary EGM-11-001 (2013).
- [66] Keijun Zhu (for ECAL CMS Group), *The CMS ECAL Laser Monitoring System*, Proc.IEEE Nucl. Sci. Symp. vol. **1** (2007) 153-158.
- [67] Quantronix, 41 Research Way, East Setauket, NY 11733, USA,  
<http://www.quantronixlasers.com>.
- [68] L.Y. Zhang, K.J. Zhu, R.Y. Zhu and D. Liu, *Monitoring Light Source for CMS Lead Tungstate Crystal Calorimeter at LHC* , Proc. IEEE Trans. Nucl. Sci. vol. **48** no. 3 (2001) 372-8.
- [69] Photonics Industries, 390 Central Avenue, Bohemia, NY 11716, USA,  
<http://www.photonix.com>.
- [70] The CMS Collaboration, *The TriDAS Project, Technical Design Report, Volume 2: Data Acquisition and High-Level Trigger*, CERN/LHCC (2002) 2002-36,  
<http://cmsdoc.cern.ch/cms/TDR/DAQ/daq.html>.
- [71] M.De Gruttola *et al.*, *Persistent storage of non-event data in the CMS databases*, JINST **5** (2010) P04003.
- [72] CMS Collaboration, *CMS, The Computing Project, Technical Design Report*, CERN-LHCC-2005-023, (2005) <http://cmsdoc.cern.ch/cms/cpt/tdr/>.
- [73] G. Govi, V. Innocente and Z. Xie, *CMS offline conditions framework and services*, J. Phys.: Conf. Ser. **219** (2010) 042027.
- [74] B. Stroustrup, *The C++ Programming Language*, Addison-Wesley, 1997,  
ISBN 0201327554.

- [75] R. Leyderman, *Oracle C++ Call Interface Programmer's Guide*, (2009) Oracle.
- [76] C.D. Jones *et al.*, *Analysis environments for CMS*, J. Phys. Conf. Ser. **119** (2008) 032027.
- [77] The CMS Collaboration, *ECAL 2010 performance results*, CMS DPS 2011-008 (2011).
- [78] The CMS Collaboration, *CMS ECAL Performance on 2011 data*, CMS DP 2012-002 (2012).
- [79] [http://www.hep.caltech.edu/~zhu/talks/ryz\\_120228\\_laser\\_web.pdf](http://www.hep.caltech.edu/~zhu/talks/ryz_120228_laser_web.pdf).
- [80] CMS Collaboration, *Electron reconstruction and identification at  $\sqrt{s} = 7 \text{ TeV}$* , CMS Physics Analysis Summary EGM-10-004 (2011).
- [81] M. Anderson *et al.*, *Review of clustering algorithms and energy corrections in ECAL*, CMS Note IN-2010-008 (2010).
- [82] W. Adam *et al.*, *Electron Reconstruction in CMS*, CMS Analysis Note AN-2009-164 (2009).
- [83] CMS Collaboration, *Commissioning of the Particle-flow Event Reconstruction with the first LHC collisions recorded in the CMS detector*, CMS Physics Analysis Summary PFT-10-001 (2010).
- [84] W. Adam, R. Fruhwirth, A. Strandlie, T. Todorov, *Reconstruction of electrons with the Gaussian-sum filter in the CMS tracker at the LHC*, J. Phys. G: Nucl. Part. Phys. **31** (2005) N9-N20.
- [85] C. Charlot, C. Rovelli, Y. Sirois, *Reconstruction of Electron Tracks Using Gaussian Sum Filter in CMS*, CMS Analysis Note AN-2005-011 (2006).
- [86] R. Fruhwirth, *Application of Kalman filtering to track and vertex fitting*, Nucl. Instrum. and Methods, **A 262** (1987) 444.

- [87] P. Meridiani and C. Seez, *Definition of calibrated ECAL RecHits and the ECAL calibration and correction scheme*, CMS Note IN-2011-002 (2011).
- [88] CMS Collaboration, *Electromagnetic calorimeter calibration with 7 TeV data*, CMS Physics Analysis Summary EGM-10-003 (2011).
- [89] H. Bethe and W. Heitler, *On the Stopping of Fast Particles and on the Creation of Positive Electrons*, Proc. Roy. Soc. Lond. **A** **146** (1934) 83-112.
- [90] S. Baffoni et al., *Electron Identification in CMS*, CMS Analysis Note AN-2009-178 (2009).
- [91] W. Andrews et al., *Study of photon conversion rejection at CMS*, CMS Analysis Note AN-2009-159 (2010).
- [92] B. LeBourgeois et al., *Improvement in Photon Conversion Rejection Performance Using Advanced Tracking Tools*, CMS Analysis Note AN-2010-283 (2010).
- [93] J. Alcazar-Maestre et al., *Updated Measurements of the Inclusive W and Z Cross Sections at 7 TeV*, CMS Analysis Note AN-2010-264 (2010).
- [94] B. Clerbaux et al., *Search for High-Mass Resonances Decaying to Electron Pairs in the CMS Experiment*, CMS Analysis Note AN-11-444 (2012).
- [95] V. Timciuc et al., *Calibration of the ECAL energy scale using the  $J/\psi$  resonance*, CMS Analysis Note AN-10-443 (2011).
- [96] W. Verkerke, D. Kirkby, *RooFit Users Manual v2.07*.
- [97] V. Ticmiuc et al., *Measurement of the CMS ECAL scale and resolution performance from  $Z \rightarrow ee$  decays and determination of the signal line shape for  $H \rightarrow \gamma\gamma$* , CMS Analysis Note AN-11-204 (2011).
- [98] CMS Collaboration, *Measuring Electron Efficiencies at CMS with Early Data*, CMS Physics Analysis Summary EGM-07-001 (2007).

- [99] L. Thomas, B. Clerbaux and G. De Lentdecker, *High pt Electron selection efficiency measurement with Tag and Probe method*, CMS Analysis Note AN-2011-117 (2011).
- [100] E/Gamma POG, *Electron reconstruction efficiency with 2011 Data*,  
[#Electron\\_reconstruction\\_efficien.](https://twiki.cern.ch/twiki/bin/view/CMS/EgCommissioningAndPhysicsDeliverables?rev=15)
- [101] CMS Collaboration, *Measurements of inclusive W and Z cross sections in pp collisions at  $\sqrt{s} = 7$  TeV*, JHEP 01 (2011) 080, doi:10.1007/JHEP01(2011)080, arXiv:1012.2466.
- [102] Sidney D. Drell and Tung-Mow Yan, *Massive Lepton-Pair Production in Hadron-Hadron Collisions at High Energies*, Phys. Rev. Lett. **25** (1970) 902, doi:10.1103/PhysRevLett.25.316.
- [103] CMS Collaboration, *High PileUp Studies*, CMS DP-2012-005 (2012).
- [104] S. Bafoni *et al.*, *Electron Charge Determination Commissioning from 7 TeV Data*, CMS Analysis Note AN-2010-468 (2010).
- [105] F. Maltoni and T. Stelzer, *MadEvent: Automatic event generation with MadGraph*, JHEP **02** (2003) 027.
- [106] S. Frixione, P. Nason and C. Oleari, *Matching NLO QCD computations with Parton Shower simulations: the POWHEG method*, JHEP **11** (2007) 070.
- [107] T. Sjöstrand , S. Mrenna and P. Skands, *PYTHIA 6.4 physics and manual*, JHEP **05** (2006) 026.
- [108] J. Pumplin *et al.*, *New generation of parton distributions with uncertainties from global QCD analysis*, JHEP **07** (2002) 012.
- [109] GEANT4 Collaboration, *GEANT4-a simulation toolkit*, Nucl. Instrum. Meth. **A 506** (2003) 250.

- [110] O. Charaf *et al.*, *Search for High-Mass Resonances Decaying to Electron Pairs in the CMS Experiment*, CMS Analysis Note AN-2011-159 (2011).
- [111] Nikolaos Kidonakis, *Next-to-next-to-leading soft-gluon corrections for the top quark cross section and transverse momentum distribution*, Phys. Rev. **D 82** (2010) 114030.
- [112] G. Alverson *et al.*, *Search for High-Mass Resonances Decaying to Muon Pairs with Collisions Gathered at  $\sqrt{s} = 7 \text{ TeV}$* , CMS Analysis Note AN-11-472 (2012).
- [113] M. Chen *et al.*, *Search for New High-Mass Resonances Decaying to Muon Pairs in the CMS Experiment*, CMS Analysis Note AN-2007-038 (2007).
- [114] CMS Collaboration, *Search for narrow resonances in dilepton mass spectra in pp collisions at  $\sqrt{s} = 7 \text{ TeV}$* , Phys. Lett. **B 714** (2012) 158-179.
- [115] K. Melnikov and F. Petriello, *Electroweak gauge boson production at hadron colliders through  $O(\alpha_s^2)$* , Phys. Rev. **D 74** (2006) 114017, arXiv:hep-ph/0609070.
- [116] CMS Collaboration, *Performance of CMS muon reconstruction in pp collision events at  $\sqrt{s} = 7 \text{ TeV}$* , CMS Physics Analysis Summary MUO-10-004 (2011).
- [117] W. K. Hastings, *Monte Carlo sampling methods using Markov chain and their applications*, Biometrika **57** (1970) 97.
- [118] L. Moneta *et al.*, *The RooStats project*, Proc. Sci. **ACAT** (2010) 057.
- [119] K. Melnikov and F. Petriello, *Electroweak gauge boson production at hadron colliders through  $O(\alpha_S^2)$* , Phys. Rev. **D 74** (2006) 114017.
- [120] E. Accomando *et al.*, *Z' physics with early LHC data*, Phys. Rev. **D 83** (2011) 075012.
- [121] R. Hamberg, W. L. van Neerven and T. Matsuura, *A complete calculation of the order  $\alpha_S^2$  correction to the Drell-Yan K factor*, Nucl. Phys. **B 359** (1991) 343, Erratum: - ibid. **B 644** (2002) 403.

- [122] W. L. van Neerven and E. B. Zijlsta, *The  $O(\alpha_S^2)$  corrected Drell-Yan K-factor in the DIS and  $\overline{MS}$  schemes*, Nucl. Phys. **B** **382** (1992) 11, Erratum: - *ibid.* **B** **680** (2004) 513.
- [123] P. Mathews, V. Ravindran and K. Sridhara, *NLO-QCD corrections to dilepton production in the Randall-Sandrum model*, JHEP **10** (2005) 031.
- [124] B. Clerbaux *et al.*, *Statistical analysis of the resonant signal search in the multiple final state modes*, CMS Analysis Note AN-10-312 (2011).
- [125] L. Randall and R. Sandrum, *An alternative to compactification*, Phys. Rev. Lett. **83** (1999) 4690.
- [126] L. Randall and R. Sandrum, *A large mass hierarchy from a small extra dimensions*, Phys. Rev. Lett. **83** (1999) 3370.
- [127] CMS Collaboration, *Search for Narrow Resonances in Dilepton Mass Spectra in pp Collisions at  $\sqrt{s} = 8$  TeV*, CMS Physics Analysis Summary EXO-12-061 (2013).
- [128] B. Clerbaux *et al.*, *Search for High Mass Resonances Decaying to Electron Pairs at 8 TeV with the Full 2012 dataset*, CMS Analysis Note AN-12-415 (2013).